January 2010

Ionic Mechanisms of Action Potential Rate Dependence, Conduction and Block in Normal Epicardium and in Remodeled Epicardium Post-Infarction

Keith Decker
Washington University in St. Louis

WASHINGTON UNIVERSITY IN ST. LOUIS

School of Engineering and Applied Science

Department of Biomedical Engineering

Dissertation Examination Committee:
Yoram Rudy, chair
Jianmin Cui
Igor R. Efimov
Sándor J. Kovács
Colin G. Nichols
Richard B. Schuessler

IONIC MECHANISMS OF ACTION POTENTIAL RATE DEPENDENCE, CONDUCTION AND BLOCK IN NORMAL EPICARDIUM AND IN REMODELED EPICARDIUM POST-INFARCTION

by
Keith Forest Decker

A dissertation presented to the
Graduate School of Arts and sciences
of Washington University in
partial fulfillment of the
requirements for the degree
of Doctor of Philosophy

August 2010

Saint Louis, Missouri

Abstract

In this work, detailed computational models are used to study the electrophysiology of normal epicardium and the arrhythmogenic effects of epicardial cell remodeling post-infarction. The canine epicardial myocyte model described here reproduces a wide range of experimentally observed rate dependent phenomena in cell and tissue. Model behavior depends on updated formulations for the 4-AP sensitive transient outward current (I_{to1}), the slow component of the delayed rectifier potassium current (I_{Ks}), the L-type Ca^{2+} channel ($I_{Ca,L}$) and the sodium-potassium pump (I_{NaK}) fit to data from canine ventricular myocytes. The model shows that I_{to1} plays a limited role in potentiating peak $I_{Ca,L}$ and Ca^{2+} release for propagated action potentials (APs), but modulates the time course of action potential duration (APD) restitution. I_{Ks} plays an important role in APD shortening at short diastolic intervals but a limited role in AP repolarization at longer cycle lengths. In addition, simulations demonstrate that $I_{Ca,L}$, I_{NaK} and $[Na^+]_i$ play critical roles in APD accommodation and the rate dependence of APD restitution. Starting from the ionic model of a normal epicardial cell described above, an epicardial border zone (EBZ) model was developed based on available remodeling data. Ionic models of normal zone (NZ) and EBZ myocytes were incorporated into one-dimensional models of propagation to gain mechanistic insight into how ion channel remodeling affects APD and refractoriness, vulnerability to conduction block and conduction safety post-infarction. Simulations of EBZ APD restitution show that remodeled I_{Na} and I_{CaL} promote increased effective refractory period (ERP) and prolonged APD at short diastolic interval (DI). Heterogeneous tissue simulations show that increased post-repolarization refractoriness and altered restitution lead to a large rate dependent vulnerable window for conduction block. In simulations of conduction post-infarction, EBZ I_{K1} remodeling partially offsets the reduction in conduction safety due to altered

I_{Na}, while I_{to1} and I_{CaL} have a negligible effect on conduction. Further simulations show that injection of skeletal muscle sodium channel SkM1-I_{Na}, a recently proposed anti-arrhythmic therapy, has several desirable effects including normalization of EBZ ERP and APD restitution, elimination of vulnerability to conduction block and normalization of conduction in uncoupled tissue.

Acknowledgements

I thank Dr. Yoram Rudy, for always demanding the best from his students and demanding even more from himself. I thank the Rudy lab members who I first met at Case Western Reserve University and who I have worked with, lived with and dined and drank at Mi Pueblo with early during my graduate career; Dr. Tom Hund, Dr. Greg Faber and Dr. Jon Silva and Tom O'Hara. I thank Jordi Heijman for making important contributions to the modeling studies presented here. I would also like to thank all of the other current and former members of the Rudy lab.

Most importantly, I would like to thank the people who made the decision to leave Ohio difficult; especially my grandparents, my brothers and my Mom and Dad, and the people who made this turn out to be the right decision; Austin, Serenity and Emily.

Table of Contents

List of Figures

Abbreviations

Commonly used abbreviations are below. Additional abbreviations accompany equations in Appendix A.

NZ	Normal Zone
EBZ	Epicardial Border Zone
VW	vulnerable window for formation of the initial line of block
AP	action potential, (ms)
APD	action potential duration, (ms)
PRR	post-repolarization refractoriness, (ms)
ERP	effective refractory period, (ms)
DI	diastolic interval, (ms)
SF	safety factor
LAD	left-anterior descending coronary artery
CL_{S1}	S1 pacing cycle length, (ms)
CI_{S2}	S2 coupling interval, (ms)
SR	sarcoplasmic reticulum
SS	subspace
g_j	gap junction conductance, μS
dV/dt_{max}	maximum AP upstroke velocity, (V/s)
$\tau_{recovery}$	time constant of recovery of AP upstroke velocity (ms)
τ_{VDI}	time constant of I_{CaL} voltage dependent inactivation (ms)
V_m	membrane potential (mV)
V_{rest}	resting membrane potential (mV)
V_{hold}	holding potential (mV)
CT_{KC}	K^+-Cl^- cotransporter
CT_{NaCl}	Na^+-Cl^- cotransporter
I_{NaL}	late Na^+ current
I_{Na}	fast Na^+ current
SkM1-I_{Na}	Skeletal muscle Na^+ current isoform 1
I_{Nab}	background Na^+ current
$I_{NaCa,i}$	Na^+/Ca^{2+} exchanger (localized to myoplasm)
I_{Cab}	background Ca^{2+} current
I_{pca}	sarcolemmal Ca^{2+} pump
I_{to1}	4-aminopyridine-sensitive transient outward K^+ current
I_{Kr}	fast delayed rectifier K^+ current
I_{Ks}	slow delayed rectifier K^+ current
I_{K1}	time-independent K^+ current
I_{NaK}	Na^+-K^+ pump current
I_{leak}	NSR leak
I_{diff}	Ca^{2+} diffusion, SR subspace to myoplasm
I_{tr}	Ca^{2+} transfer, NSR to JSR
I_{rel}	Ca^{2+} release from JSR
$I_{diff,ss}$	ion diffusion, subspace to local I_{CaL} subspace
$I_{NaCa,ss}$	Na^+/Ca^{2+}exchanger (localized to SR subspace)
$I_{Ca,L}$	L-type Ca^{2+} current

I_{to2}	Ca^{2+}-dependent transient outward Cl^{-} current
SS(CaL)	I_{CaL} subspace
SS(SR)	SR subspace
PLB	phospholamban
SERCA	SR Ca^{2+}-ATPase;
CSQN	calsequestrin
CaMKII	Ca^{2+}/calmodulin-dependent kinase
NSR	network SR
JSR	junctional SR.

Epigraph

"When first I engaged in this work, I resolved to leave neither words nor things unexamined...I soon found that...whatever abilities I had brought to my task, with those I must finally perform it. To deliberate whenever I doubted, to enquire whenever I was ignorant, would have protracted the undertaking without end, and perhaps without much improvement... I saw that one enquiry only gave occasion to another, that book referred to book, that to search was not always to find, and to find was not always to be informed; and that thus to pursue perfection was, like the first inhabitants of Arcadia, to chase the Sun, which, when they had reached the hill where he seemed to rest, was still beheld at the same distance from them. I then contracted my design, determining to confide in myself...by this I obtained at least one advantage, that I set limits to my work, which would in time be ended, though not completed."

- Preface to A Dictionary of the English Language, Samuel Johnson

Chapter 1. Background

1.1 The Epicardial Border Zone and Arrhythmogenesis Post-Infarction

Survivors of myocardial infarction are at an increased risk of ventricular arrhythmia and sudden death in the days and weeks following the initial ischemic event. Years of experiments have been devoted to increasing our understanding of the pathophysiological basis of this enhanced risk (Janse and Wit, 1989; Wit and Janse, 1992). The initiation of reentrant ventricular tachycardia is thought to depend on the presence of a substrate that has undergone structural and electrophysiological remodeling in reponse to the initial myocardial insult (Pinto and Boyden, 1999). This remodeling is thought to increase vulnerability to initiation of an arrhythmia in response to a triggering event. While ventricular tachycardia and its degeneration into ventricular fibrillation following myocardial infarction are leading causes of sudden cardiac death, the connection between structural and electrophysiological remodeling and increased vulnerability to arrhythmia remains poorly understood.

A canine model in which a transmural infarct is created by left anterior descending (LAD) coronary artery ligation is thought to provide an excellent model of arrhythmogenesis in humans, and as such has been the focus of years of experiments (Janse and Wit, 1989). Three to five days post-infarction, programmed stimulation protocols can be used to initiate tachycardias similar to those that are observed clinically (Wit and Janse, 1992). These programmed stimulation protocols are thought to mimic the spontaneous premature depolarizations that trigger arrhythmias in vivo. Arrhythmias in this model are reentrant in nature and have been mapped to a thin rim of surviving epicardial tissue that borders the infarct (the epicardial border zone or EBZ) (El-Sherif et al., 1977c)

The nature of reentry in the EBZ was first described in a series of experiments by El-Sherif and coworkers (El-Sherif et al., 1977a; El-Sherif et al., 1977c; El-Sherif et al., 1981;

Gough et al., 1985; Mehra et al., 1983; Restivo et al., 1990). This work showed that reentry can be initiated when a properly timed premature beat results in a line of conduction block. Wavefronts propagate around and then coalesce distal to this initial line of block. Reentry results when the coalesced wavefront breaks through and excites recovered tissue. This pattern of initiation often results in the figure-of-eight reentry characteristic of the EBZ preparation, although other patterns are observed. The initial line of block tends to form perpendicular to the myocardial fiber direction, while the long axis of the circuit during sustained reentry tends to align parallel to the fiber axis (Cardinal et al., 1988; Ciaccio et al., 2001a; Dillon et al., 1988). Reentry in this preparation is usually functional, in that gross anatomical obstacles are not often present within the reentrant circuit. When inducible, episodes of monomorphic tachycardia are often very stable, persisting for more than 100 cycles (Ciaccio et al., 2001b).

In whole heart and isolated tissue preparations, investigators have used epicardial mapping of paced beats and reentrant circuits to gain insight into the mechanisms underlying the initiation and maintenance of reentry. El-Sherif and coworkers have identified a gradient of increasing effective refractory period (ERP) from the periphery to the interior of the EBZ, and have argued that the formation of the initial line of block depends on propagation of a premature beat into EBZ tissue with abnormally long ERP (Gough et al., 1985; Restivo et al., 1990). Wit and coworkers have emphasized the importance of anisotropic tissue structure in the vulnerability to sustained reentry (Dillon et al., 1988). Early experiments (Dillon et al., 1988) and more recent high resolution mapping studies (Cabo et al., 2006) have reported regions of localized conduction slowing, especially for conduction transverse to the fiber axis and within the outer regions of the reentrant circuit. Tissue anisotropy may result in lowered safety factor for longitudinal conduction (Spach and Dolber, 1986; Spach et al., 1982; Spach et al., 1981),

contributing to the formation of initial lines of block, while preferential side-to-side uncoupling may contribute to formation of lines of apparent block during sustained reentry. A recent series of experiments by Ciaccio and coworkers (Ciaccio, 2000, 2001, 2002; Ciaccio et al., 2001a; Ciaccio et al., 2001b) has provided additional valuable information on the spatial and temporal properties of reentrant circuits in the EBZ. Reentrant circuits are characterized by a slow conduction zone (SCZ) in the region where the reentrant wavefront exits the central common pathway. The inducibility and cycle length (CL) of reentry are correlated with the length of the initial line of block and the geometry of the central common pathway. This work suggests that the spatial properties of the infarct are critical determinants of vulnerability to arrhythmia.

Studies in myocytes isolated from the EBZ have characterized the electrophysiological and structural remodeling processes that occur after infarction (Pinto and Boyden, 1999). Cells isolated from the EBZ have lowered upstroke velocity, slowed recovery of excitability and exhibit increased post-repolarization refractoriness (Lue and Boyden, 1992). These abnormalities are caused by altered Na^+ channel (I_{Na}) kinetics (Pu and Boyden, 1997), and the severity of I_{Na} remodeling is increased near the center of the reentrant circuit (Baba et al., 2005). EBZ cells lack a phase 1 notch due to a reduction in expression of both components of the transient outward current I_{to1} (Lue and Boyden, 1992) and I_{to2} (Aggarwal et al., 1997)). EBZ cells have a triangularized AP morphology linked to a reduction in I_{K1} density (Lue and Boyden, 1992). In addition to the aforementioned remodeling processes, altered density and kinetics of the L-type Ca^{2+} current ($I_{Ca(L)}$) (Aggarwal and Boyden, 1995) and delayed rectifier potassium currents (I_{Kr} and I_{Ks}) (Jiang et al., 2000) may play critical roles in altered rate dependence of action potential duration and morphology in the EBZ. Cells from the EBZ also show alterations in Ca^{2+} handling, including increased diastolic $[Ca^{2+}]_i$, decreased systolic $[Ca^{2+}]_i$, decreased rate

dependence of Ca^{2+}-transient (CaT) relaxation and a decrease in CaT amplitude with increased pacing frequency (Licata et al., 1997; Pu et al., 2000). These alterations in Ca^{2+} handling may be caused by a combination of ion channel remodeling (especially $I_{Ca(L)}$) and alterations in Ca^{2+} handling proteins, in particular calcium/calmodulin-dependent protein kinase II (CaMKII) (Hund and Rudy, 2004, 2006). Recent studies have shown increased levels of auto-phosphorylated (Hund et al., 2008a) and oxidized CaMKII (Christensen et al., 2009) in the EBZ. Increased CaMKII activation may contribute to altered I_{Na} and I_{NaL} activity in the EBZ (Christensen et al., 2009). Additional studies have characterized structural remodeling processes in the EBZ. In cells isolated from the outer pathway of the reentrant circuit, gap junction distribution is altered, with increased disarray and side-to-side localization (Cabo et al., 2006; Peters et al., 1997; Yao et al., 2003). This altered distribution is accompanied by a reduction in side-to-side coupling in isolated cell pairs (Cabo et al., 2006; Yao et al., 2003). The fact that the reentrant circuit is localized to regions of gap junction disarray that span the entire thickness of the EBZ (Peters et al., 1997) suggests an important role for structural remodeling in arrhythmogenesis.

Several computational studies of EBZ cell and tissue have provided important insights into mechanisms of arrhythmogenesis after infarction. In single cell and strand simulations, Cabo and Boyden studied the ionic determinants of EBZ ERP and repolarization (Cabo and Boyden, 2003). This study confirmed that I_{Na} remodeling plays a key role in post-repolarization refractoriness, and suggested that I_{CaL} remodeling plays a key role in APD heterogeneity between NZ and EBZ. A major limitation of this study was the failure to validate the ion channel properties and rate dependence of APD in the control model against available experimental data. Using this single cell model, Cabo and Boyden have developed two-dimensional models of the

EBZ and studied the stability of reentry after initiation. One study found that heterogeneity in gap junction coupling within the EBZ stabilizes reentry (Cabo and Boyden, 2006). A second study showed that heterogeneity in I_{Na} and I_{CaL} remodeling within the reentrant circuit also stabilizes reentry (Baba et al., 2005). These studies provide important hypotheses about how remodeling heterogeneity within the EBZ effects the stability of reentry, which should be tested using models of the NZ and EBZ where ion channel formulations and APD rate dependence have been more thoroughly validated. Additional studies by Hund and coworkers have emphasized the role of CaMKII remodeling in the EBZ post-infarction. CaMKII remodeling may alter Ca^{2+} homeostasis and contribute to altered I_{Na} and I_{NaL} function in the EBZ (Hund et al., 2008a). A recent study has linked CaMKII to reduced conduction velocity, increase effective refractory period and increased vulnerability to conduction block in the EBZ (Christensen et al., 2009). Importantly, neither the studies of Cabo et al. or Hund and coworkers have characterize the full range of rate dependent APD dynamics in NZ or EBZ models. In particular, the effect of EBZ remodeling on APD restitution was not explored. Considering the wide range of experimental and computational studies suggesting that the complex dependence of APD on rate is a critical determinant of the dynamics of reentry, this is an important limitation of previous computational studies of arrhythmia and remodeling in the EBZ.

1.2 Computational Models and the Study of Cardiac Arrhythmias

The intiation and maintenance of arrhythmia depends on the heterogeneous response of normal and remodeled cells to complex patterns of excitation. Studies of cardiac electrophysiology and arrhythmogenesis using detailed computational models often focus on results for standing action potentials or for steady state pacing, however. Experimentally, arrhythmia is often initiated by a single premature beat after sustained pacing at a slower cycle

length. Rate dependent heterogeneity of action potential duration and refractoriness will be a key determinant of whether that premature beat will lead to conduction block. The spatial distribution of APD after the initial line of block forms will help determine whether reenty is initiated. The spatial and temporal response of APD to changes in rate will govern the transition from the initiating premature beat to the fast cycle lengths of reentry and the chaotic activation patterns of fibrillation. Thus, while important insights can be gained by the study of APD at one or a few pacing rates, understanding of arrhythmogenesis will depend on the study of a wider range of pacing protocols. The study of arrhythmia in physiologicall detailed models has been limited by their computational complexity and the failure of available models to reproduce the range of rate dependent phenomena observed experimentally (Cherry and Fenton, 2006). This has led to the development of simplified computational models that reproduce a desired set of rate dependent phenomena observed experimentally, but do not ground APD dynamics in physiological representations of underlying ionic currents and ion concentrations. This approach has led to important contributions to our understanding of the link between APD rate dependence and arryhthmia, but questions arise as to whether models that do not contain accurate representations of underlying physiological processes will lead to clinically relevant finding. Clearly, there is a critical need for computational models that both accurately represent underlying physiological processes and reproduce a wide range of rate dependent phenomena relevant to arrhythmogenesis.

1.3 Electrophysiological and Structural Determinants of Arrhythmia

The rate dependence of APD has been extensively characterized in experiment and linked to the initiation and maintenance of arrhythmogenesis through a large body of computational research. APD depends on both the time since repolarization of the previous action potential

(diastolic interval or DI) and the history of stimulation prior to the previous action potential (memory). APD adaptation (also referred to as dynamic restitution) is defined as the dependence of APD on steady state pacing cycle length (CL_{S1}). APD restitution is defined as the dependence of APD on the diastolic interval (DI) or coupling interval (CI) of an additional (S2) stimulus after pacing to steady state at CL_{S1}. After pacing to steady state at CL_{S1}, APD accommodation (Watanabe and Koller, 2002) (also referred to as short term memory (Franz et al., 1988)) is defined as the time course of adjustment of APD during sustained pacing at a new CL (CL_{S2}). APD adaptation, restitution and accommodation are aspects of action potential rate dependence ubiquitously observed in the ventricular myocardium of many species including human, despite wide variation in action potential duration morphology and ion channel expression across species and cell types. Experimentally characterized restitution curves typically show increasing APD with increasing DI, with the steepest slope at the shortest DI. During accommodation after a change from a fast to a slow CL, APD adjusts monotonically to a new steady state over a time course of minutes. As with APD restitution, APD adaptation typically shows an increasing APD as a function of increasing DI or CL. However, APD adaptation shows a shallower slope than APD restitution at the intersection of the two curves. A large body of computational studies have emphasized the importance of APD rate dependence in the initation and maintenance of arrhythmias. The steepness of APD restitution is thought to promote APD alternans and govern the transition from stable to chaotic arrhythmias, the so-called 'Restitution Hypothesis' (Karma, 1994). APD accommodation and memory are thought to play a role in the stability of fibrillation (Baher et al., 2006; Toal et al., 2009). Heterogeneity in APD adaptation is a key determinant of the dispersion of repolarization and susceptibility to the initiation of arrhythmias. Despite the ubiquitously observed properties of APD adaptation, restitution and accommodation and their

likely role in arrhythmia, many currently available models fail to reproduce some or all of these phenomena (Cherry and Fenton, 2006). In addition, the underyling mechanisms of these phenomena remain incompletely understood.

Additional electrophysiological and structural properties of tissue beyond the rate dependence of APD will determine susceptibility to arrhythmia. Conduction safety and vulnerability to conduction block will depend on the complex interplay of electrophysiological and structural remodeling processes. Currents contributing to depolarization and phase 1 action potential (AP) amplitude, including I_{Na}, I_{CaL}, I_{to1} and I_{to2} are remodeled in the EBZ and may play a role in abnormal conduction (Huelsing et al., 2001; Joyner et al., 1996; Rohr and Kucera, 1997; Shaw and Rudy, 1997). Structural factors including gap junction coupling (Shaw and Rudy, 1997), tissue anisotropy (Spach and Dolber, 1986; Spach et al., 1982; Spach et al., 1981) and wave-front curvature (Cabo et al., 1994; Fast and Kleber, 1995, 1997) are also critical determinants of conduction safety. Other electrophysiological and structural determinants of the stability of reentry after induction include cell excitability (Beaumont et al., 1998), conduction velocity restitution (Cherry and Fenton, 2004; Fenton et al., 2002), AP morphology (Cherry and Fenton, 2004) and Ca^{2+}-dependent voltage alternans (Sato et al., 2006; Shiferaw et al., 2005).

1.3 Objectives

The development of rational approaches to the prevention and treatment of arrhythmia depends on our understanding of underlying ionic mechanisms. A large body of literature has characterized the electrophysiological and structural remodeling processes that may increase vulnerability to arrhythmia after infarction. Computational studies are critical for underlying how these remodeling processes lead to heterogeneity in the electrophysiological properties of normal and diseased cells, and how this heterogeneity creates a substrate vulnerable to the

initation and maintenance of arrhythmia. Given this critical need, the research presented here was undertaken: 1) To develop an ionic model of the normal canine epicardial myocyte that accurately reproduces a wide range of rate dependent phenomena, and to link these rate dependent phenomena to underyling ionic processes. 2) To develop an ionic model of the remodeled epicardial border zone myocyte, and link ion channel remodeling to abnormal APD rate dependence. 3) To study, in multicellular tissue models, how heterogeneity in normal and EBZ cell behavior leads to a substrate with increased vulnerability to arrhythmia due to abnormal APD rate dependence, altered conduction and increased susceptibility to conduction block.

Chapter 2. Action Potential Rate Dependence in a Computational Model of Canine Epicardium

2.1 Introduction

Cardiac arrhythmias and sudden death involve complex myocardial activation patterns including conduction block, reentry and fibrillation. In order to understand the relations and transitions between these patterns, the ionic determinants of the response of healthy and diseased cardiac myocytes to complex patterns of excitation must be understood. The single cell response to such excitation patterns depends on the complex interaction between ionic currents, intracellular ion concentrations and membrane voltage. Computational cell models provide critical tools for exploring these interactions, allowing the development and testing of hypotheses about underlying ionic mechanisms based on careful integration of available experimental data (Rudy and Silva, 2006). The canine is a common animal model for studying cell electrophysiology in a range of disease states. Our group and others have developed detailed mathematical models of the canine action potential (Fox et al., 2002; Hund and Rudy, 2004; Winslow et al., 1999). While these models have been used to study arrhythmia mechanisms after heart failure (Winslow et al., 1999) and myocardial infarction (Cabo and Boyden, 2003; Hund et al., 2008b) as well as ionic mechanisms of alternans (Fox et al., 2002; Livshitz and Rudy, 2007), they are limited in their ability to simulate important rate-dependent phenomena (Cherry and Fenton, 2007), including the dependence of steady-state action potential duration on pacing cycle length (CL) (APD adaptation), the dependence of APD on diastolic interval (DI) (APD restitution) and the time course of the adjustment of APD to changes in rate (short-term memory (Franz et al., 1988) or APD accommodation (Watanabe and Koller, 2002)). These limitations extend to ionic models of other species, including the human (Cherry and Fenton,

2007). We hypothesized that canine epicardial APD adaptation, restitution and accommodation could be simulated and understood based on available descriptions of subcellular ionic processes. We incorporated updated and validated formulations of the 4-AP sensitive transient outward current (I_{to1}), the slow component of the delayed rectifier potassium current (I_{Ks}), the L-type Ca^{2+} channel ($I_{Ca,L}$) and the sodium-potassium pump (I_{NaK}) into a previously published model of the canine epicardial myocyte (Hund et al., 2008b; Hund and Rudy, 2004; Livshitz and Rudy, 2007). Model behavior was examined in both single cell and multicellular (strand) simulations. Our work provides new insight into molecular mechanisms underlying important rate-dependent action potential properties, including APD restitution, adaptation and accommodation. Specifically, our studies highlight the importance of I_{to1} and I_{Ks} in APD restitution, and the role of $I_{Ca,L}$ and I_{NaK} in APD accommodation and rate dependent APD restitution.

2.2 Methods

Cell Simulations

Steady-state results are shown after pacing for 1800 seconds at a given CL with a conservative K^+ stimulus (Hund et al., 2001). This simulation time resulted in a beat-to-beat change in APD, maximum intracellular sodium ($[Na^+]_{i,max}$) and calcium ($[Ca^{2+}]_{i,max}$) of less than 0.1%. Restitution results were obtained for an additional beat after pacing to steady-state as described. Accommodation simulations involved pacing to steady-state at a given CL (CL_{S1}), followed by pacing to steady-state at a different CL (CL_{S2}).

Strand Simulations

One-dimensional simulations of propagation were performed in a strand of 96 cells, following previous work from our laboratory (Shaw and Rudy, 1997). Cell 1 was directly stimulated, and simulation results are shown for a central cell (cell 48). Stimulation protocols

were similar to those used for single cells (duration of pacing = 1800 s), resulting in beat-to-beat changes in APD, $[Na^+]_{i,max}$ and $[Ca^{2+}]_{i,max}$ of less than 0.1%. Gap junction conductance of 2.5 μS gave a maximum upstroke velocity (Di Diego et al., 1996) and conduction velocity (Spach et al., 2000) consistent with experimental results in canine epicardial tissue. Additional parameters used in multicellular simulations are included in Appendix A.

2.3 Model Development

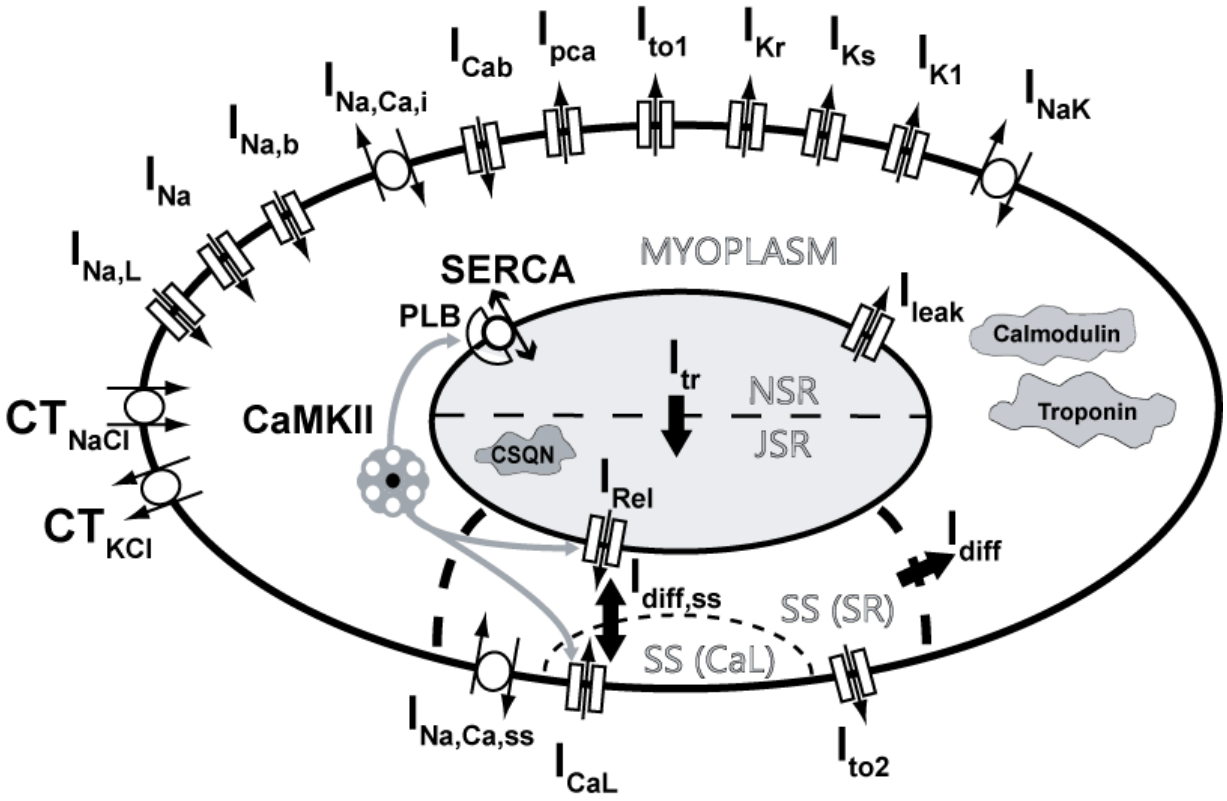

Figure 2-1 Canine Epicardial Cell Model . See page vii and Appendix A for abbreviations and equations.

The Hund-Rudy dynamic (HRd) model (Fig. 2-1) (Hund et al., 2008b; Hund and Rudy, 2004; Livshitz and Rudy, 2007) served as a starting point for development of an updated model of the canine epicardial myocyte. Major reformulations were made to the L-type Ca^{2+} current ($I_{Ca,L}$), the potassium component of the transient outward current (I_{to1}), the delayed rectifier potassium current (I_{Ks}), the Na^+-K^+ pump (I_{NaK}), the chloride component of the transient outward current

(I_{to2}) and the late sodium current (I_{NaL}). Parameters for reformulated currents were fit to experimental data from canine epicardial myocytes whenever possible. Experimental data was chosen that represented either the consensus of a wide range of experimental results or came from the most complete available studies. Special attention was given to the role of each of these reformulated currents in the rate dependence of action potential duration in canine epicardial model and experiment. Updates made to intracellular calcium ($[Ca^{2+}]_i$) handling in a recent study of APD and $[Ca^{2+}]_i$- transient (CaT) alternans were also included (Livshitz and Rudy, 2007). Appendix A includes a complete set of model equations and descriptions of adjustments to model parameters not included in this section

2.3.1 I_{CaL}

Figure 2.2*A* shows the state structure of a novel Markov model of $I_{Ca,L}$. This model was formulated with the goals of 1) reproducing a wide range of experimental data 2) maintaining computational tractability in order to facilitate long-term multicellular simulations. Activation is voltage dependent (α and β transitions). In Ca^{2+} free conditions, inactivation and recovery from inactivation are voltage dependent (x and y transitions). Elevation of Ca^{2+} in a local subspace ($[Ca^{2+}]_{SS,CaL}$) moves channels from the Ca^{2+}-free gating tier to an upper tier (θ and δ transitions) characterized by accelerated inactivation (x^* and y^* transitions). This structure reflects the hypothesis that Ca^{2+} binding to calmodulin removes a "brake" and speeds up I_{CaL} voltage dependent inactivation (Mahajan et al., 2008; Pitt, 2007). $[Ca^{2+}]_{SS,CaL}$ elevation depends on I_{CaL} Ca^{2+} entry and diffusion of Ca^{2+} ($I_{diff,SS}$) after SR Ca^{2+}-induced Ca^{2+} release. This phenomenological approach allows reproduction of slowed I_{CaL} Ca^{2+} dependent inactivation when SR function is blocked or intracellular Ca^{2+} buffering is high.

The I_{CaL} Markov model was fit to data from canine ventricular myocytes wherever possible. The $I_{Ca,L}$ current-voltage (I-V) relationship was fit to data from left ventricular

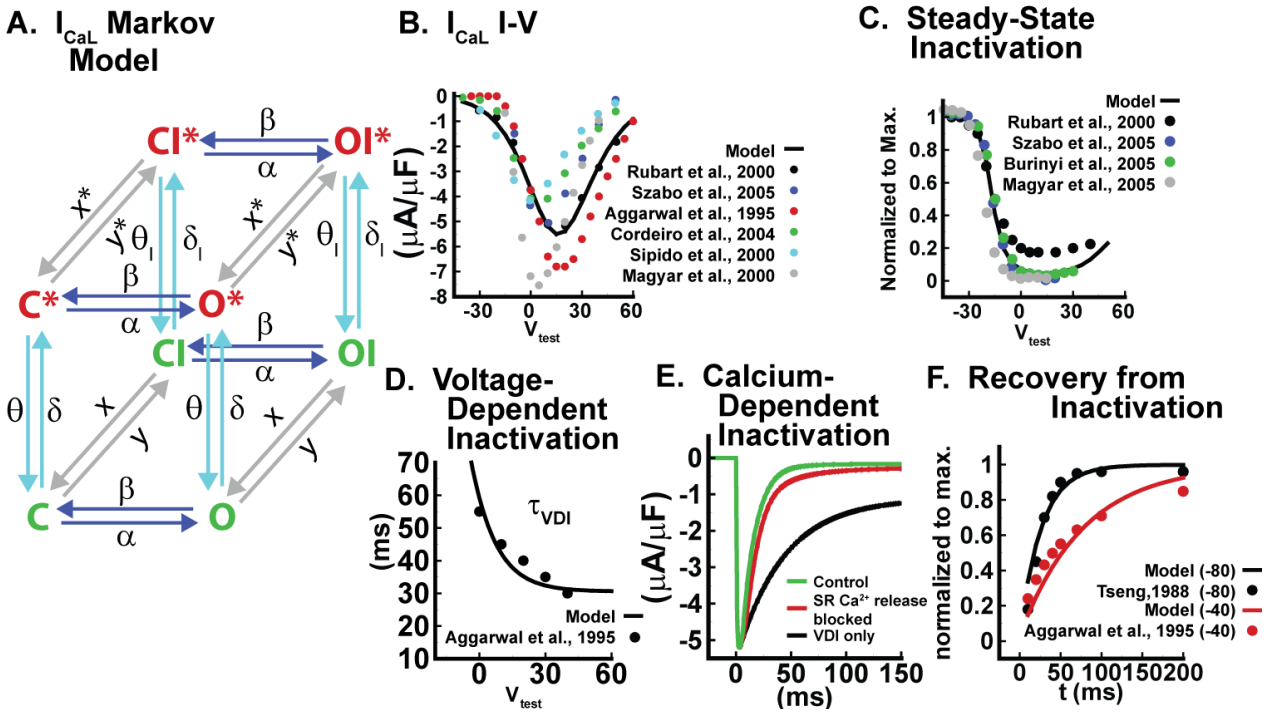

Figure 2-2 I_{CaL} Model and Experimental Fits. (A) I_{CaL} Markov Model diagram, (B) $I_{Ca,L}$ current-voltage (I-V) relationship and (C) steady-state inactivation, (D) voltage-dependent inactivation, (E) calcium-dependent inactivation and (F) recovery from inactivation .

myocytes, (Rubart et al., 2000) (Fig. 2-2*B*). The Rubart I-V curve data (Rubart et al., 2000) was chosen because it falls in the middle range of canine ventricular data recorded at body temperature (Aggarwal and Boyden, 1995; Cordeiro et al., 2004; Magyar et al., 2002; Rubart et al., 2000; Sipido et al., 2000; Szabo et al., 2005). Model I_{CaL} steady state inactivation is compared to multiple experimental data sets in Figure 2-2*C*. The Szabo steady state inactivation data (Szabo et al., 2005) chosen for model fitting has a slope and $V_{1/2}$ consistent with multiple experiments from canine ventricle at body temperature (Birinyi et al., 2005; Magyar et al., 2002; Rubart et al., 2000; Szabo et al., 2005). I_{CaL} steady state inactivation data with lesser degrees of

inactivation at steady state (Rubart et al., 2000) resulted in model APD outside the range observed in canine experiments. Experimental studies have shown that I_{CaL} inactivation is Ca^{2+} dependent, and is significantly slowed in Ca^{2+}-free solutions. The time constant of voltage dependent inactivation (τ_{VDI}) in Ca^{2+}-free solutions is fit to data from canine epicardial myocytes (Aggarwal and Boyden, 1995) (Fig. 2-2*D*). Voltage dependent inactivation was simulated in the model by eliminating Ca^{2+} dependent transitions to upper tier states. Figure 2-2*E* compares the relative contribution of voltage, Ca^{2+} entry via I_{CaL} and SR Ca^{2+} release to inactivation in the model. I_{CaL} inactivation is fastest in control, is modestly slowed by block of SR Ca^{2+} release and is substantially slowed by complete elimination of Ca^{2+} dependent inactivation (VDI only). The quantitative dependence of I_{CaL} inactivation on I_{CaL} Ca^{2+} entry, SR Ca^{2+}-release and voltage is difficult to characterize experimentally, but model behavior is qualitatively consistent with available experimental evidence (Findlay, 2002a, b; Sun et al., 1997). Model voltage dependence of the time constant of recovery from inactivation (Fig. 2-2*F*) is consistent with canine ventricular data (Aggarwal and Boyden, 1995; Tseng, 1988).

2.3.2 I_{Ks}

The Hodgkin-Huxley based formulation for I_{Ks} used in the Hund-Rudy model of the canine epicardial myocyte (Hund and Rudy, 2004) was replaced with the 17 state Markov model proposed by Silva and Rudy (Silva and Rudy, 2005). The structure of the I_{Ks} model is shown in Figure 2-3*A*. The original Silva-Rudy model accurately reproduces the kinetics of I_{Ks} in guinea pig and human based on underlying voltage sensor transitions and has provided insight into the role of I_{Ks} in APD adaptation in these species (Silva and Rudy, 2005). The I_{Ks} model can be divided into deep closed states (Zone 2), closed states near the open state (Zone 1) and open states. Transition from rest (Zone 2) to the open state (Open) requires a slow Zone 2 to Zone 1

transition (the first voltage sensor transition), followed by a fast Zone 1 to Open state transition (the second voltage sensor transition) . Transition rate parameters were adjusted to fit the following data from canine epicardial and midmyocardial myocytes: i) tail current amplitudes at holding potentials from -20 to +70 mV after 300 ms and 3000 ms of activation (Fig. 2-3*B*) (Volders et al., 2003); ii) tail currents at holding potentials from -10 to 60 mV after 5000 ms of

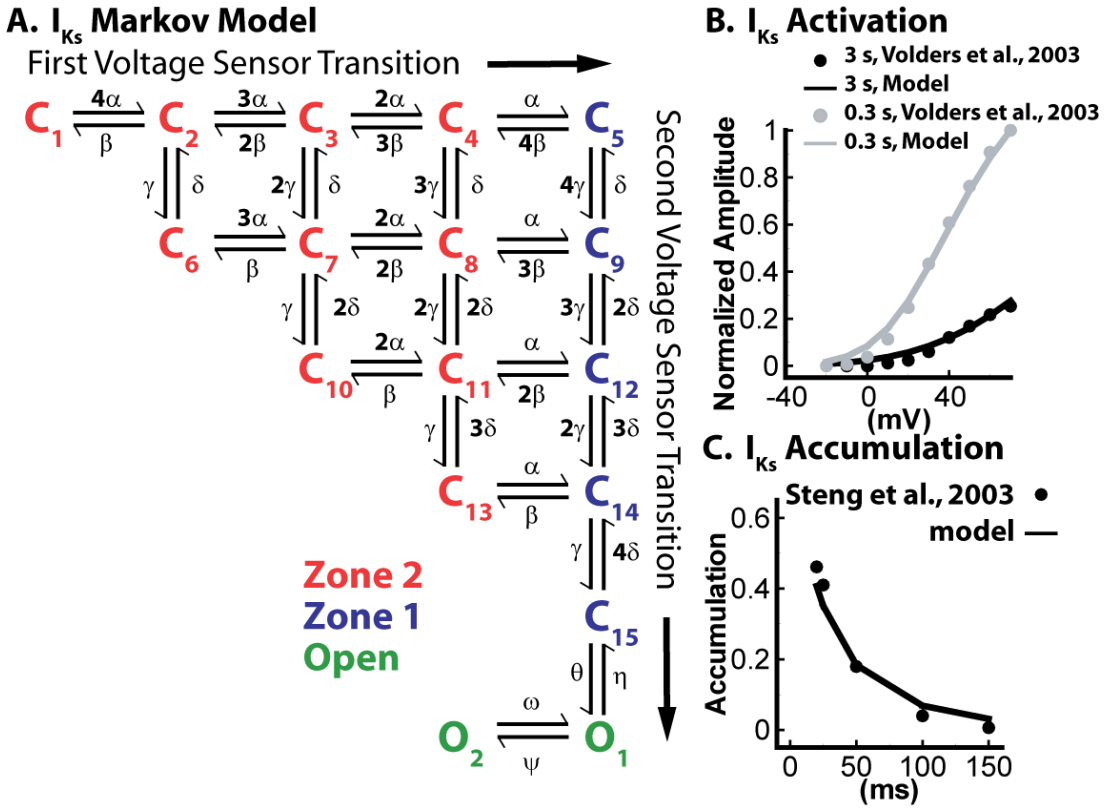

Figure 2-3 I_{Ks} Model and Experimental Fits. (A) I_{Ks} Markov Model state diagram and model fits to (B) activation and (C) accumulation.

activation (Liu and Antzelevitch, 1995; Stengl et al., 2003); iii) activation half-time on depolarization to +20 mV (Liu and Antzelevitch, 1995; Stengl et al., 2003); iv) deactivation half-times for tail currents to -25, -50 and -80 mV (Liu and Antzelevitch, 1995; Stengl et al., 2003) and v) accumulation characteristics for inter-pulse intervals between 20 and 150 ms after 200 ms

depolarizing steps (Fig. 2-3*C*) (Stengl et al., 2003). Current density was scaled to that of canine epicardial myocytes (Liu and Antzelevitch, 1995; Stengl et al., 2003).

2.3.3 I_{to1}

Model I_{to1} is derived from a previous formulation (Dong et al., 2006). Modifications were made to better fit experimental measurements from the canine. Model I_{to1} density is consistent with multiple experiments from canine left ventricular epicardial cells (Fig. 2-4A) (Liu et al., 1993; Lue and Boyden, 1992; Sun and Wang, 2005). Activation and inactivation

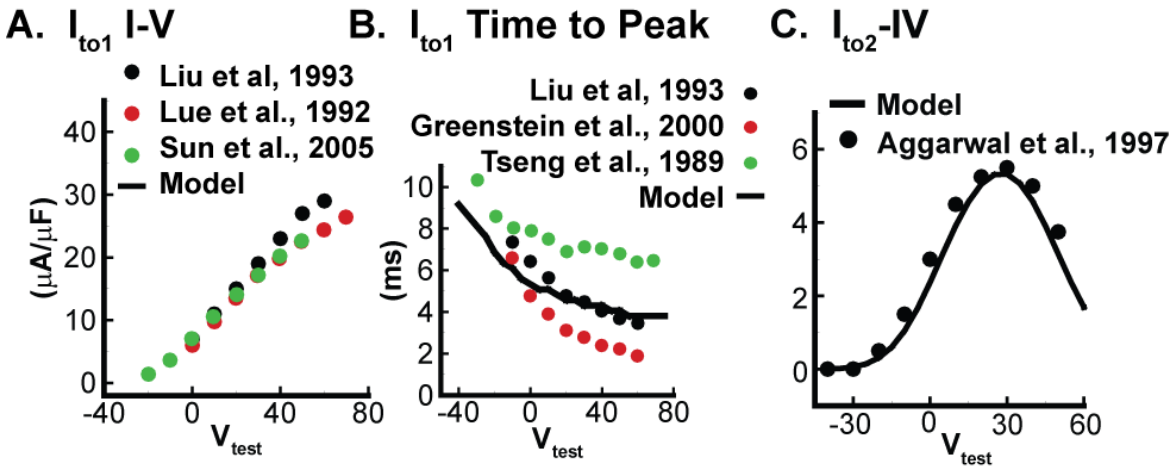

Figure 2-4 I_{to1} and I_{to2} Experimental Fits. Model fits to (A) I_{to1} I-V Curve, (B) I_{to1} time-to-peak and (C) I_{to1} I-V curve.

kinetics were adjusted to reproduce experimentally measured time to peak (Greenstein et al., 2000; Lue and Boyden, 1992; Tseng and Hoffman, 1989). Model time to peak falls in the middle range of published data from canine epicardial cells (Fig. 2-4*B*) and is a significant improvement on other published Hodgkin-Huxley formulations (Dumaine et al., 1999; Sun and Wang, 2005), in which time to peak is much faster (<1 ms) than that observed experimentally. The time constant of inactivation of I_{to1} at positive voltages in canine epicardial myocytes is typically around 10 ms (Cordeiro et al., 2009; Lue and Boyden, 1992). Consistent with a

previous modeling study (Flaim et al., 2006), this time constant of inactivation resulted in a non-physiological notch and dome shape for the action potential (Simulations not shown). Following Flaim et al., I_{to1} inactivation was accelerated (τ = 5 ms) to achieve a realistic action potential shape. The required acceleration of I_{to1} inactivation in the model may reflect in vivo acceleration of I_{to1} inactivation by intracellular Ca^{2+} (Flaim et al., 2006; Patel et al., 2004). A slow inactivation gate was included to reproduce the slow recovery from inactivation observed in canine (Liu et al., 1993).

2.3.4 I_{to2}

Although I_{to2} remains a poorly characterized current, a novel formulation was developed to reflect the best available information in canine left ventricular myocytes (Aggarwal et al., 1997; Tseng and Hoffman, 1989; Zygmunt, 1994). Model I_{to2} is a Cl^- carrying current, activates and deactivates rapidly (Aggarwal et al., 1997; Zygmunt, 1994) and can be completely eliminated by block of SR Ca^{2+} release, consistent with experiment. I_{to2} current voltage relationship was fit to data from canine epicardial myocytes (Fig. 2-4C) (Aggarwal et al., 1997).

2.3.5 I_{NaK}

A recently developed I_{NaK} formulation based on data from canine left ventricular epicardial myocytes (Gao et al., 1995; Gao et al., 2005) was incorporated into the model. Model I_{NaK} density was fit to experimental data (Fig. 2-5*A*) (Gao et al., 2005) adjusted to 37^{o}C using Q10 = 2.1 (Sakai et al., 1996). I_{NaK} is a critical determinant of $[Na^+]_i$ homeostasis in the model. Fig. 2-5*B* demonstrates that the model accurately reproduces $[Na^+]_i$ at rest and after sustained pacing at CL = 500 ms. Model fit to the pacing dependence of $[Na^+]_i$ also depends on the density of 'background' Na^+ fluxes (I_{Nab} and CT_{NaCL}). While information on the magnitude and

dependence of these background fluxes on V_m, $[Na^+]_i$ and other factors remains limited, it is

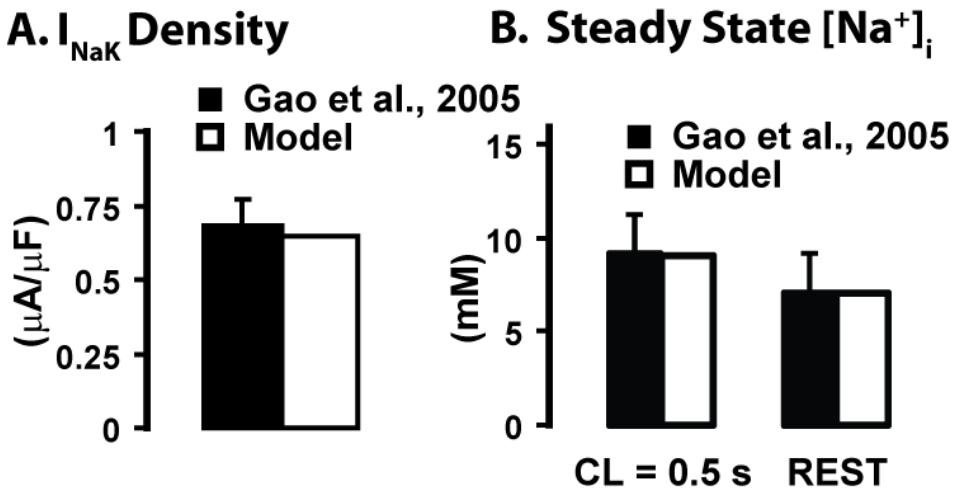

Figure 2-5 I_{NaK} and $[Na^+]_i$ Experimental Fits. Model fits to experimental (A) I_{NaK} density and (B) steady-state $[Na^+]_i$

clear that both electrogenic and non-electrogenic background Na^+ fluxes exist and are important determinants of Na^+ homeostasis in model and experiment (Despa et al., 2002; Gao et al., 2005; Shivkumar et al., 1997).

2.3.6 I_{NaL}

A novel I_{NaL} formulation was developed based on recent data from human and canine ventricular myocytes and reflects present understanding of the current (Zaza et al., 2008). At 24°C, human (Maltsev and Undrovinas, 2006) and canine (Maltsev et al., 2008a) ventricular I_{NaL} inactivates with fast ($\tau \sim 50$ ms) and slow ($\tau \sim 500$ ms) time constants during a pulse to -30 mV. These fast and slow time constants are thought to represent burst and late activating modes of the cardiac Na^+ channel isoform ($Na_v1.5$), respectively. Total I_{NaL} in the model is calculated as the sum of channels in the late bursting (*LB*) and late scattered (*LS*) modes. Time and voltage dependent inactivation of the burst and late activating modes was implemented using Hodgin-Huxley type gates h_{LB} and h_{LS}. Considering the similarities in reported behavior in human

(Maltsev and Undrovinas, 2006) and canine ventricle (Maltsev et al., 2008a), I_{NaL} onset of inactivation is based on characterization of the time course of inactivation in human ventricular myocytes (Maltsev and Undrovinas, 2006), as adjusted to 37^{o}C based on Q10 data (Maltsev and Undrovinas, 2006). The relative contribution of the late scattered mode ($f_{LS} = 0.27$) and steady state voltage dependence of inactivation is based on canine ventricular myocyte data (Maltsev et al., 2008a). The time constant of recovery from inactivation was adapted from data in human ventricular myocytes (Maltsev et al., 1998), also adjusted to 37^{o}C based on Q10 of 2.2 (Maltsev and Undrovinas, 2006). Current density was adjusted to reproduce the experimentally measured APD prolongation of approximately 40 ms after application of low concentrations of TTX in canine epicardial myocytes (Zygmunt et al., 2001). No experimental data are available on I_{NaL} in the EBZ.

2.4 Ionic Mechanisms of Action Potential Duration Adaptation, Restitution and Accommodation

2.4.1 APD Rate Dependence in Cell and Strand

Figure 2-6 compares the rate dependence of APD in model and experiment. The rate dependence of simulated steady-state APs is shown in Fig. 2-6*A (left).* Both cell and strand simulations exhibit the spike and dome morphology characteristic of canine epicardium (Fig. 2-6*A right).* (Liu et al., 1993). Steady-state APs in the strand show a reduced upstroke amplitude and velocity compared to the single cell due to electronic load during propagation. Maximum upstroke voltage (V_{max}) and velocity (dV/dt_{max}) match experiments in canine ventricular epicardium at CL = 0.8 s (Di Diego et al., 1996) (experiment V_{max} = 13.1±4.7 mV, dV/dt_{max} = 151.8±39.8 V/s; model V_{max} = 9.24 mV, dV/dt_{max} = 162.6 V/s) . In addition, phase 1 notch depth is less rate dependent in the strand than in the single cell, also consistent with experiments (Fig.

2-6*A*) (Liu et al., 1993). We next determined APD restitution in our single cell and strand models. After pacing to steady-state at a given CL (CL_{S1}), additional stimuli (S2) scanning the

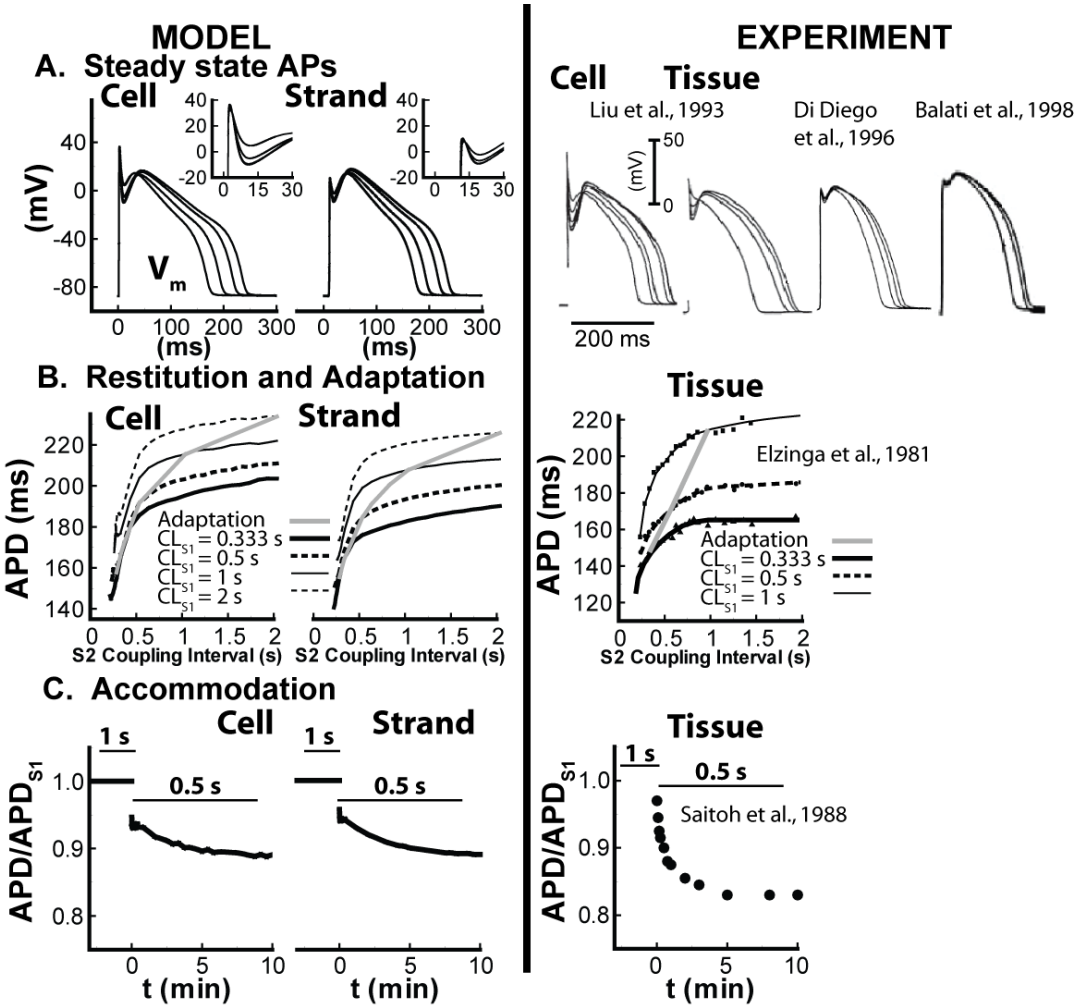

Figure 2-6 APD Rate Dependence in Cell and Strand. (A, left) Model steady-state APs at CL = 0.3, 0.5, 1 and 2 s in cell and strand. Peak upstroke voltage and rate dependence of notch depth are shown in the inset. (A, right) Experimental steady state APs in single cell and three tissue preparations are included for comparison. (B, left) Model CL_{S1} dependence of APD restitution in cell and strand. Gray traces denote adaptation (S2 coupling interval = CL_{S1}). (B, right) CL_{S1} dependence of APD restitution in experiment (right ventricle, open chest dogs) (Elzinga et al., 1981). (C, left) Model accommodation of APD after a change in CL from 1 s to 0.5 s in cell and strand. (C, right) APD accommodation in canine ventricular muscle fiber experiments (Saitoh et al., 1988).

diastolic interval were applied to generate restitution curves (Fig. 2-6*B*, *left*). As the basic pacing cycle length (CL_{S1}) decreases, restitution curves in the single cell and strand models shift towards shorter APD, consistent with experimental measurements (Fig. 2-6*B*, *right*) (Boyett and Jewell, 1978; Cherry and Fenton, 2007; Elzinga et al., 1981; Han and Moe, 1969). Fig 2-6*C* *(left)* shows the time course of APD in model cell and strand after pacing to steady-state at CL_{S1} = 1 s, followed by sustained pacing at CL_{S2} = 0.5 s starting at t = 0. APD at the new CL approaches steady-state after several minutes of pacing, consistent with experiments in canine ventricle (Fig. 2-6*C*, *right*) (Saitoh et al., 1988).

2.4.2 Differences in cell and strand behavior

Cardiac myocyte electrophysiology and AP dynamics are often studied and simulated in

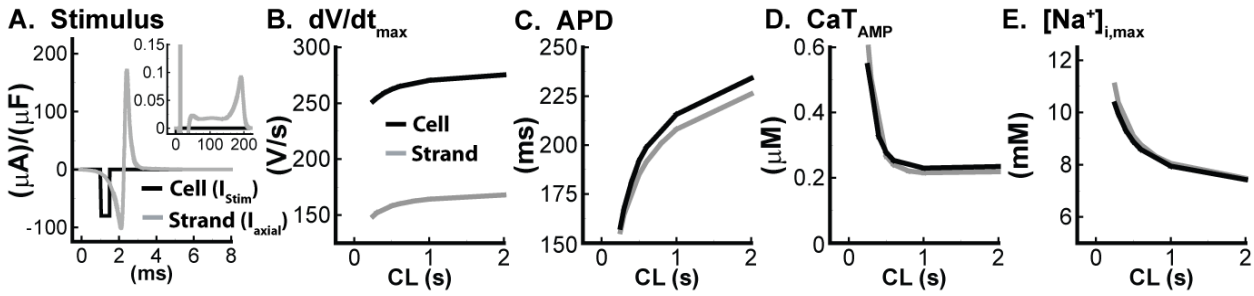

Figure 2-7 Differences in Rate Dependence in Cell and Strand. (A) Comparison of isolated cell stimulus (black) and strand axial current (gray). Inset shows sustained repolarizing axial current. CL_{S1} dependence of (B) dV/dt_{max} (C) APD (D) CaT_{AMP} and (E) $[Na^+]_{i,max}$ in cell and strand simulations.

isolated cells. We hypothesized that AP dynamics would differ between isolated cell and tissue due to differences in applied stimulus and electrotonic loading. A -80 μA/μF, 0.5 ms stimulus was used in single cell simulations (Fig. 2-7*A*). In the strand, excitatory axial current in well-coupled tissue (Fig. 2-7*A*) consists of i.) an initial transient depolarizing current ii.) a transient repolarizing current as the cell supplies charge to depolarizing downstream cells and iii.) a small sustained repolarizing current (Fig. 2-7*A*, inset). The biphasic axial current in the tissue reduces

AP upstroke velocity relative to its value in the single cell (Fig. 2-7*B*). In addition, steady-state tissue APD is reduced slightly (Fig. 2-7*C*) due to the sustained repolarizing axial current (Fig. 2-7*A*, inset). APD adaptation in cell and strand simulations (Fig. 2-7) is consistent with experiments (Liu et al., 1993). Both cell and strand simulations show an increase in Ca^{2+} transient amplitude (CaT_{AMP}) (Fig. 2-7*D*) (Sipido et al., 2000) and maximum intracellular Na^{+} ($[Na^{+}]_{i,max}$) (Fig. 2-7*E*) (Gao et al., 2005) with pacing rate, consistent with experiment. Differences in CaT_{AMP} and $[Na^{+}]_{i,max}$ in cell and strand simulations are minimal. Subsequent results are from strand simulations unless otherwise specified.

Experimental (Saitoh et al., 1988) and computational (Greenstein et al., 2000) studies have suggested that I_{to1}, by controlling phase 1 repolarization, is an important modulator of $I_{Ca,L}$ activation and intracellular $[Ca^{2+}]_i$ release. We hypothesized that the effect of I_{to1} on $I_{Ca,L}$

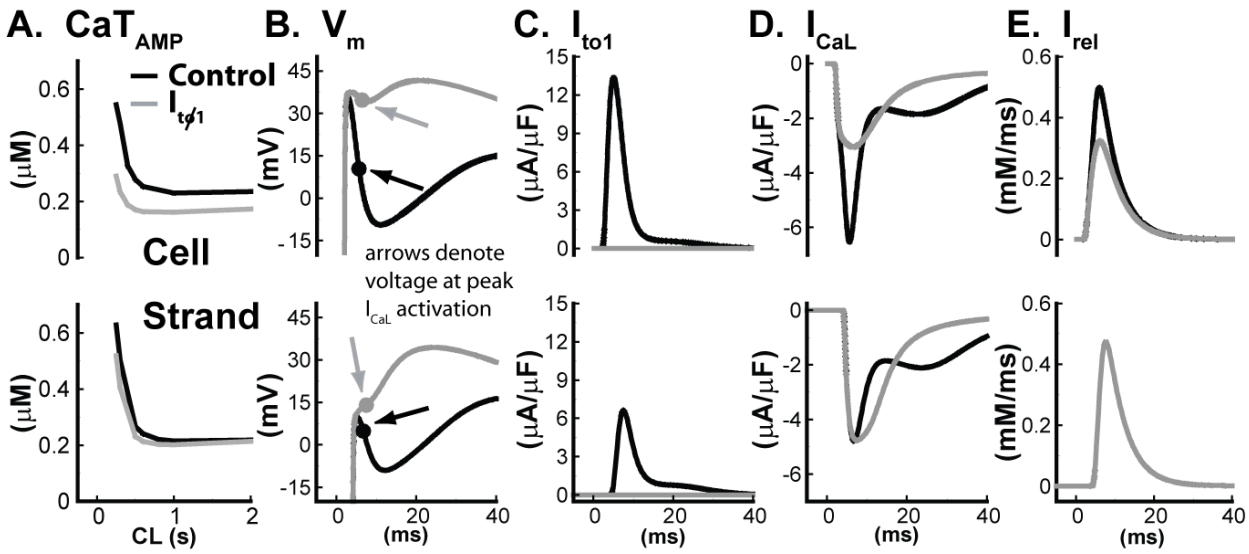

Figure 2-8 I_{to1} Block in Cell and Strand. (A) CaT_{AMP} (B) V_m (C) I_{to1} (D) $I_{Ca,L}$ and (E) I_{rel}, in control and after 100% I_{to1} block in cell (top) and strand (bottom) simulations. B-E are for CL_{S1} = 1 s. Arrows in (B) denote time and V_m at peak $I_{Ca.L}$.

activation and $[Ca^{2+}]_i$ release would differ between isolated cells and multi-cellular tissue due to differences in upstroke velocity and AP amplitude. Fig. 2-8*A* shows that, while block of I_{to1}

leads to a significant reduction in CaT_{AMP} in cell simulations, reduction in CaT_{AMP} after I_{to1} block in tissue simulations is minimal. The interplay between V_m, I_{to1}, $I_{Ca,L}$ and Ca^{2+} release from the sarcoplasmic reticulum (SR) in cell and strand is examined in panels B-E. We note several important differences between simulated APs in the strand and in the isolated cell. These unique features of the strand AP include 1) reduced peak upstroke voltage (Fig. 2-8*B*); 2) reduced I_{to1} activation (Fig. 2-8*C*); and 3) minimal dependence of peak $I_{Ca,L}$ on I_{to1} activation (Fig. 2-8*D*). Reduced peak upstroke voltage in the strand leads to a reduction in peak I_{to1} due to the approximately linear dependence of I_{to1} activation on V_m. This reduction in I_{to1} activation leads to a reduction in phase 0 repolarization. Arrows in Fig. 2-8*B* denote V_m at the peak of $I_{Ca,L}$ activation in cell and strand, respectively. In cell simulations, a large I_{to1} repolarizes V_m (Fig. 2-8*C*) towards the peak of the $I_{Ca,L}$ I-V relationship (Fig. 2-8*B*), promoting $I_{Ca,L}$ activation (Fig. 2-8*D*) and SR Ca^{2+} release (Fig. 2-8*E*). When I_{to1} is blocked in the cell, $I_{Ca,L}$ activation occurs at a V_m that is far from the peak of the I-V curve (Fig. 2-8*B*), decreasing peak $I_{Ca,L}$ (Fig. 2-8*D*) and SR Ca^{2+} release (Fig. 2-8*E*). For a propagating action potential, however, increased load decreases peak upstroke voltage so that it is near the peak of the I_{CaL} I-V curve (Fig. 2-8*B*, approximately 10 mV). Maximal $I_{Ca,L}$ activation occurs shortly after the peak upstroke V_m such that the depth of the phase 1 notch plays little role in determining V_m as $I_{Ca,L}$ is peaking. Consequently, block of I_{to1} in the strand has little effect on peak $I_{Ca,L}$ (Fig. 2-8*D*) and SR Ca^{2+} release (Fig. 2-8*E*). Furthermore, reduced phase 1 repolarization (Fig. 2-8*B*) due to reduced I_{to1} activation (Fig. 2-8*C*) also suggests a diminished importance of I_{to1} in the strand relative to the cell.

2.4.3 Ionic Mechanisms of APD restitution

APD restitution will determine the response of cells to the premature stimuli that trigger arrhythmia, and is thought to be a critical determinant of the stability of reentry after initiation. The ionic mechanisms underlying the kinetics of APD restitution remain incompletely understood, however. A series of simulations was performed to characterize the most important determinants of restitution kinetics in canine epicardial myocytes. Fig. 2-9*A* shows that the

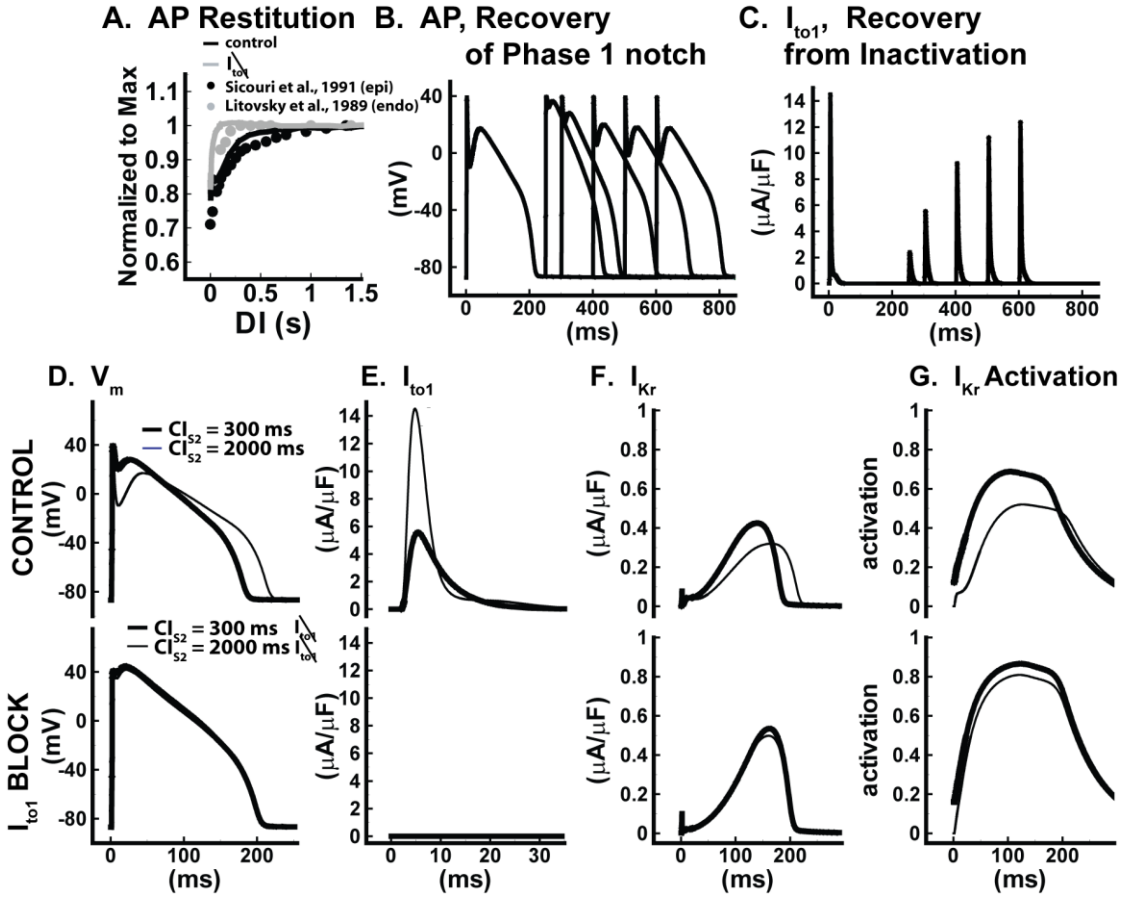

Figure 2-9 I_{to1} and APD Restitution. (A) APD (normalized to maximum) as a function of diastolic interval (DI), during restitution at CL_{S1} = 2 s in control and after 100% I_{to1} block in strand simulations. Results are compared to data from canine epicardial (Sicouri and Antzelevitch, 1991) and endocardial (Litovsky and Antzelevitch, 1989) tissue experiments. Recovery of (B) action potential phase 1 notch and (C) I_{to1} during restitution. (D) V_m , (E) I_{to1}, (F) I_{Kr} current and (G) I_{Kr} activation during APD restitution at S2 coupling intervals (CI_{S2}) of 0.3 and 2 s in control and after I_{to1} block in the strand. Action potential after I_{to1} block at short CI_{S2} (thick, gray) and long CI_{S2} (thin, gray) have nearly identical APD.

model time course of APD restitution is consistent with experiments in epicardial tissue (Sicouri and Antzelevitch, 1991). In canine epicardium, APD gradually increases as S2 coupling interval (CI_{S2}) increases beyond 0.3 s. When I_{to1} is blocked, the increase in APD with increasing DI is more abrupt, as observed in canine endocardium (Litovsky and Antzelevitch, 1989), consistent with the absence of I_{to1} in this tissue. Fig. 2-9*B* and Fig. 2-9*C* shows action potentials and I_{to1} during restitution in the model. Phase 1 notch depth is shallow at short DI, and gradually increases to its maximum depth at long DI (Fig. 2-9*B*). This increase in notch depth is the result of slow recovery of canine epicardial I_{to1} from inactivation (Fig. 2-9*C*), consistent with experiment (Liu et al., 1993). Figs. 2-9*D*-*G* examine the role that I_{to1} plays in APD restitution time course. At short CI_{S2}, I_{to1} has not fully recovered from inactivation (Fig. 2-9*E*, top) resulting in minimal phase 1 repolarization (Fig. 2-9*D*, top). As CI_{S2} increases, notch depth increases as I_{to1} recovers from inactivation. Increasing notch depth slows I_{Kr} activation (Fig. 2-9*G*, top) , since I_{Kr} activation is slower at negative voltages, leading to decreased I_{Kr} current at long CI_{S2} (Fig. 2-9*F*, top). The gradual increase in APD during restitution follows the slow time course of I_{to1} recovery and the suppression of I_{Kr} activation due to increasing notch depth. When I_{to1} is absent, phase 1 voltage does not change as CI_{S2} increases beyond 0.3 s (Fig. 2-9*D*, *bottom)*, I_{Kr} activation is constant at CI_{S2} greater than 0.3 s (Fig. 2-9*F-G*, *bottom)* and the gradual change in APD observed in epicardial tissue is absent (Fig. 2-9*A)*.

While block of I_{to1} eliminates the DI dependence of APD at $CI_{S2} > 0.3$ s, a substantial degree of APD shortening still occurs at $CI_{S2} < 0.3$ s. Additional simulations were performed to identify the ionic mechanisms responsible for APD shortening at $CI_{S2} < 0.3$ s. Fig. 2-10A demonstrates that with normal I_{Na}, APD shortens by 20% at the shortest DI, but with I_{Na} recovery kinetics eliminated (by resetting h and j gates to 1 to remove inactivation when the S2 is applied)

APD shortens by only 10%. Fig. 2-10B-C characterize normal I_{Na} recovery and its effect on membrane V_m during restitution. In control, incomplete I_{Na} recovery at short DI (Fig. 2-10C)

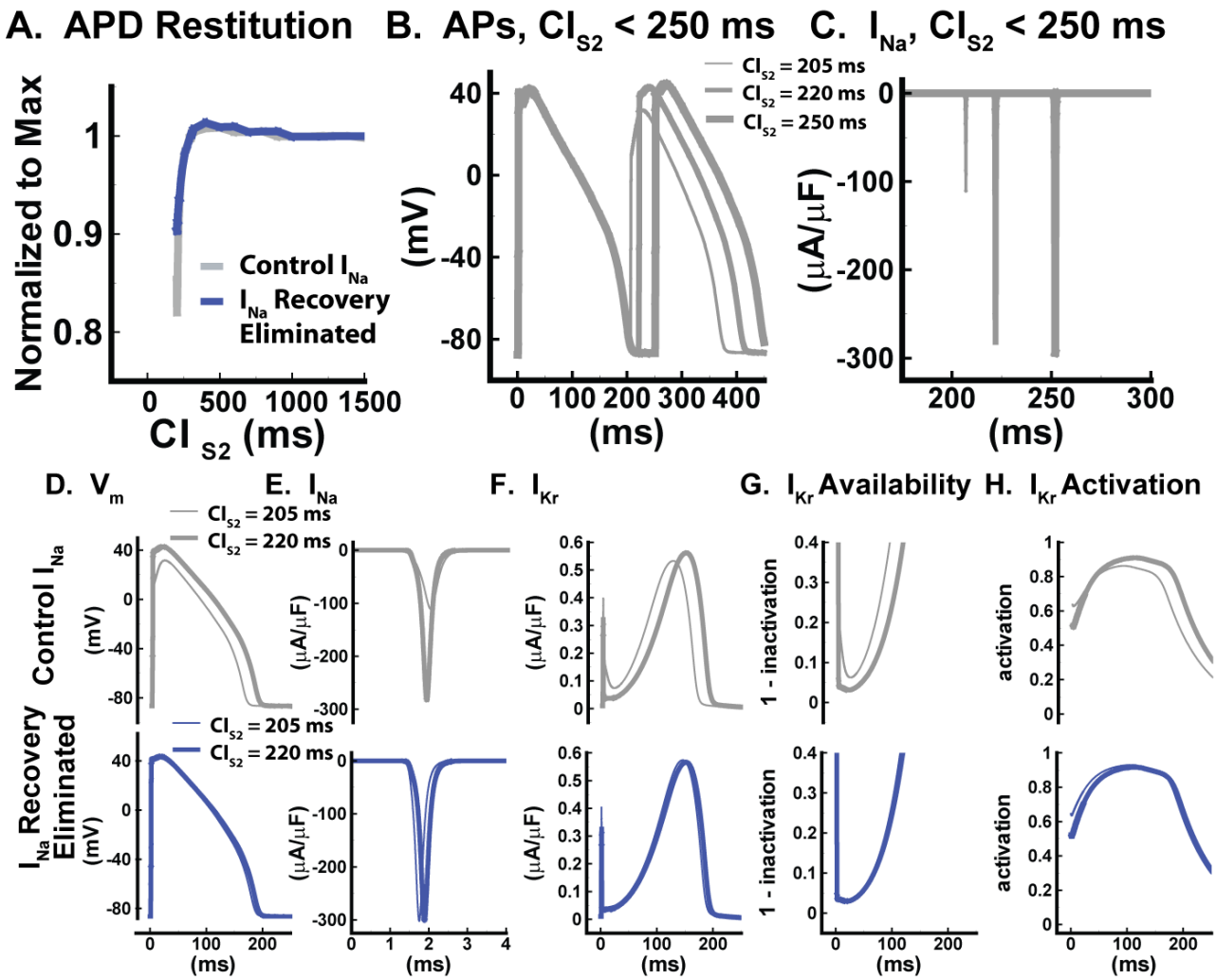

Figure 2-10 I_{Na} and APD Restitution. (A) APD (normalized to maximum) as a function of diastolic interval (CI_{S2}), during restitution at CL_{S1} = 2 s with normal I_{Na} and after elimination of recovery of I_{Na}. Recovery of I_{Na} was eliminated by resetting I_{Na} *h* and *j* gates to 0 upon application of the S2 stimulus. Simulations were performed with I_{to1} blocked to isolate the role of I_{Na}. Recovery of (B) V_m and (C) I_{Na} during restitution. (D) V_m , (E) I_{Na}, (F) I_{Kr} current, (G) I_{Kr} availability and (H) I_{Kr} activation during APD restitution at S2 coupling intervals (CI_{S2}) of 0.3 and 2 s with normal I_{Na} and after elimination of I_{Na} recovery. Action potential after I_{to1} block at short CI_{S2} (thick, gray) and long CI_{S2} (thin, gray) have nearly identical APD.

results in reduced early AP V_m (Fig. 2-10B). Maximum I_{Na} magnitude and upstroke V_m are reached within 50 ms after repolarization of the previous AP. The time constant of I_{Na} recovery from inactivation reflects model fit to data on the recovery of dV/dt_{max} in canine epicardial myocytes. Ionic mechanisms underlying the effects of I_{Na} recovery on APD are examined in Panels D-H. At short CI_{S2}, (CI_{S2} = 205 ms) incomplete recovery of I_{Na} (Fig. 2-10E, top) decreases early AP V_m (Fig. 2-10D, top) . Decreased early AP V_m leads to increased I_{Kr} availability (Fig. 2-10E G, top) and I_{Kr} current (Fig. 2-10F, top), promoting APD shortening. Although decreased membrane V_m also leads to slower I_{Kr} activation, the increase in I_{Kr} availability dominates and leads to net enhancement of I_{Kr}. The bottom panels in Figs. 2-10D-H confirm that elimination of I_{Na} recovery (Fig. 2-10E, bottom) reduces the CI_{S2} dependence of AP V_m, I_{Kr} availability, I_{Kr} current and APD.

The role of I_{Ks} in canine APD restitution is examined in Figure 2-11. Fig. 2-11A demonstrates that elimination of the CI_{S2} dependence of I_{Ks} activation (by resetting channels to the Zone 2 closed state *C1* when the S2 stimulus was applied) decreases APD shortening at premature CI_{S2} by 10%. Note that I_{to1} and I_{Na} recovery were eliminated in order to isolate the effect of I_{Ks} on restitution. Figs. 2-11 *B-F* examine the ionic mechanisms underlying the contribution of I_{Ks} to restitution. The 17 state I_{Ks} model can be divided into two open states, five *Zone 1* closed states that can activate rapidly and ten 'deep' *Zone 2* closed states which require slow transitions to *Zone 1* before activation is possible. At CI_{S2} = 205 ms, a significant fraction of channels activated during the S1 AP remain in *Open* states (Fig. 2-11 *D*), while an additional fraction occupy *Zone 1* (Fig. 2-11*F*) states. When a premature stimulus is applied, channels that are already in *Open* states and those moving rapidly from *Zone 1* to *Open* states combine to give prominent I_{Ks} activation (Fig. 2-11 *C*). Peak activation of I_{Ks} at CI_{S2} = 260 ms is markedly

increased relative to peak density at CI_{S2} = 300 ms. As DI increases, channels activated during the S1 stimulus move from *Zone 1* and *Open* states to *Zone 2*, resulting in less prominent I_{Ks}

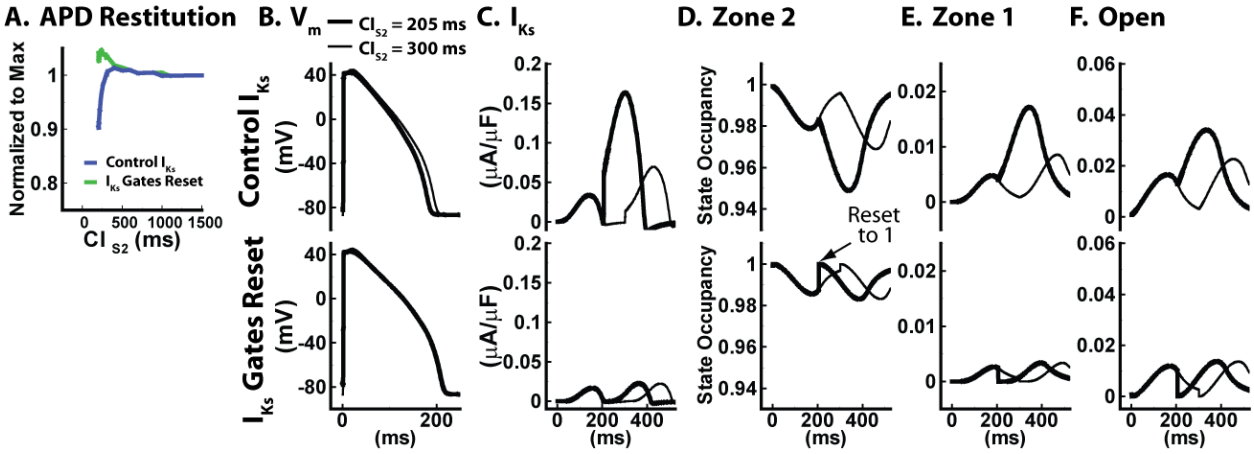

Figure 2-11 I_{Ks} and APD Restitution. (A) APD (normalized to maximum) as a function of diastolic interval (CI_{S2}), during restitution at CL_{S1} = 2 s with normal $I_{Ks}$and after elimination of recovery of I_{Ks}. Recovery of I_{Ks} was eliminated by resetting I_{Ks} states to *Zone 2* upon application of the S2 stimulus. Simulations were performed with I_{to1} blocked and I_{Na} recovery eliminated to isolate the role of I_{Ks}. (B) V_m , (C) I_{Ks}, and state occupancy of (D) *Zone 2*, (E) *Zone 1* and (F) *Open State* during APD restitution at S2 coupling intervals (CI_{S2}) of 205 and 300 ms with normal I_{Ks} (*top*) and after elimination of I_{Ks} recovery (*bottom*).

activation and reduced APD prolongation for more mature stimuli. The bottom panels of Figs. 2-11 B-E confirm the proposed role of I_{Ks} in APD shortening. If I_{Ks} channels are reset to Zone 2 when the S2 stimulus is applied, the rapid movement to Zone 1 and Open states during the S2 AP is eliminated. I_{Ks} activation is weak at CI_{S2} = 205 and 300 ms and the CI_{S2} dependence of APD is dramatically decreased. Note that when I_{to1} and the CI_{S2} dependence of I_{Na} and I_{Ks} are eliminated, APD no longer shortens at premature CI_{S2}. This result suggests that these three currents are the most critical determinants of APD shortening during restitution in canine epicardium.

2.4.4 Ionic Mechanisms of APD accommodation

Figure 2-12 describes important characteristics of APD accommodation in the canine epicardial model. The black trace in Fig. 2-12 A shows a steady state AP at CL_{S1} = 1000 ms. This APD also can be represented by the black circle on the APD adaptation curve in Fig. 2-12 B. The red trace in Fig. 2-12 A shows the 1st beat after pacing rate is changed to CL_{S2} = 500 ms. This APD can also be represented by the red circle on the restitution curve in Fig. 2-12 B.

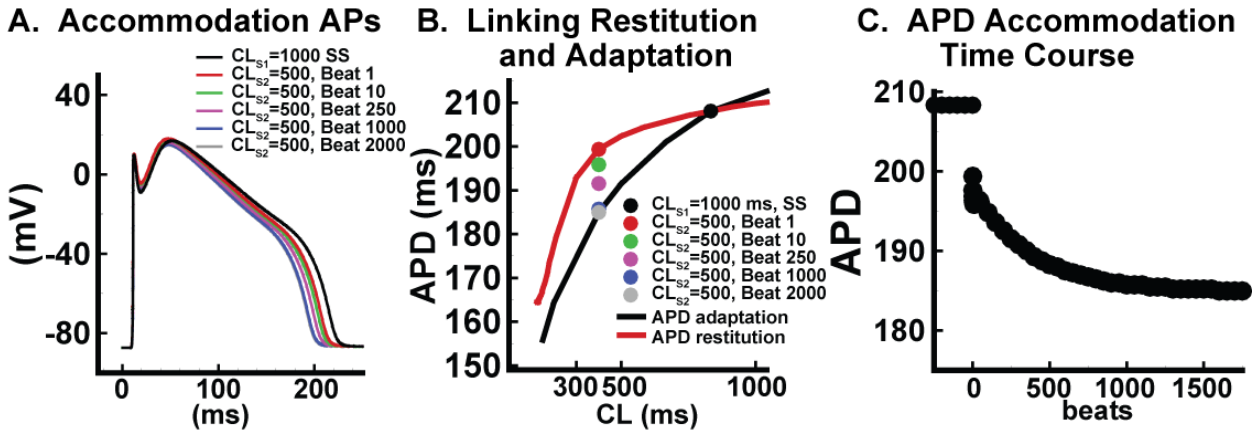

Figure 2-12 Linking Accommodation, Restitution and Adaptation. (A) Steady state APD at CL_{S1} = 1000, and selected action potentials after the transition from CL_{S1} = 1000 ms to CL_{S2} = 500 ms. (B) APD adaptation, APD restitution at CL_{S1} = 1000 ms, and APDs for selected beats after the transition from CL_{S1} = 1000 ms to CL_{S2} = 500 ms. (C) The time course of APD accommodation after a the transition from CL_{S1} = 1000 ms to CL_{S2} = 500 ms.

Green, blue, and magenta traces in Fig. 2-12 A and points in Fig. 2-12B show APs and APDs for the transition from steady state at CL_{S1} = 1000 ms to steady state at CL_{S2} = 500 ms (gray trace or circle). The transition from steady state at CL_{S1} = 1000 ms to steady state at CL_{S2} = 500 ms can therefore be thought of as consisting of two processes; 1) restitution, the APD shortening that occurs for the 1st beat at the new CL_{S2} and 2) accommodation, which describes further APD shortening after the 1st beat. Fig. 2-12C shows that approximately 2000 beats (1000 seconds) of pacing are required to reach steady state at CL_{S2}. The qualitative features relating APD adaptation and restitution via APD accommodation described in the model are consistent with

observations in a large range of tissue and preparations. As shown in Fig. 2-12B, the slope of the APD adaptation curve is steeper than that of the APD restitution curve at their intersection, since accommodation leads to APD shortening after a change to a shorter CL_{S2}. This relationship between the slope of restitution and adaptation has been observed in, for example, canine endocardium (Cherry and Fenton, 2006; Elzinga et al., 1981), canine ventricular epicardial tissue (Elzinga et al., 1981; Han and Moe, 1969), human ventricular epicardium (Franz et al., 1988) and bullfrog myocardium (Kalb et al., 2004). The time required for APD to reach steady state after a change in CL ranges from 1-3 (Franz et al., 1988; Lux and Ershler, 2003; Saitoh et al., 1988; Williams et al., 1999) to as many as 5-10 (Saitoh et al., 1988) minutes. While accommodation is a widely observed phenomenon and may play a role in the dynamics of fibrillation (Baher et al., 2006; Toal et al., 2009), the phenomena is poorly understood and is not reproduced by many available models (Baher et al., 2006).

The ionic mechanisms of APD accommodation are explored in Figure 2-13. When the pacing CL is changed from 1000 to 500 ms, APD decreases abruptly at the 1st beat, than decreases over a time course of minutes until reaching steady state at the new CL (Fig. 2-13A). Figure 2-13B demonstrates that $[Na^+]_i$ approaches steady state at the new CL with a similar time course. We therefore hypothesized that this $[Na^+]_i$ increase was the primary cause of APD decrease during accommodation. Consistent with this hypothesis, clamp of $[Na^+]_i$ to its steady state value at CL = 500 ms eliminates accommodation during the transition from CL = 1000 ms to CL = 500 ms. Further analysis was performed to investigate the ionic determinants of $[Na^+]_i$ increase and equilibration at the new CL. At steady state at CL = 1000 ms, Na^+ influx and efflux are matched (Fig. 2-13 C). Influx and efflux were calculated for each cycle in terms of the change in $[Na^+]_i$ divided by the cycle length. Figure 2-13 D shows that I_{NaCa}, I_{Na}, I_{NaL} and

background fluxes (I_{Nab} and I_{NaL}) are the sources of Na^+ influx in canine ventricular myocytes, while I_{NaK} is the only source of Na^+ efflux. After CL changes to 500 ms, Na^+ influx exceeds

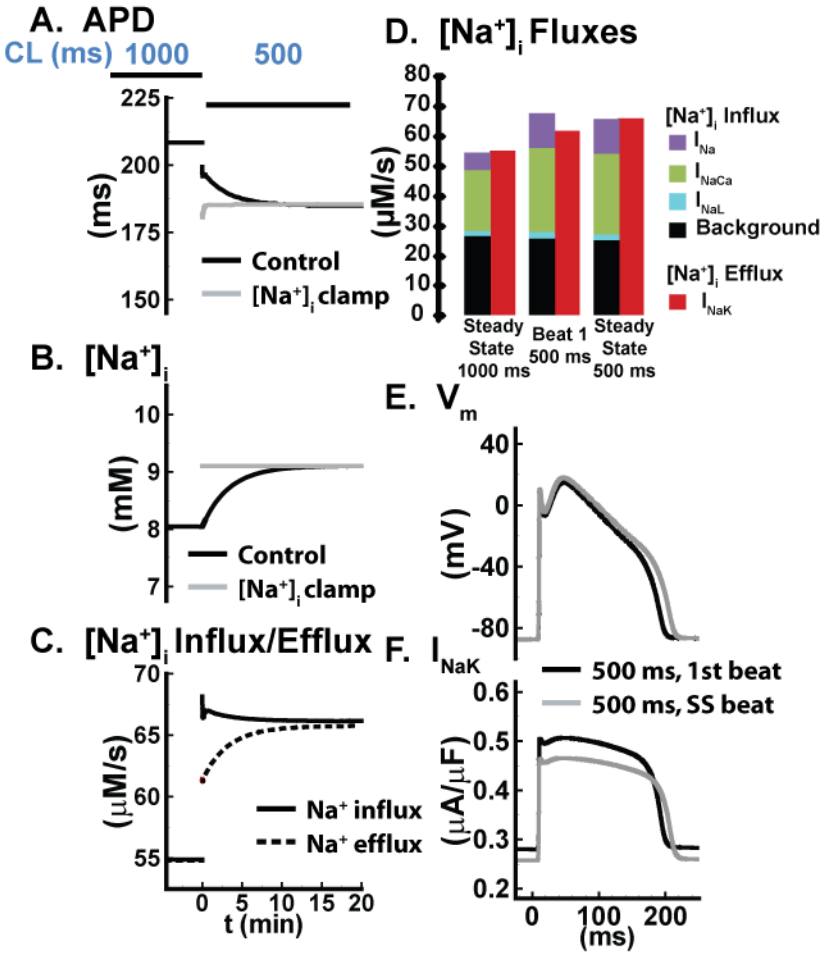

Figure 2-13 $[Na^+]_i$, I_{NaK} and APD Accommodation. Accommodation of (A) APD and (B) $[Na^+]_i$ after a change in CL from 1 s to 0.5 s in control and with $[Na^+]_i$ clamped to its steady-state value at CL = 0.5 s. (C) Integrated Na^+ fluxes calculated for each beat during the transition from steady-state at CL = 1 s to steady-state at CL = 0.5 s. Integrated Na^+ influx was calculated as $I_{NaCa} + I_{Na} + I_{NaL} + I_{Nab} + CT_{NaCl}$ and Na^+ efflux as I_{NaK}. (D) Components of integrated Na+ influx and efflux at steady state CL_{S1} = 1000 ms, beat 1 at CL_{S2} = 500 ms and steady state at CL_{S2} = 500 ms. (E) Vm and (F) I_{NaK} for the 1st beat and a steady-state (SS) beat after a change in CL from 1 s to 0.5 s.

efflux until Na^+ influx increases to match efflux and $[Na^+]_i$ reaches equilibrium. After a change from CL = 1000 ms to CL = 500 ms, Na^+ flux via I_{NaCa} and I_{Na} increase, but this increase is not

matched by the increase in I_{NaK}. The shorter DI at the faster CL prevents I_{NaK} from extruding the $[Na^+]_i$ that enters the cell during the action potential, primarily via I_{Na} and I_{NaCa}. The net Na^+ influx drives an increase in $[Na^+]_i$, which promotes increased I_{NaK} activity until influx and efflux match. The increase in I_{NaK} activity increases the net outward current from the 1st to the SS beat at CL = 500 ms (Fig. 2-13 F), providing the primary mechanisms for APD accommodation.

A recent experimental study has shown that block of I_{CaL} dramatically attenuates APD accommodation in rabbit myocytes (Tolkacheva et al., 2006). Fig. 2-14A demonstrates that block of I_{CaL} also attenuates APD accommodation in the canine epicardial model during a CL change from 1000 to 500 ms. This attenuation of APD accommodation is accompanied by a decrease in the degree of $[Na^+]_i$ accumulation (Fig. 2-14B). Fig. 2-12C demonstrates that this

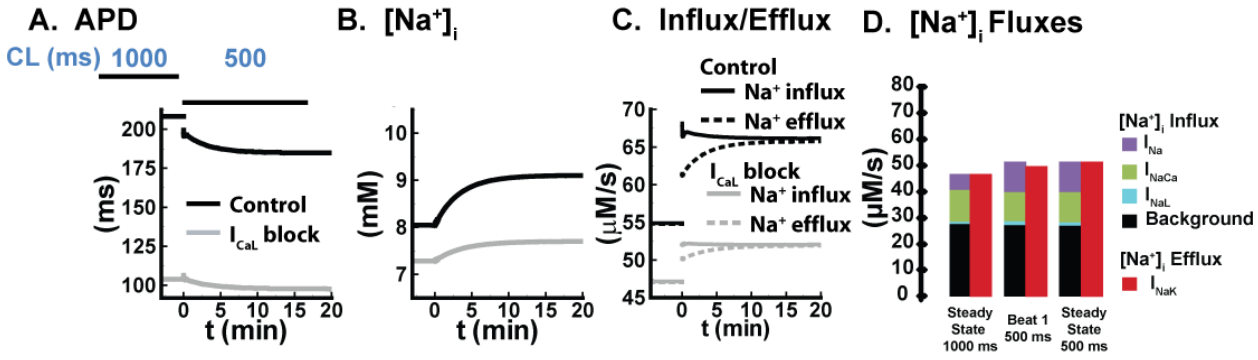

Figure 2-14 I_{CaL} and APD Accommodation. Accommodation of (A) APD and (B) $[Na^+]_i$ after a change in CL from 1 s to 0.5 s in control and I_{CaL} blocked. (C) Integrated Na^+ fluxes calculated for each beat during the transition from steady-state at CL = 1 s to steady-state at CL = 0.5 s in control and with I_{CaL} blocked. Integrated Na^+ influx was calculated as $I_{NaCa} + I_{Na} + I_{NaL} + I_{Nab} + CT_{NaCl}$ and Na^+ efflux as I_{NaK}. (D) Components of integrated Na^+ influx and efflux at steady state CL_{S1} = 1000 ms, beat 1 at CL_{S2} = 500 ms and steady state at CL_{S2} = 500 ms after I_{CaL} block.

decrease in $[Na^+]_i$ accumulation is caused by a decreased imbalance between Na^+ influx and efflux after the transition to CL = 500 ms. Fig. 2-14D examines the contributions of ion channels and exchangers to the decreased imbalance in Na^+ fluxes after a change to CL = 500

ms. In control (Fig. 2-14D), transition to a faster CL results in a large increase in I_{NaCa} Na^+ influx. This increase in I_{NaCa} forward mode activity (Na^+ entry/Ca^{2+} efflux) is driven by increased Ca^{2+} influx via I_{CaL} at the faster rate. Ca^{2+} influx increases because a similar degree of I_{CaL} Ca^{2+} entry occurs during the AP at the faster CL, but this similar amount of Ca^{2+} entry occurs during a shorter CL. When I_{CaL} is blocked, Ca^{2+} efflux does not increase at the faster rate and the increase in Na^+ influx due to increased I_{NaCa} Na^+ entry at the faster rate is attenuated, leading to decreased Na^+ accumulation and APD accommodation.

2.4.5 Ionic Mechanisms of APD adaptation

The analysis of APD restitution and accommodation provided above leads to a clearer understanding of the ionic mechanisms underlying APD adaptation as demonstrated in Figure 2-15. The DI dependence of I_{Kr} (Fig. 2-15 B) due to mechanisms described in the above section

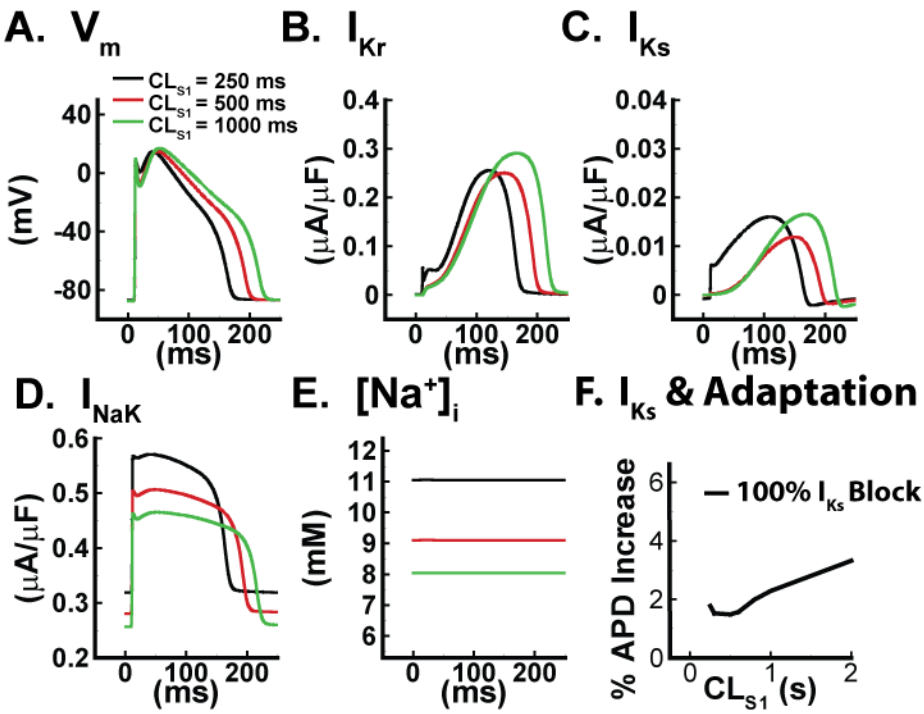

Figure 2-15 Mechanism of APD adaptation. V_m, I_{Kr}, I_{Ks}, I_{NaK} and $[Na^+]_i$ at steady state CL_{S1} = 250, 500 and 1000 ms. (F) APD prolongation after I_{Ks} block as a function of CL_{S1}.

on restitution leads to increased I_{Kr} magnitude and promotes APD shortening at CL_{S1} = 250 ms. The accumulation of $[Na^+]_i$ that occurs with sustained pacing at fast CL_{S1} (Fig. 2-15E) described in the above section on accommodation leads to increased I_{NaK} (Fig. 2-15D), which also promotes APD shortening at CL_{S1} = 250 ms. Although accumulation of I_{Ks} in Open and Zone 1 states at short DI does increase I_{Ks} activation at CL_{S1} = 250 ms, block of I_{Ks} reveals that this current plays a limited in role in adaptation. While elimination of I_{Ks} DI dependence can lead to an approximately 10% increase in APD at the shortest DI during restitution (Fig. 2-15A), APD increases by < 2% after I_{Ks} block at CL_{S1} = 250 ms. It is important to note that the processes of restitution and accommodation are not independent. For instance, sustained pacing at fast CL_{S2} shortens APD via accommodation, which in turn tends to prolong DI (DI = CL_{S2} - APD) and lengthen APD via restitution. However, in spite of their interdependence, studying the two processes separately provides important insight into ionic mechanisms of APD rate dependence.

2.4.6 Ionic Mechanisms of S1 Dependent APD Restitution

Several experimental studies have shown that the APD restitution curve shifts to shorter APD as basic pacing CL decreases (Boyett and Jewell, 1978; Cherry and Fenton, 2007; Elzinga et al., 1981; Han and Moe, 1969). The S1 dependence of restitution may play a role in the stability of fibrillation (Baher et al., 2006), but many recently published models fail to reproduce this phenomena (Cherry and Fenton, 2006). Consistent with experimental observations, our model reproduces the dependence of restitution on the rate of S1 pacing (Fig. 2-16). The level of $[Na^+]_i$ during restitution depends on CL_{S1}, with pacing at fast CL_{S1} leading to $[Na^+]_i$ accumulation during accommodation (Fig. 2-16) as described above APD. Fig. 2-16C and Fig. 2-16D show APs and I_{NaK} for a range of CL_{S1}, but with CL_{S2} held constant, in order to eliminate restitution dependent effects on APD. The shortening of APD with decreasing CL_{S1} in Fig. 2-

16C results from the increase in I_{NaK} activity in Fig. 2-16D, which is in turn due to the CL_{S1}

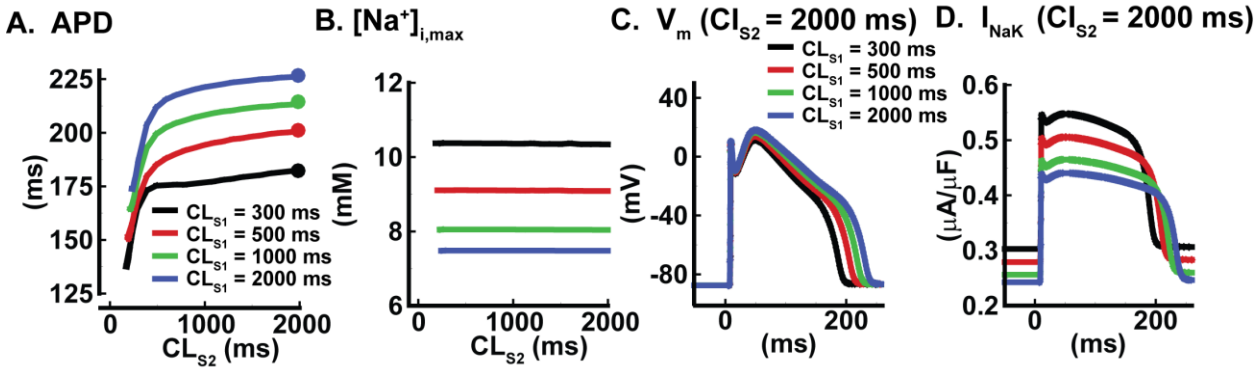

Figure 2-16 Mechanism of S1 Dependent APD Restitution. S1 dependence of (A) APD restitution and (B) $[Na^+]_{i,max}$. (C) V_m and (D) I_{NaK} at CI_{S2} = 2000 ms and CL_{S1} = 300, 500, 1000 and 2000 ms.

dependence of to $[Na^+]_i$ shown in Fig. 2-16B.

Fig. 2-17 examines the S1 dependence of APD restitution kinetics in model and experiment. Panels 2-17A-D demonstrate that the model reproduces the kinetics of APD restitution at CL_{S1} = 2000, CL_{S1} = 1000, CL_{S1} = 500 and CL_{S1} = 333 ms. Comparison at CL_{S1} = 2 s (Fig. 2-17*A*) is to left ventricular (LV) epicardial tissue experiment (Elzinga et al., 1981; Sicouri and Antzelevitch, 1991), while CL_{S1} = 1 s (Fig. 2-17*B*), 0.5 s (Fig. 2-17*C*) and 0.333 s (Fig. 2-17*D*) is to right ventricular (RV) epicardial tissue experiment (Elzinga et al., 1981; Sicouri and Antzelevitch, 1991) because left ventricular data at these rates were not available. Fig. 2-17E and Fig. 2-17F demonstrate that model and experimental restitution kinetics show a small dependence on CL_{S1}. Differences in restitution kinetics between the model and the RV experiments are relatively small and may be due to differences in LV and RV I_{to1} expression and kinetics (Di Diego et al., 1996), Ca^{2+} handling or other heterogeneities. Additional simulations (not shown) suggest that rate dependent SR Ca^{2+} loading and Ca^{2+} release can have significant effects on APD restitution. S1 dependent SR Ca^{2+} loading and Ca^{2+} release and the effects of

this S1 dependent Ca^{2+} release on APD are underexplored and poorly understood phenomena and should be explored in future modeling and experimental studies.

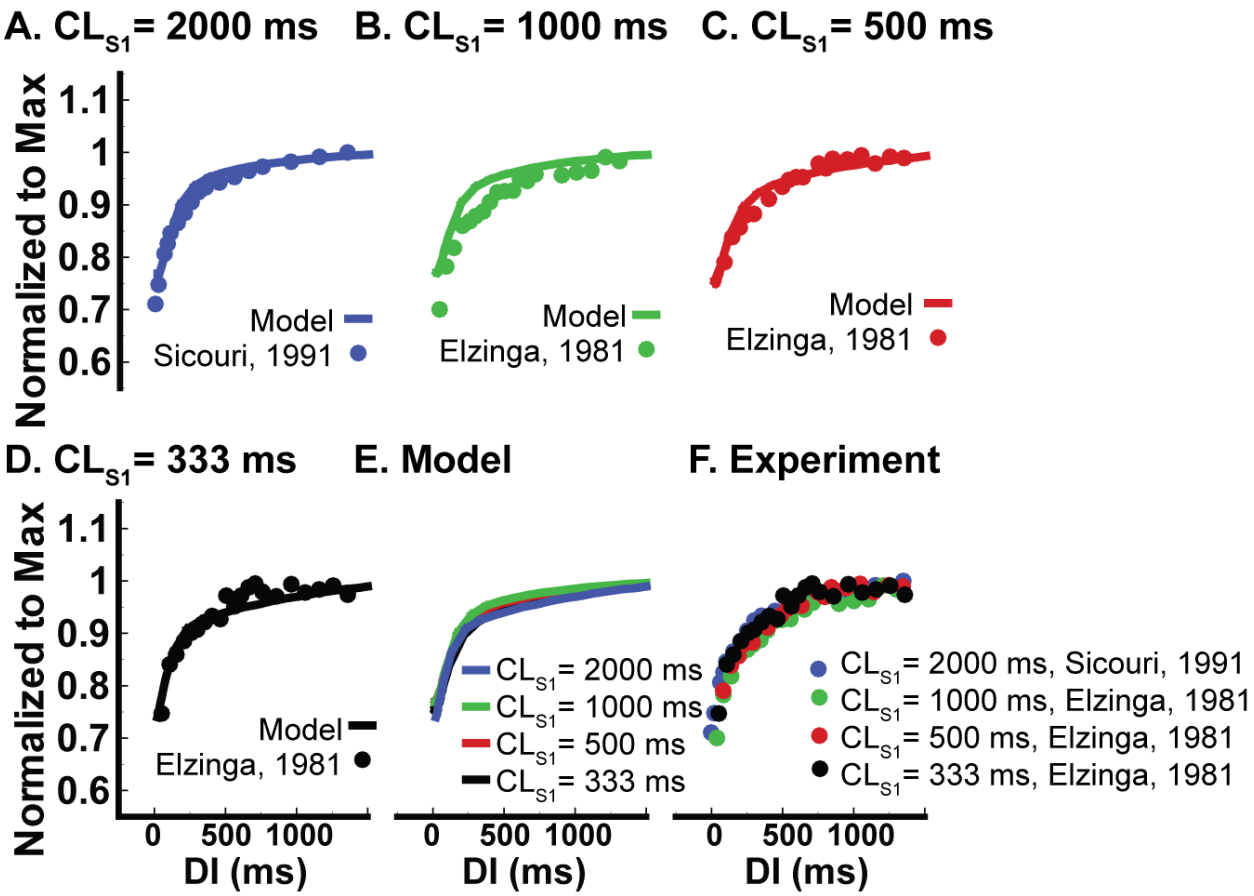

Figure 2-17 Rate Dependence of APD Restitution Kinetics. APD restitution time course in model and experiment at (A) CL_{S1} = 2000 ms, (B) CL_{S1} = 1000 ms, (C) CL_{S1} = 500 ms and CL_{S1} = 333 ms. Comparison of APD restitution kinetics in model (E) and experiment (F)

2.5 Discussion

The rate dependent phenomena examined in this study are thought to play an important role in the dynamics of arrhythmia (Baher et al., 2007; Karma, 1994; Mironov et al., 2008). The model presented here reproduces experimentally observed APD adaptation, restitution and accommodation in both cell and tissue. While the rate dependence of model APD, CaT and $[Na^+]_i$ accumulation are similar in cell and strand, our simulation results show that the effects of I_{to1} block on ion accumulation differ. Other simulation results (Qu, 2004) have suggested that

APD restitution kinetics and the transition to APD alternans and more complex excitation patterns in cell and tissue also differ. Taken together, these results suggest that experimental results in isolated myocytes should be extrapolated to the multicellular tissue with caution.

Recent studies have emphasized limitations in our mechanistic understanding of the rate dependence of action potential duration (Cherry and Fenton, 2007). The detailed, physiologically based mathematical descriptions of critical ionic currents, pumps and exchangers incorporated into the model lead to novel insight into underlying ionic mechanisms. Specific mechanistic insights generated by our study include: i.) I_{to1} potentiates $I_{Ca,L}$ and SR Ca^{2+} release during early AP repolarization in isolated cells but not in multicellular tissue. ii.) I_{to1} plays an important role in APD restitution due to its slow recovery kinetics. As DI increases, I_{to1} recovery and phase 1 notch depth increase, suppressing I_{Kr} activation and lengthening APD. iii.) I_{Ks} plays a limited role in repolarization of paced APs, but plays an important role in APD shortening for premature stimuli. iv.) $I_{Ca,L}$ plays a critical role in APD accommodation and memory. As a response to Ca^{2+} entry via $I_{Ca,L}$ at fast rates, forward mode I_{NaCa} increases, leading to increased Ca^{2+} efflux and Na^{+} influx. Sodium accumulation increases repolarizing I_{NaK}, thereby shortening APD during accommodation. v.) $I_{Ca,L}$ dependent increase in $[Na^{+}]_i$ and I_{NaK} at fast rates is responsible for the shift in APD restitution curves towards shorter APD.

Previous experiments and simulation studies have suggested that I_{to1}, by increasing phase 1 repolarization, increases peak $I_{Ca,L}$ (the trigger for SR release) and consequently SR Ca^{2+} release (Greenstein et al., 2000; Sah et al., 2002). These studies showed enhanced $I_{Ca,L}$ and SR Ca^{2+} release when phase 1 repolarization increases the $I_{Ca,L}$ driving force. While this scenario is relevant to an isolated, directly stimulated myocyte, model simulations indicate that it does not apply to the situation *in vivo*, where electrotonic loading from neighboring cells weakens the AP

upstroke. Our simulations suggest that, for propagating APs, I_{to1}-dependent phase 1 repolarization has little effect on peak $I_{Ca,L}$ and SR Ca^{2+} release. In addition, simulations show that the weakened AP upstroke in the tissue decreases I_{to1} activation and phase 1 repolarization. I_{to1} has been accorded a role in conduction (Huelsing et al., 2001; Wang et al., 2000) and in electrophysiological remodeling in various diseased states (Kaab et al., 1996; Lue and Boyden, 1992; Yu et al., 1999). Our results suggest that predictions of the effect of I_{to1} and I_{to1} block based on single cell simulations and experiments may not apply to the *in vivo* situation. In contrast, model simulations predict that I_{to1} plays a significant role in APD restitution. The interplay between I_{Kr} activation and the slow recovery kinetics of I_{to1} leads to a gradual increase in APD during restitution, while I_{to1} block results in a more abrupt APD increase. This result provides a mechanistic explanation for the correlation between notch depth and APD observed in canine ventricular tissue (Litovsky and Antzelevitch, 1989). The time course of APD restitution is thought to play an important role in the stability of ventricular arrhythmias (Karma, 1994). Our results suggest that experimentally observed heterogeneity in I_{to1} density and recovery kinetics (Oudit et al., 2001; Patel and Campbell, 2005) may play a role in the stability of arrhythmias in different species, regions of tissue or pathophysiological states. Canine experiments have shown transmural heterogeneity in I_{NaL} (Zygmunt et al., 2000), I_{to1} (Liu et al., 1993), I_{Ks} (Liu and Antzelevitch, 1995) and I_{NaCa} (Zygmunt et al., 2001). The epicardial model accurately reproduces endocardial restitution kinetics after blocking only I_{to1}, suggesting that I_{to1} is the dominant determinant of heterogeneity in restitution between the two cell types.

Experimental measurements of the effect of I_{Ks} block on APD in canine ventricle have ranged from near 0 (Stengl et al., 2003) to as much as 30% (Shimizu and Antzelevitch, 1998). Varro et al. (Varro et al., 2001) report a modest prolongation (3-7%) and biphasic CL

dependence after chromanol block, consistent with our simulation results. Although the role of I_{Ks} in repolarization remains controversial, LQT mutations linked to genes for I_{Ks} α- and β-subunits (Splawski et al., 1997) argue for an important role in repolarization. Our simulations demonstrate that slow activation and relatively low density limit the role of I_{Ks} in AP repolarization at physiological heart rates in the absence of β-adrenergic stimulation, consistent with our previous modeling studies (Hund and Rudy, 2004). Simulations with a detailed Markov model of I_{Ks} predict an important role for I_{Ks} in APD restitution. During deactivation, channels accumulate in closed states (Zone 1) where rapid activation in response to a premature stimulus is possible, leading to an important role for I_{Ks} in APD restitution at short DI. A role for I_{Ks} in APD shortening at fast CL_{S1} via accumulation in closed states has been previously shown in the guinea pig and human (Silva and Rudy, 2005). While major differences exist between I_{Ks} density and kinetics in guinea pig and canine, the mechanism for enhanced participation of I_{Ks} at fast CL_{S1} during adaptation and at short DI during restitution are similar in the two species. Importantly, while large density in the guinea pig ensures an important role for I_{Ks} at all rates, we find that I_{Ks} plays a major role in canine restitution at short DI, despite a limited role at longer physiological CL. While the effect of I_{Ks} block on paced APs has been studied experimentally, no studies on the role of I_{Ks} in restitution have been reported. I_{Ks} is also likely to play an important role in repolarization in the presence of β-adrenergic stimulation (Volders et al., 2003) or for abnormally prolonged APD (Varro et al., 2001).

Recent simulations have addressed the role of APD accommodation and short-term memory in the dynamics of arrhythmia (Baher et al., 2007; Boyett and Jewell, 1978; Mironov et al., 2008). Both simulations (Baher et al., 2007) and experiments (Tolkacheva et al., 2006) have emphasized uncertainty in the ionic mechanisms underlying this phenomenon. The results

presented here predict a major role for $I_{Ca,L}$ driven $[Na^+]_i$ accumulation in this phenomenon. A role for $[Na^+]_i$ and I_{NaK} in gradual APD changes during long-term pacing has been previously proposed (Boyett and Jewell, 1978; Faber and Rudy, 2000; Hund and Rudy, 2000). Similarities between the effect of block of $I_{Ca,L}$ and SR function in simulation and experiment (Tolkacheva et al., 2006) provide support for this hypothesis. While a similar time course of APD accommodation after a CL change has been observed in a range of preparations, APD accommodation in other species and preparations is often more rapid (Franz et al., 1988; Tolkacheva et al., 2006; Williams et al., 1999). This suggests that other mechanisms may play a role or, alternatively, that additional experiments are required to improve our understanding of equilibration of $[Na^+]_i$ and $[Ca^{2+}]_i$ during long term pacing. A role for $I_{Ca,L}$ in the dynamics of arrhythmia has been proposed by many investigators, usually through effects on APD restitution (Boyett and Jewell, 1978; Qu et al., 1999). Our simulations suggest that the effect of $I_{Ca,L}$ on $[Na^+]_i$ and APD accommodation should also be considered. The importance of $[Na^+]_i$ in determining the rate dependence of APD also points to an important limitation of simplified computational models, where intracellular ion concentrations are often held constant.

The predictive value of multicellular simulations of arrhythmia depends on the ability of cell models to reproduce experimental observation. Despite variability across species, cell type and preparation, APD adaptation, restitution and accommodation are qualitatively similar in many species. Our model examines the ionic basis of these rate dependent phenomena in the canine, but may provide insight into ionic mechanisms in other species including human. In addition, our model will provide a valuable tool for linking initiation and maintenance of arrhythmia to underlying cellular processes and ionic currents through multicellular simulations.

Chapter 3. Ionic Mechanisms of Electrophysiological Heterogeneity and Block in the Infarct Border Zone

3.1 Introduction

Survivors of myocardial infarction are at an increased risk of ventricular arrhythmia in the days and weeks that follow the initial ischemic event. Years of experiments have been devoted to increasing our understanding of the pathophysiological basis for this enhanced risk (Janse and Wit, 1989; Wit and Janse, 1992). A large body of research has focused on a canine model in which a transmural infarct is created by ligation of the left anterior descending coronary artery (LAD) (Dillon et al., 1988; El-Sherif et al., 1977b; El-Sherif et al., 1977c; Gough et al., 1985; Ursell et al., 1985). Arrhythmias in this model are reentrant in nature and have been mapped to a thin rim of surviving epicardial tissue that borders the infarct (the epicardial border zone or EBZ) (El-Sherif et al., 1977c). Initiation and maintenance of arrhythmia are thought to depend on the presence of a structurally and electrophysiologically remodeled substrate with enhanced vulnerability to a triggering event (Pinto and Boyden, 1999). Numerous studies have characterized remodeling of ion channels (Aggarwal and Boyden, 1995; Aggarwal et al., 1997; Baba et al., 2005; Dun et al., 2004; Dun and Boyden, 2005; Jiang et al., 2000; Lue and Boyden, 1992; Pu and Boyden, 1997), Ca^{2+} handling (Licata et al., 1997; Pu et al., 2000) and gap junctions (Cabo et al., 2006; Peters et al., 1997; Yao et al., 2003) in the EBZ 3–5 days post-infarction. The clinical importance of arrhythmia and the wealth of experimental data characterizing arrhythmias and remodeling make the EBZ an excellent paradigm for computational modeling studies aimed at elucidating the underlying ionic mechanisms.

Transitions between successful conduction, formation of the initial line of block, reentry and fibrillation depend on the heterogeneous response of healthy and diseased cells to complex

myocardial activation patterns. Our recently published computational model (Decker et al., 2009) accurately reproduces the response of the canine ventricular epicardial cell to a range of relevant pacing protocols. Starting from this control model, an EBZ myocyte model was developed based on experimental remodeling data. We tested the hypothesis that ion channel remodeling results in heterogeneity in the rate dependence of normal zone (NZ) and EBZ APD and refractoriness. Simulations using a multi-cellular model of heterogeneous myocardium were used to study the link between EBZ remodeling and the VW. In addition, we tested the hypothesis that ion channel remodeling combined with gap junction uncoupling leads to abnormal, unsafe conduction in the EBZ. The potential of gene therapy using a skeletal muscle sodium channel isoform (SkM1-I_{Na}) in the prevention of arrhythmia post-infarction (Lau et al., 2009) was also explored.

3.2 Methods

NZ and EBZ cell models were paced for 1800 s at a given S1 cycle length (CL_{S1}) with a conservative K^+ stimulus (Hund et al., 2001) (magnitude = -80 μA/μF, duration = 0.5 ms) to achieve steady state. Previous studies from our laboratory have used strand models to gain insight into the ionic mechanisms of propagation and conduction block (Shaw and Rudy, 1995, 1997). In this study, strands were composed of 96 serially arranged cells connected by gap junctions, with direct stimulation of cell 1 (magnitude = -200 μA/μF, duration = 1 ms). Parameter values used in the present study and detailed validation of the strand model of propagation are found in (Shaw and Rudy, 1997). Simulations were performed in homogeneous (96 NZ or 96 EBZ cells) or heterogeneous (48 NZ followed by 48 EBZ cells) strands. To achieve steady state, strands were paced for 1800 s at a given CL_{S1}. Restitution was studied with a single additional beat at the S2 coupling interval (CI_{S2}) after pacing to steady state at a given

CL_{S1}. In simulations where SkM1-I_{Na} was added to the EBZ region, SkM1-I_{Na} density (1.65 mS/μF) was adjusted to reproduce the experimentally observed 80% increase in EBZ dV/dt_{max} after SkM1-I_{Na} injection (Lau et al., 2009).

The effective refractory period (ERP) was defined as the smallest CI_{S2} for which AP propagation was successful. Post-repolarization refractoriness (PRR) was defined as ERP – APD. The vulnerable window (VW) for conduction block at the NZ to EBZ transition was used as a quantitative measure of vulnerability to formation of the initial line of conduction block, a prerequisite for initiation of reentry in infarcted myocardium. For pacing at a constant CL_{S1}, the VW was defined as the range of CL_{S1} for which conduction block occured at the NZ to EBZ transition. For restitution protocols, VW was defined as the range of CI_{S2} for which conduction block occured at the NZ to EBZ margin.

Safety factor (SF) indicates the margin of safety of action potential (AP) propagation, and is a useful quantitative measure of conduction safety (Shaw and Rudy, 1997). A detailed description and discussion of the method for calculating SF is included in (Shaw and Rudy, 1997). Briefly, SF for a cell during propagation is defined as:

$$SF = \frac{Charge\ \ generated\ \ \ by\ cell\ \ excitation}{Charge\ \ received\ \ \ for\ \ excitation} = \frac{\int_A\ I_C \cdot dt + \int_A\ I_{out} \cdot dt}{\int_A\ I_{in} \cdot dt} \quad A|Q_m > 0$$

where I_C is the capacitative current of the cell of interest, I_{out} is the axial current between the cell of interest and its downstream neighbor, I_{in} is the axial current received by the cell of interest from its upstream neighbor and Q_m is the time integral of transmembrane current. The integration limit A ($Q_m>0$) used to calculate SF denotes the time period during which the cell has completed its sink-source cycle. The fraction of SF>1 indicates the relative safety of conduction, while conduction fails for SF<1 (Shaw and Rudy, 1997).

3.3 Results

3.3.1 An Ionic Model of the Epicardial Border Zone myocyte

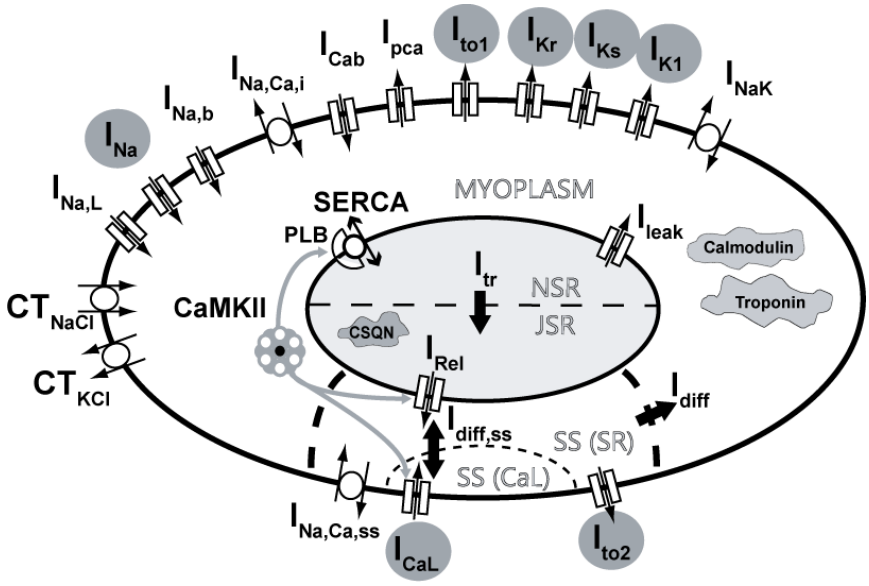

Figure 3-1 Canine Epicardial Border Zone (EBZ) cell model. Remodeled Epicardial Border Zone currents are circled in gray.

A model of the epicardial border zone myocyte was derived from the control (normal zone or NZ) model by incorporating myocyte remodeling data from 3-5 day old canine infarct preparations. Remodeled currents incorporated into the EBZ model are circled in gray in Figure 3-1. Modifications to the original epicardial cell model are described in Appendix B. Figure 3-2 shows a comparison between model-generated and experimentally recorded EBZ remodeling data. Reduction of I_{Na} density and leftward shift in I_{Na} steady state inactivation result in a reduced maximum AP upstroke velocity (Fig. 3-2*A*, *left*) and increased time constant of recovery of AP upstroke velocity ($\tau_{recovery}$, Fig. 3-2*A*, *right*), quantitatively consistent with experiment (Lue and Boyden, 1992). Figure 3-2*B* shows that the model reproduces the reduced L-type Ca^{2+} channel current (I_{CaL}) (Fig. 3-2*B*, *left*) and faster I_{CaL} voltage dependent inactivation (τ_{VDI}) (Fig. 3-2*B*, *right*) recorded in the EBZ (Aggarwal and Boyden, 1995). Figure 3-2*C* and Figure 3-2*D*

show reductions in the magnitude of K^+ (Lue and Boyden, 1992) and

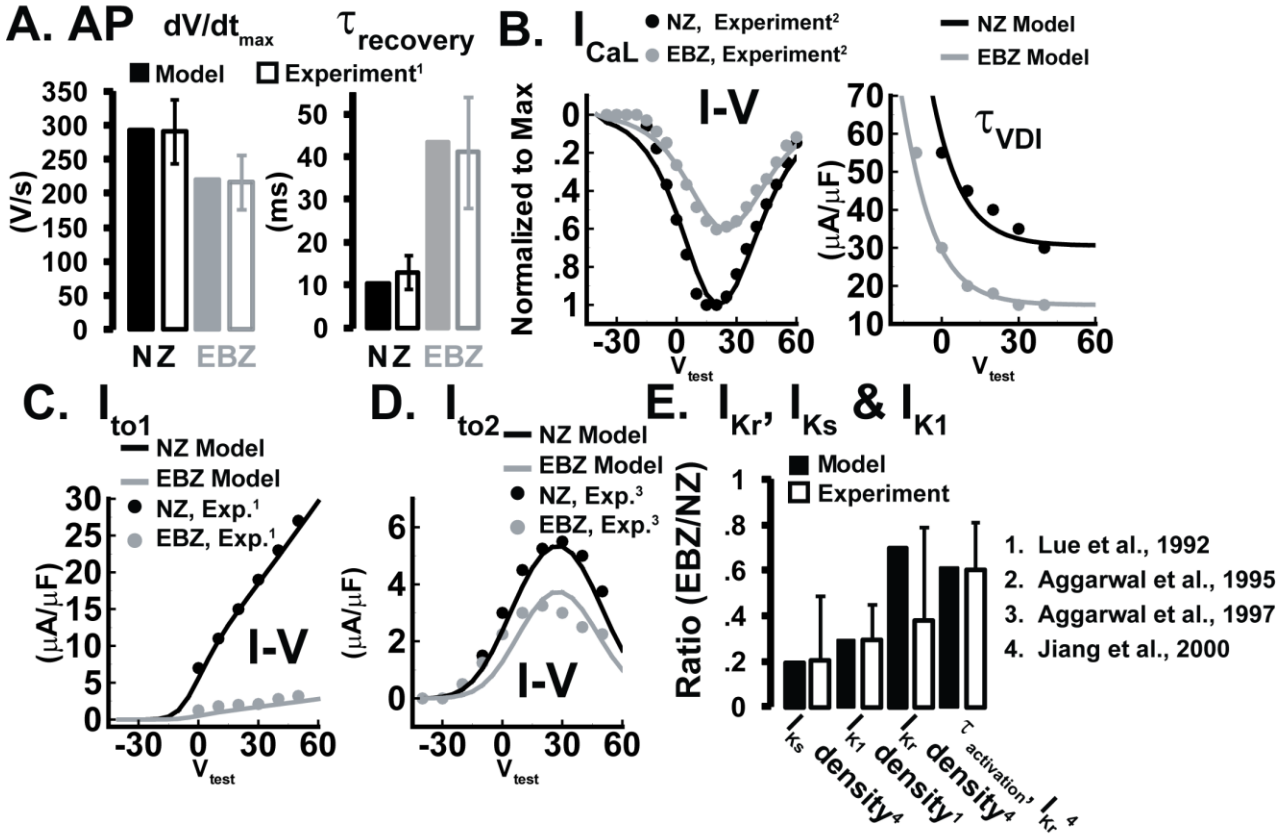

Figure 3-2 Model fits to NZ and EBZ Experimental Data. (**A)** Normal Zone (NZ) and (EBZ) maximum AP upstroke velocity (dV/dt_{max}) and time constant of recovery of AP dV/dt_{max} ($\tau_{recovery}$) in model and experiment (Lue and Boyden, 1992). $dVdt_{max}$ properties were determined as described in (Lue and Boyden, 1992). V_m was held at 0 mV for 500 ms, followed by varying time intervals at the holding potential (V_{hold}). APs were elicited by application of a stimulus after release of voltage clamp at V_{hold}. Fully recovered dV/dt_{max} was determined for an AP elicited after 500 ms at V_{hold} = -110 mV. $\tau_{recovery}$ was determined by an exponential fit to the time course of recovery of AP dV/dt_{max} at V_{hold} = -80 mV. **(B)** I_{CaL} current-voltage (I-V) relationship and time constant of voltage dependent inactivation (VDI) in model and experiment (Aggarwal and Boyden, 1995). NZ and EBZ I-V relationship of **(C)** I_{to1} (Lue and Boyden, 1992) and **(D)** I_{to2} (Aggarwal et al., 1997) in model and experiment. **(E)** Ratio (EBZ:NZ) of I_{Ks} density (Jiang et al., 2000), I_{K1} density (Lue and Boyden, 1992), I_{Kr} density (Jiang et al., 2000) and I_{Kr} (Jiang et al., 2000) time constant of activation in model and experiment.

Cl^- (Aggarwal et al., 1997) components of the transient outward current (I_{to1} and I_{to2}) in the EBZ, respectively. Delayed and inward rectifier potassium channel data are shown in Figure 3-2*E*. Reduced fast and slow components of the delayed rectifier potassium current (I_{Kr} and I_{Ks}) (Jiang et al., 2000), reduced inward rectifier current (I_{K1}) (Lue and Boyden, 1992) and more rapid I_{Kr} activation (Jiang et al., 2000) are reproduced by the EBZ model.

3.3.2 APD Rate Dependence in the Epicardial Border Zone

Figure 3-3*A* compares steady state APs (CL_{S1} = 1 s, $[K^+]_o$ = 4 mM) in NZ (black) and

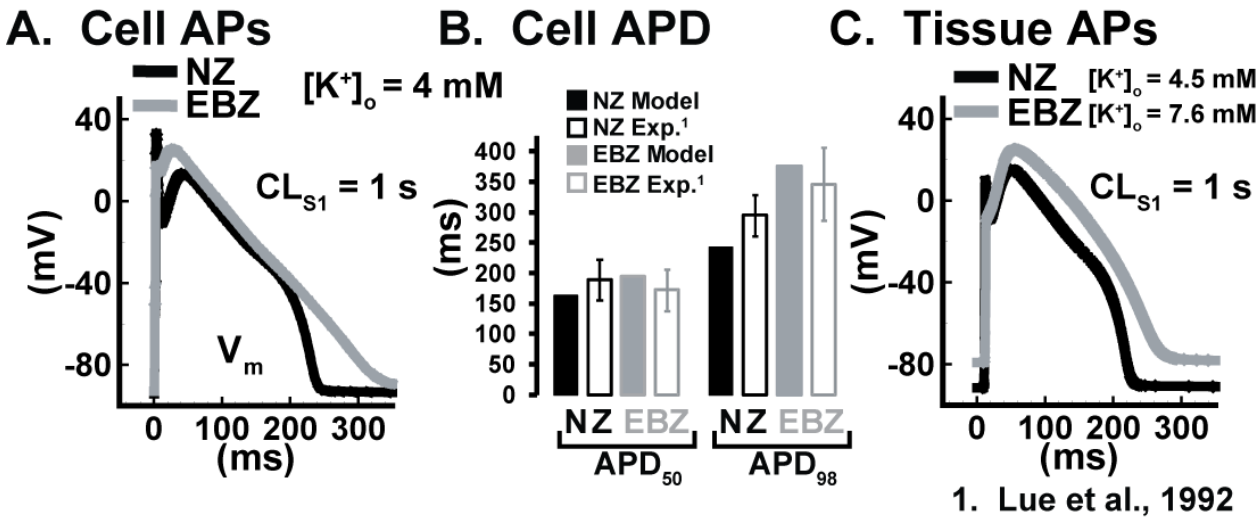

Figure 3-3 EBZ Action Potentials in Cell and Strand. *A.* Model NZ and EBZ cell APs (CL_{S1} = 1 s, $[K^+]_o$ = 4 mM). *B.* NZ and EBZ APD (CL_{S1} = 1 s, $[K^+]_o$ = 4 mM) at 50% and full (98%) repolarization in model and experiment (Janse and Wit, 1989; Lue and Boyden, 1992; Wit and Janse, 1992). *C.* Model NZ ($[K^+]_o$ = 4.5 mM) and EBZ ($[K^+]_o$ = 7.6 mM) APs (CL_{S1} = 1 s) for the central cell in homogeneous strand simulations.

EBZ (gray) single cell simulations. The EBZ model AP reproduces the absence of a phase 1 notch (due to loss of I_{to1}) and AP triangulation (due to reduction in I_{K1}) observed experimentally (Lue and Boyden, 1992). Both model and experiment show similar APD_{50} in NZ and EBZ (Fig. 3-3*B*, *left*). In addition, the model reproduces the significant prolongation of EBZ APD at full repolarization observed in cell experiments with $[K^+]_o$ = 4 mM (Fig. 3-3*B*, *right*). AP

triangulation, loss of the notch and prolonged EBZ cell APD at $[K^+]_o$ = 4 mM are consistent with previous single-cell modeling results (Cabo and Boyden, 2003; Hund et al., 2008a). Figure 3-3*C* compares simulated APs from the middle cell of homogeneous NZ and EBZ strands. Elevation of EBZ $[K^+]_o$ was required to reproduce the marked elevation of EBZ resting V_m observed in tissue experiments (Ursell et al., 1985) (model NZ $[K^+]_o$ = 4.5 mM, V_m = -91.5 mV; EBZ $[K^+]_o$ = 7.6 mM, V_m = -78.6 mV; experiment NZ V_m = -90 mV, EBZ V_m = -79 mV). The degree of elevation of $[K^+]_o$ required to reproduce the elevation of resting membrane potential (V_{rest}) observed experimentally is a critical determinant of EBZ repolarization and refractoriness. An EBZ strand paced at CL_{S1} = 1000 ms with $[K^+]_o$ = 4.5 mM has APD = 305 ms, PRR = 12 ms and ERP = 317 ms, while at elevated $[K^+]_o$ = 7.6 mM EBZ APD = 257 ms, PRR = 76 ms and ERP = 334 ms. Increasing $[K^+]_o$ substantially increases PRR due to the markedly slower recovery of EBZ dV/dt_{max} at elevated resting potentials (Fig. 3-2*A*, right). The elevation of EBZ $[K^+]_o$ thus leads to a net increase in ERP of 17 ms, with slowing of I_{Na} recovery due to resting V_m elevation causing an increase in PRR and offsetting ERP abbreviation due to APD shortening.

In order to understand ionic mechanisms underlying heterogeneity in the response of NZ and EBZ tissue to premature stimuli, APD restitution in NZ and EBZ strands was characterized. Figure 3-4 examines ionic mechanisms underlying altered refractoriness and restitution in the EBZ. Restitution in the EBZ is characterized by a CI_{S2} range with abnormally prolonged APD at short DI (Fig. 3-4*A*, *gray curve*). In the NZ, successful conduction occurs at a DI of 6 ms (Fig. 3-4*B left*), due to near complete recovery of I_{Na} availability (Fig. 3-4*C, left)*. In the EBZ successful conduction does not occur until DI = 77 ms (Fig. 3-4*B right*) due to slow recovery of I_{Na} from inactivation (Fig. 3-4*C right*). Weak I_{Na} and diminished upstroke V_m amplitude at DI = 77 ms are associated with abnormally prolonged EBZ APD. Peak V_m during the upstroke is

reduced to approximately –20 mV, resulting in slow I_{CaL} activation (Fig. 3-4*D, right*) and slow

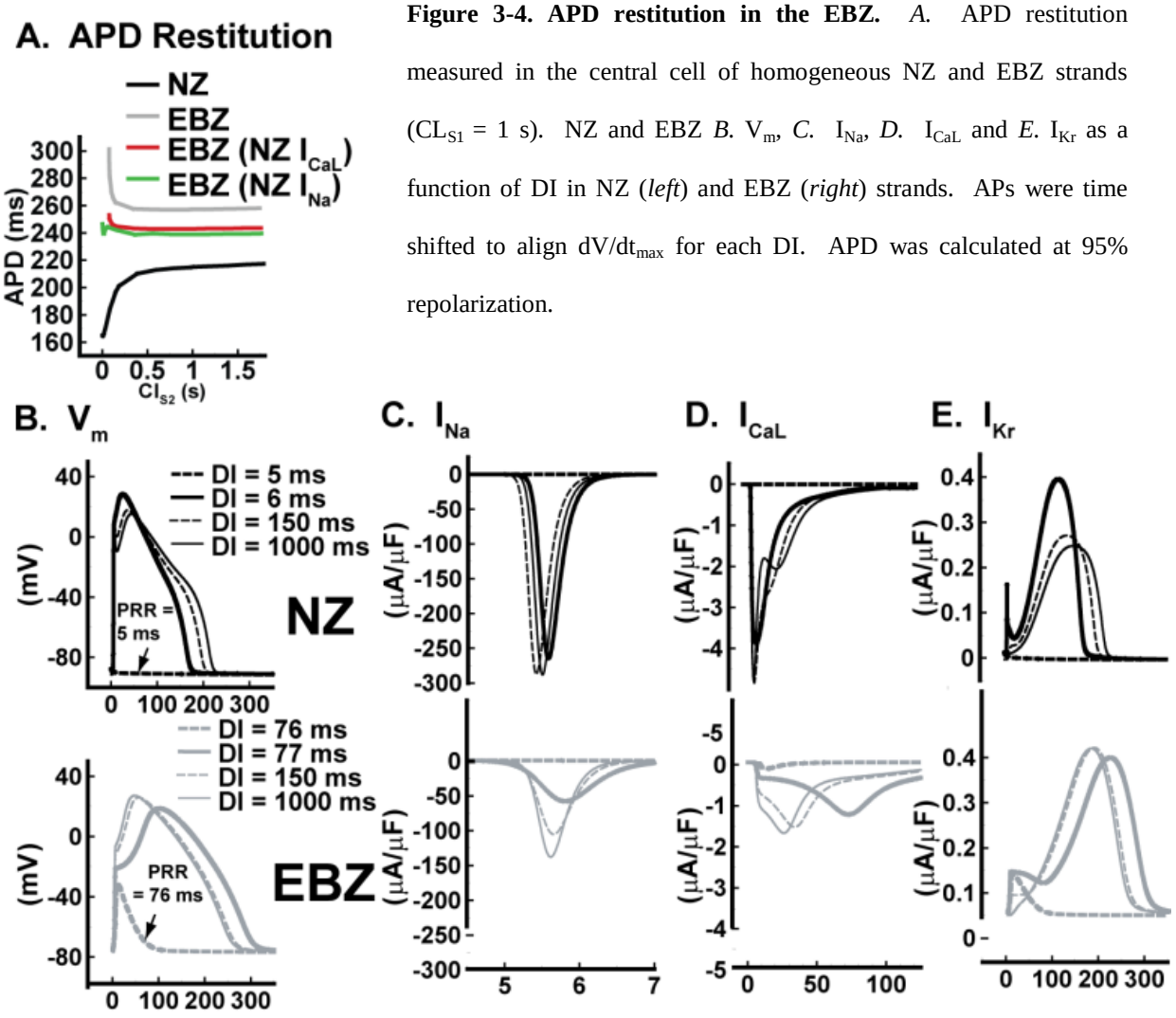

Figure 3-4. APD restitution in the EBZ. *A.* APD restitution measured in the central cell of homogeneous NZ and EBZ strands (CL_{S1} = 1 s). NZ and EBZ *B.* V_m, *C.* I_{Na}, *D.* I_{CaL} and *E.* I_{Kr} as a function of DI in NZ (*left*) and EBZ (*right*) strands. APs were time shifted to align dV/dt_{max} for each DI. APD was calculated at 95% repolarization.

I_{CaL} dependent depolarization (Fig. 3-4*B, right*). In the NZ, positive V_m promotes robust I_{CaL} activation at short DI (Fig. 3-4*D, left*), in contrast to the slow, weak activation of I_{CaL} observed in the EBZ. In addition, positive V_m leads to rapid I_{Kr} activation (Fig. 3-4*E, left*) and promotes short APD at short DI in the NZ. In contrast, suppression of EBZ I_{Kr} (Fig. 3-4*E, right*) due to negative V_m promotes APD lengthening at short DI. The critical role of slow I_{Na} recovery from inactivation and weak I_{CaL} activation in leading to abnormal EBZ restitution was confirmed via additional simulations. Restoration of normal I_{Na} or normal I_{CaL} dramatically reduces the region of prolonged APD at short DI in the EBZ strand (Fig. 3-4*A*).

3.3.3 Ionic Mechanisms of AP Heterogeneity and Conduction Block

We hypothesized that altered APD restitution in the EBZ leads to rate dependent dispersion of APD and conduction block in heterogeneous myocardium. Fig. 3-5A shows the

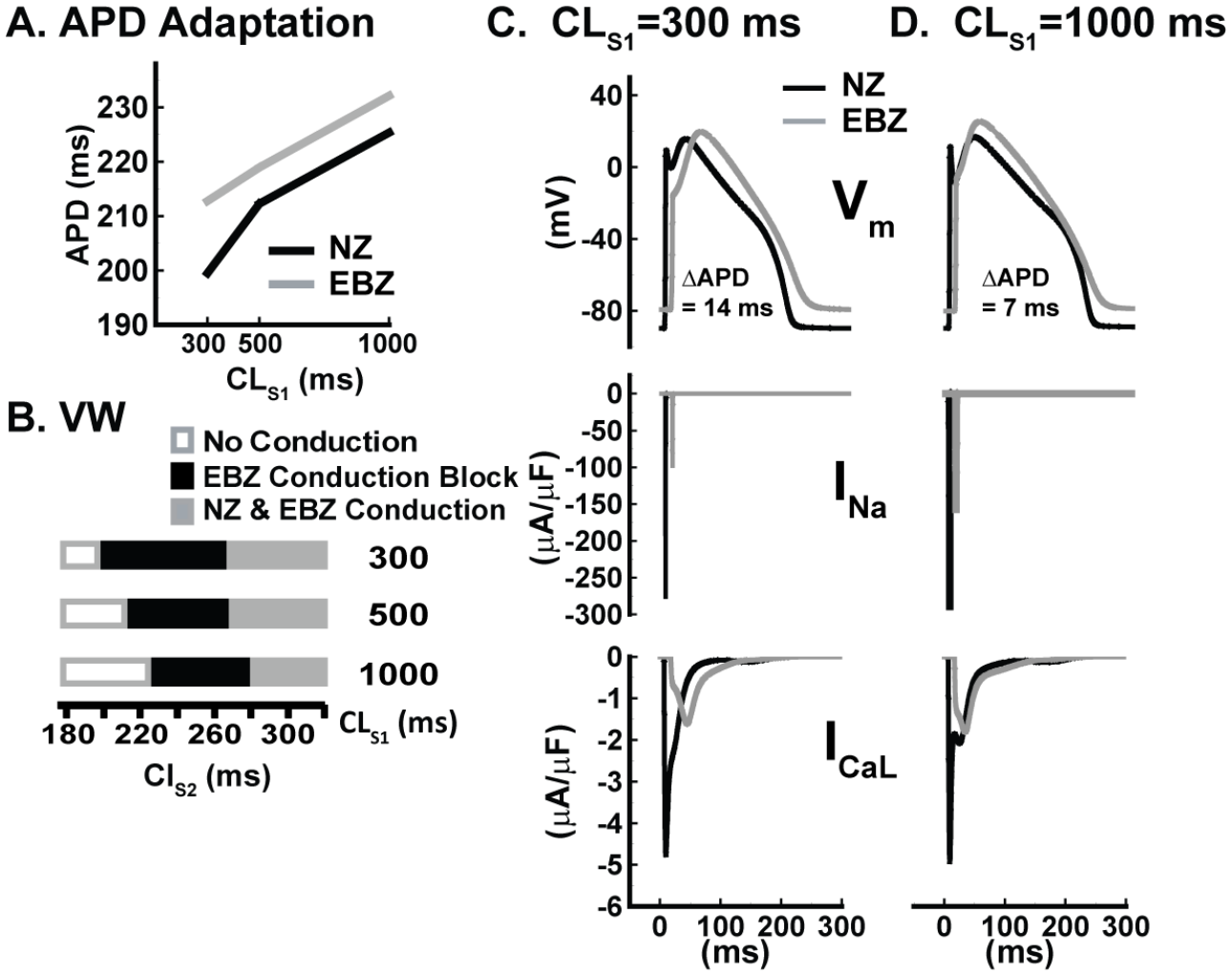

Figure 3-5 APD Adaptation and Block in heterogeneous strands. *A.* Rate dependence of NZ and EBZ APD in heterogeneous strand simulations. Strands were composed of 48 NZ and 48 EBZ cells, with stimulation at the NZ end. APD is shown for the central NZ (cell 24) and central EBZ (cell 72) cells. *B.* VW as a function of S2 coupling interval (CI_{S2}) for a range of CL_{S1}. V_m, I_{Na} and I_{CaL} from NZ (cell 24) and EBZ (cell 72) cells are shown at *C.* CL_{S1} = 300 and *D.* CL_{S1} = 1000 ms. APD was calculated at 95% repolarization.

rate dependence of APD in a heterogeneous strand simulation. The strand was composed of 48 EBZ (cell 72) cells. APD heterogeneity between NZ and EBZ increases at CL_{S1} = 300 ms. The

VW in heterogeneous strand simulations was characterized via S1-S2 stimulation protocols to test the hypothesis that heterogeneity in APD and refractoriness would lead to a large, rate-dependent VW. Fig. 3-5B shows the VW in a heterogeneous strand in response to S2 stimuli as a function of CL_{S1}. The width of the VW was 70 ms at CL_{S1} = 300 ms, 56 ms at CL_{S2} = 500 and 55 ms at CL_{S1} = 1000 ms. The width of the VW at all CL_{S1} is much greater than the APD dispersion, demonstrating that post-repolarization refractoriness is the primary determinant of the width of the VW. However, increased APD dispersion at CL_{S1} = 300 ms does lead to an increase in the VW relative to that at slower rates. Figs. 3-5*C-D* explore the ionic mechanism of increased APD dispersion at CL_{S1} = 300 ms. Conduction at CL_{S1} = 300 ms is characterized by reduced I_{Na} activation (Fig. 3-5*C, middle),* a weakened AP upstroke (Fig. 3-5*C, top)*, delayed I_{CaL} activation (Fig. 3-5*C, bottom*) and prolonged APD relative to the NZ (Fig. 3-5*C, top)*. At CL_{S1} = 1000 ms I_{Na} is more fully recovered (Fig. 3-5*D, middle),* I_{CaL} activation is less delayed (Fig. 3-5*D, bottom),* and APD heterogeneity between NZ and EBZ is decreased (Fig. 3-5*D, top)*.

The effects of heterogeneity in NZ and EBZ APD and refractoriness were also explored during sustained pacing at the rapid S1 pacing rates that characterize tachycardia and are often required to induce arrhythmia experimentally. Fig. 3-6*A* characterizes the VW in a heterogeneous strand for $CL_{S1} < 300$ ms. Pacing over a CL_{S1} range from 190 to 270 ms results in 2:1 block at the transition from NZ to EBZ, while pacing at CL_{S1} = 280 ms results in 4:3 block at the NZ to EBZ transition. In order to explore the ionic mechanisms underlying this large VW and abnormal block patterns, Figure 3-6*B-D* shows V_m, I_{Na} and and I_{CaL} from the central NZ cell (cell 24) and central EBZ cell (cell 72) at CL_{S1} = 280, 250 and 200 ms respectively. At CL_{S1} = 280 ms, 4:3 block at the NZ to EBZ transition occurs (Fig. 3-6*B*). Block is preceded by a series of 3 successful EBZ APs in which APD progressively increases (212 to 217 to 242 ms) and DI

shortens (68 to 63 to 38 ms) until the EBZ ERP is exceeded and block occurs. Increasing APD is

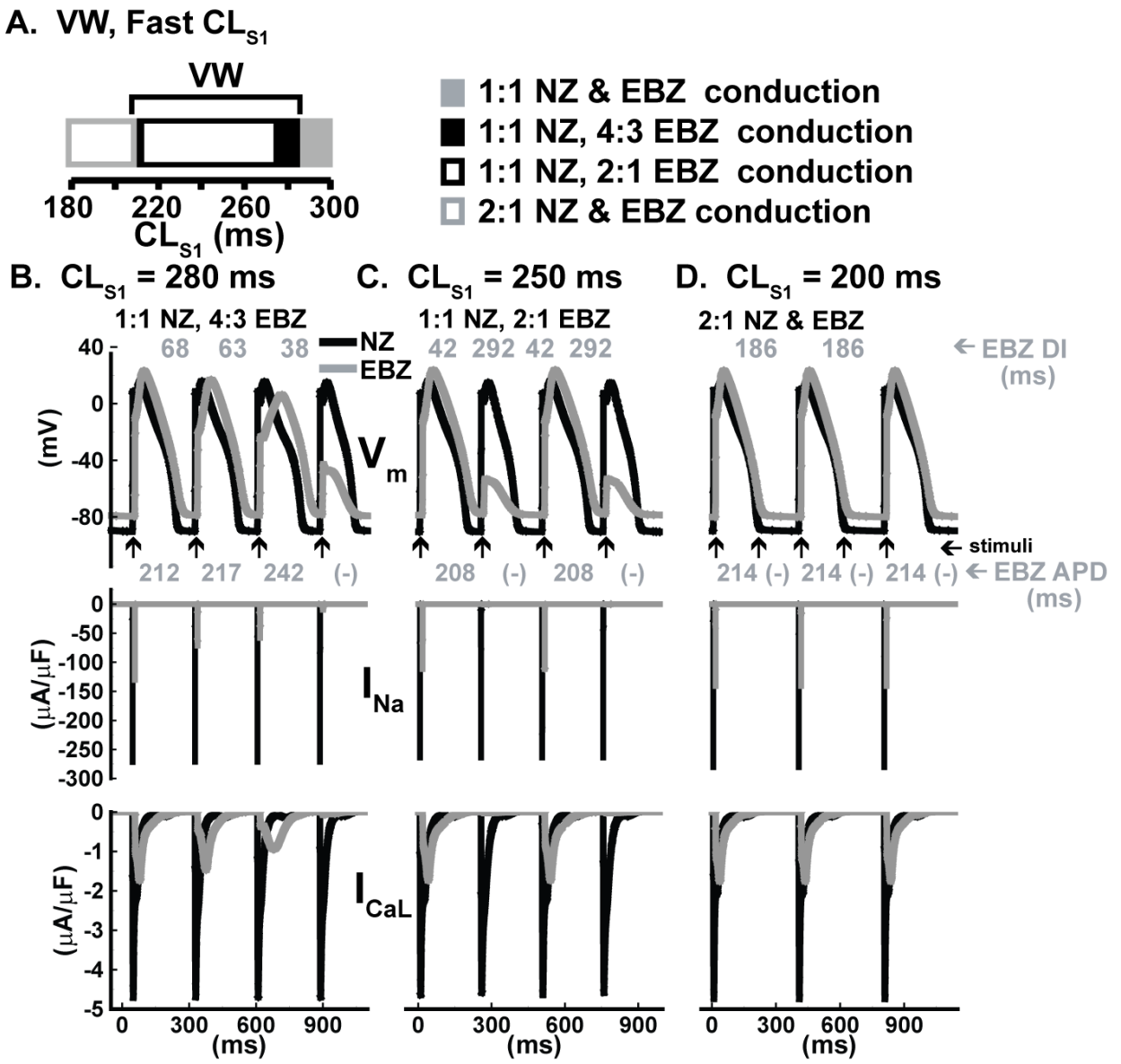

Figure 3-6 Conduction Block at fast CL_{S1} in heterogeneous strand. *A.* VW in heterogeneous strands during pacing at fast CL_{S1}. Strands were composed of 48 NZ and 48 EBZ cells. Stimuli were applied at the NZ end. *B-D.* NZ (cell 24) and EBZ (cell 72) V_m, I_{Na} and I_{CaL} in heterogeneous strands during pacing at fast CL_{S1} illustrating representative patterns of conduction and block; *B.* 4:3 EBZ conduction block (CL_{S1} = 280 ms). *C.* 2:1 EBZ conduction block (CL_{S1} = 250 ms). *D.* 2:1 NZ and EBZ conduction block (CL_{S1} = 200 ms). APD was calculated at 95% repolarization.

accompanied by decreasing I_{Na} activation (Fig. 3-6*B*, middle) and increasingly slow and delayed activation of I_{CaL} (Fig. 3-6*B*, bottom). The abnormal increase in APD with decreasing DI during APD restitution is therefore responsible for the region of 4:3 block. At CL_{S1} = 250 ms, 2:1 block at the NZ to EBZ transition occurs (Fig. 3-6*C*) since the ERP in the EBZ exceeds the pacing CL. At CL_{S1} = 200 ms, (Fig. 3-6*D*) the pacing rate exceeds the ERP of both the NZ and EBZ and 2:1 block occurs across the entire strand.

3.3.4 Ionic Mechanisms of Conduction Post-Infarction

We hypothesized that remodeling of key determinants of conduction velocity and safety,

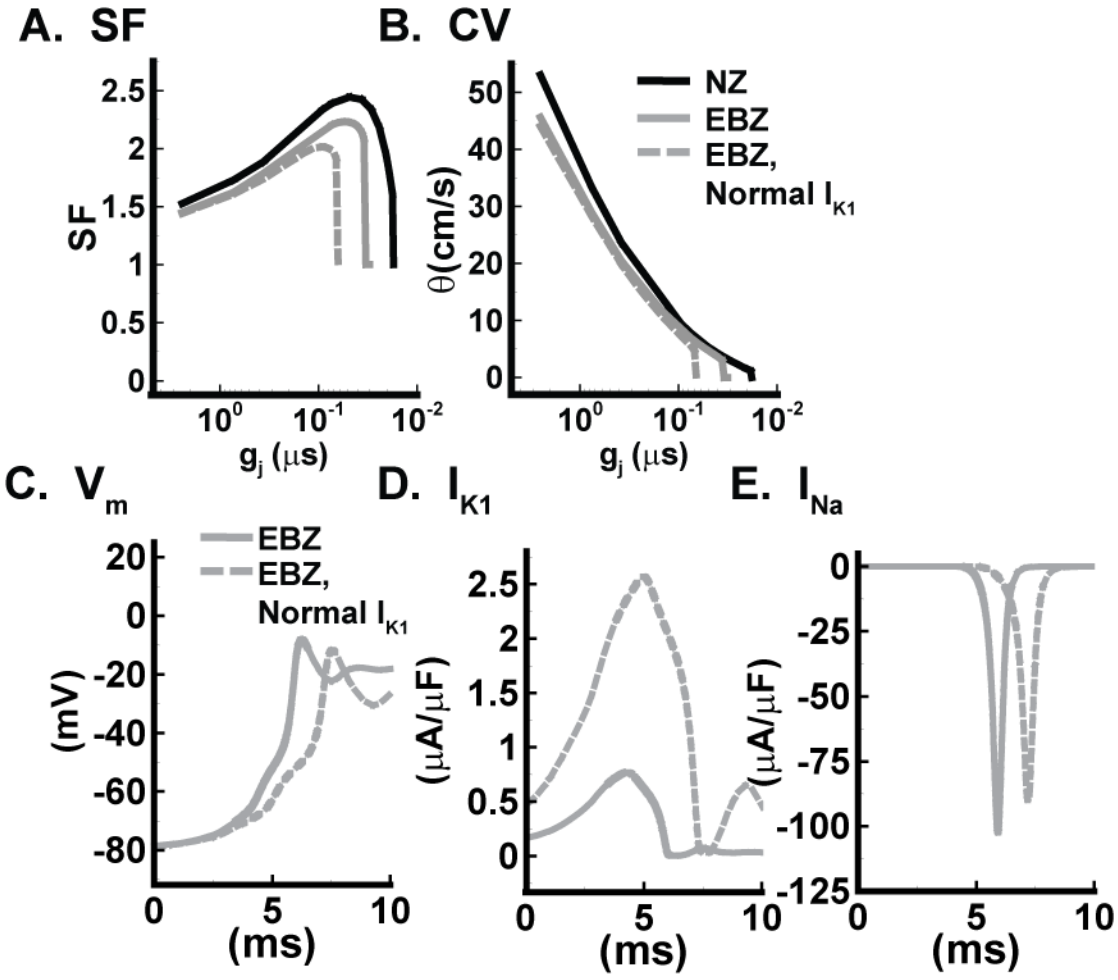

Figure 3-7 Role of I_{Na} and I_{K1} in EBZ conduction. *A.* Safety factor and *B.* conduction velocity as a function of gap junction conductance (g_j) in homogeneous strands of NZ cells, EBZ cells and EBZ cells with normal I_{K1}

restored. *C.* V_m, *D.* I_{K1} and *E.* I_{Na} for propagating APs in EBZ strands with remodeled and normal I_{K1} (greatly reduced gap junction coupling, g_j = 0.069 μS).

including gap junction conductance, I_{Na}, I_{CaL} and I_{to1}, would lead to abnormal conduction in the EBZ. NZ and EBZ conduction safety and velocity as a function of gap junction conductance (g_j) are compared in Figures 3-7*A* and 3-7*B*. Despite the range of remodeling processes that occur in the EBZ, conduction safety and velocity remain near normal except at the most severe degrees of gap junction uncoupling. The ionic mechanisms promoting near-normal conduction in the EBZ were unclear, however, considering the key role of I_{Na} in (Shaw and Rudy, 1997) conduction and the severe remodeling of this current in the EBZ. It was therefore hypothesized that additional remodeling processes in the EBZ counteract the effect of reduced I_{Na} and help maintain near normal conduction. Additional simulations revealed a key role for I_{K1} remodeling in maintaining near normal conduction in the EBZ. When EBZ I_{K1} is restored to the larger magnitude that occurs in the NZ, SF is more severely reduced (Fig. 3-7*A*) and conduction block occurs at a lesser degree of uncoupling (Fig. 3-7*B*). Figures 3-7*C-E* compare propagating APs, I_{K1} and I_{Na} in uncoupled EBZ strands (g_j = 0.069 □= 0.069 pled EBZ stra$_{K1}$ restored to its normal density. Reduction of I_{K1} (Fig. 3-7*D*) in the EBZ increases cell excitability, leading to a faster AP upstroke (Fig. 3-7*C*), increased I_{Na} activation (Fig. 3-7*E*) and thus increased SF.

Experiments and simulations have emphasized the importance of I_{to1} (Huelsing et al., 2001) and I_{CaL} (Joyner et al., 1996; Rohr and Kucera, 1997; Shaw and Rudy, 1997) as determinants of conduction safety in the context of gap junction uncoupling. It was therefore hypothesized that remodeling of EBZ I_{to1} and I_{CaL} would have a significant effect on conduction in the EBZ. Simulations using the NZ strand model are consistent with the expected role of I_{CaL} and I_{to1} in conduction (Fig. 3-8*A*, *left*). In uncoupled tissue, block of I_{CaL} reduces NZ SF while block of I_{to1} facilitates NZ conduction and increases SF (Fig. 3-8*A*, *left*). In contrast, EBZ strand

simulations show that block of I_{CaL} and restoration of normal I_{to1} both have a negligible effect on

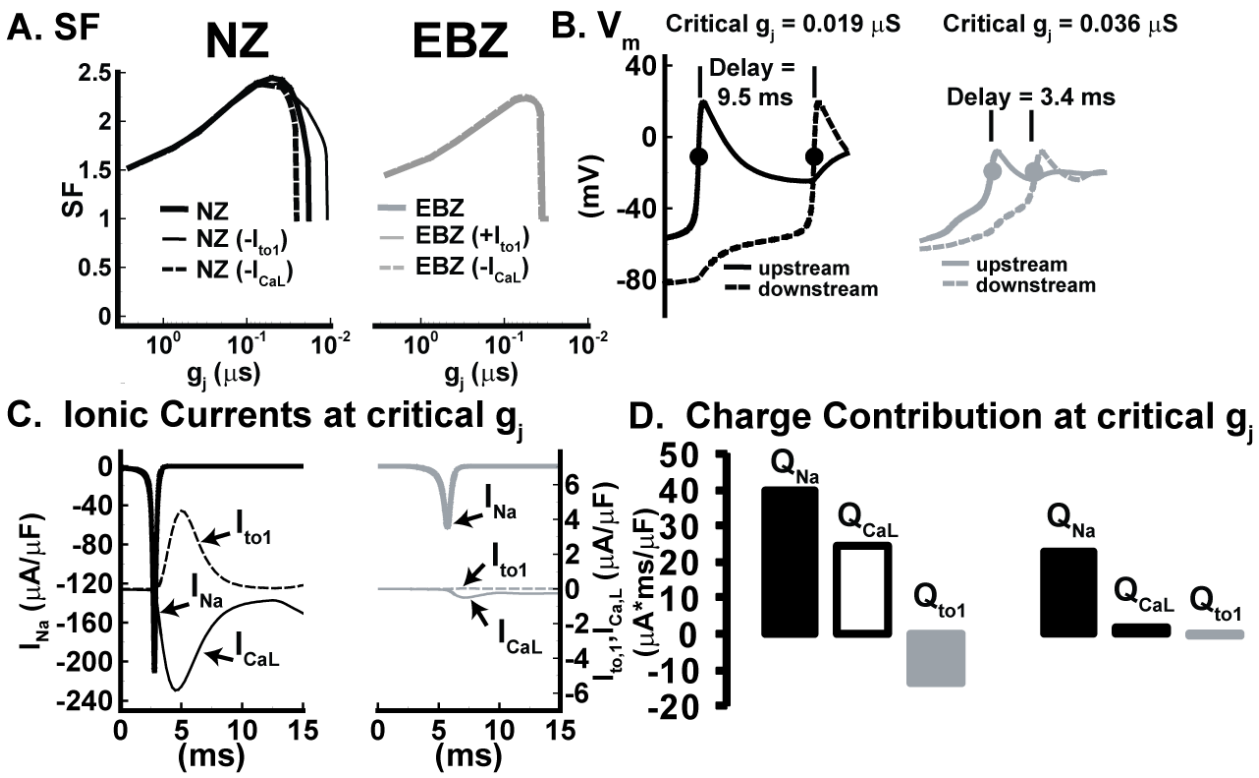

Fig. 3-8 Role of I_{CaL} and I_{to1} in NZ and EBZ conduction. *A.* Safety factor for propagation as a function of gap junction coupling in homogeneous NZ (*left*) and EBZ (*right*) strands. *B.* V_m of upstream and downstream cells during propagation in homogeneous NZ (*left*) and EBZ (*right*) strands at the minimum gap junction conductance (critical g_j) for which propagation occurs. *C.* Activation of I_{Na}, I_{to1} and I_{CaL} for a propagating AP at the critical g_j in homogeneous NZ (*left*) and EBZ (*right*) strands. Normal I_{to1} was included in the EBZ strand simulation to assess its potential role in propagation. *D.* Charge contribution (Q) of I_{Na}, I_{CaL} and I_{to1} to propagation at the critical g_j in NZ (*left*) and EBZ strands with normal I_{to1} restored (*right*).

conduction safety (Fig. 3-8*A*, *right*). Figure 3-8*B-D* investigate the role of I_{to1} and I_{CaL} in conduction in NZ and EBZ strands, at the smallest gap junction conductance for which conduction occurs (NZ critical g_j = 0.019 μS, EBZ critical g_j = 0.036 μS). Simulations are

shown with normal I_{to1} restored in the EBZ, to determine the potential importance of this current in propagation. In the NZ strand, robust I_{Na} leads to a strong AP upstroke (maximum upstroke V_m = +18 mV) and a long delay (9.5 ms) between the excitation of the neighboring upstream and downstream cells (Fig. 3-8*B, left)*. During this delay, I_{CaL} and I_{to1} activation are both large (Fig. 3-8*C, left*). Integration of I_{Na}, I_{CaL} and I_{to1} during the delay between activation of adjacent cells was used to characterize their relative contribution of excitatory charge (Q) during propagation (Fig. 3-8*D, left*). In the NZ, I_{CaL} contributes excitatory charge on the order of that contributed by I_{Na}. Since I_{to1} is a repolarizing current it makes a negative contribution to excitation. In the NZ, this negative contribution is comparable to the positive contributions made by I_{Na} and I_{CaL}. In the EBZ, the reduction in I_{Na} due to decreased density and slowed recovery from inactivation leads to a very weak AP upstroke (maximum upstroke V_m = -13 mV) (Fig. 3-8*B, right*). Intercellular conduction delay (3.4 ms) at the larger critical EBZ g_j is much shorter than in the NZ (Fig. 3-8*C*). The decreased AP upstroke V_m leads to much weaker activation of I_{CaL} and I_{to1} (restored to NZ density) in the EBZ (Fig. 3-8*C, right*), and the shorter intercellular delay limits the time period within which these currents can contribute charge to propagation. The charge contributions of I_{CaL} and I_{to1} to EBZ conduction are consequently negligible relative to the contribution of I_{Na} (Fig. 3-8*D, right*).

3.3.5 Anti-arrhythmic Effects of SkM1-I_{Na} Post-Infarction

A recent study has shown that injection of the skeletal sodium channel SkM1-I_{Na} into the EBZ decreases the inducibility of sustained tachycardia and fibrillation (Lau et al., 2009). Strand simulations were used to seek insight into the ionic mechanism underlying the anti-arrhythmic action of SkM1-I_{Na}. SkM1-I_{Na} was modeled via a 6 mV rightward shift in steady state availability relative to NZ I_{Na} (Fig. 3-9*A*) and the density of injected EBZ SkM1-I_{Na} was adjusted

to reproduce the 80% increase in EBZ dV/dt_{max} recorded in experiments (Lau et al., 2009). In homogeneous strand simulations, the increase in APD at short DI observed during EBZ restitution is attenuated (Fig. 3-9*B)*, and PRR is dramatically reduced (EBZ PRR = 76 ms,

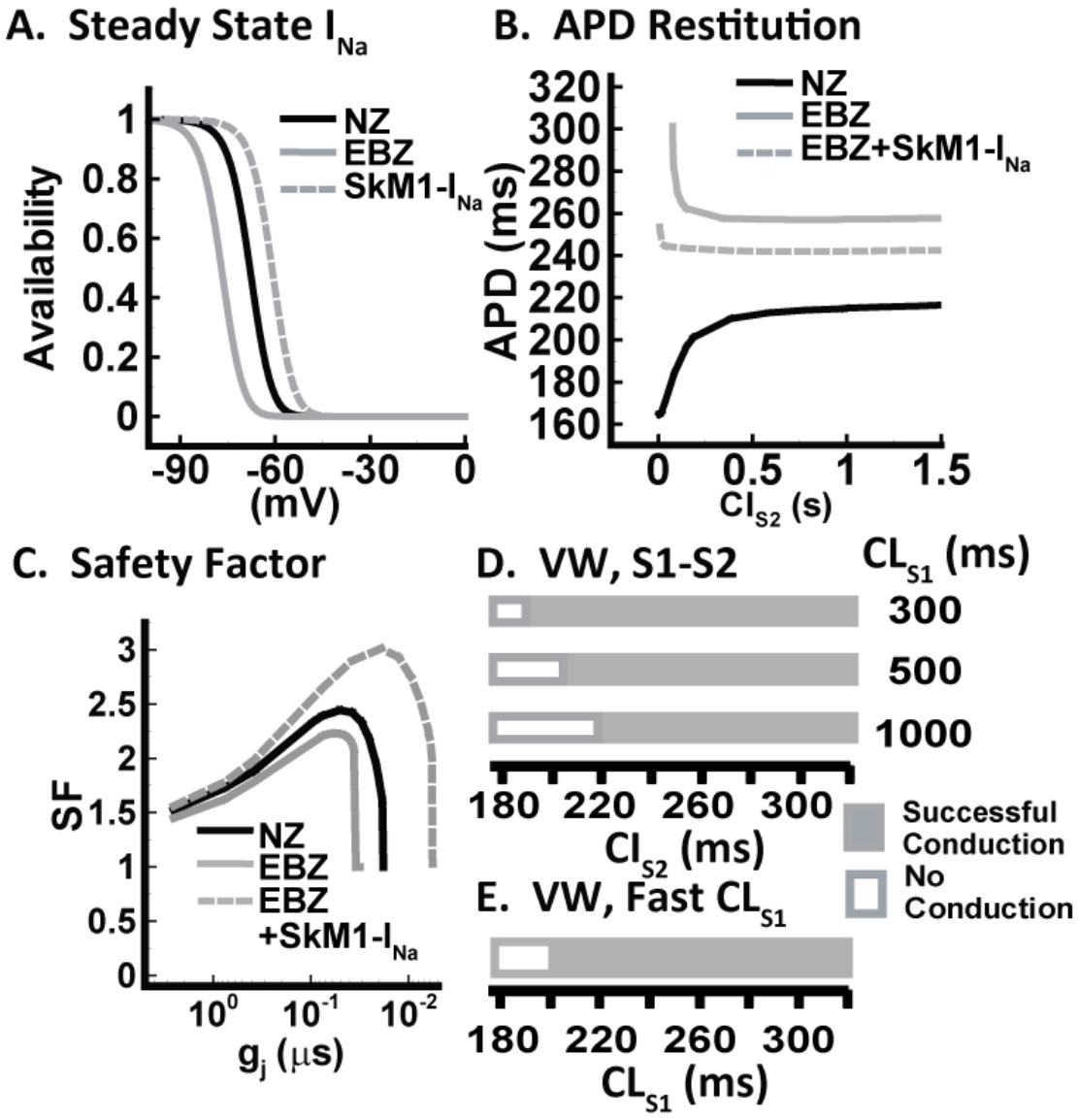

Fig. 3-9 Anti-arrhythmic effects of SkM1 I_{Na}. *A.* Safety factor for propagation as a function of gap junction coupling in homogeneous NZ (*left*) and EBZ (*right*) strands. *B.* V_m of upstream and downstream cells during propagation in homogeneous NZ (*left*) and EBZ (*right*) strands at the minimum gap junction conductance (critical g_j) for which propagation occurs. *C.* Activation of I_{Na}, I_{to1} and I_{CaL} for a propagating AP at the critical g_j in homogeneous NZ (*left*) and EBZ (*right*) strands. Normal I_{to1} was included in the EBZ strand simulation to assess its

potential role in propagation. *D.* Charge contribution (Q) of I_{Na}, I_{CaL} and I_{to1} to propagation at the critical g_j in NZ (*left*) and EBZ strands with normal I_{to1} restored (*right*).

EBZ+SkM1-I_{Na} PRR = 2 ms). Figure 3-9*C* demonstrates that the addition of SkM1-I_{Na} dramatically increases the SF for conduction in the EBZ, especially in regions of severe uncoupling. In order to explore the potential effect of SkM1-I_{Na} on arrhythmia inducibility, the VW in heterogeneous strands with SkM1-I_{Na} added to the EBZ region was assessed. The dramatic reduction in ERP in the SkM1-I_{Na} treated EBZ region completely eliminates the VW for premature S2 stimuli at all CL_{S1} (Fig. 3-9*D*, compare to Fig. 5*B).* During pacing at fast CL_{S1} (without S2 stimulation), the VW is also completely eliminated after addition of SkM1-I_{Na} (Fig. 3-9*E*,, compare to Fig. 6*A*). These results suggest that elimination of abnormal EBZ refractoriness and restitution are critical determinants of the anti-arrhythmic action of SkM1-I_{Na}.

3.4 Discussion

An extensively studied experimental canine model of the 3-5 day old infarct has provided critical insights into the nature of the arrhythmias that originate in the EBZ. Additional studies have characterized the ionic remodeling processes that accompany these arrhythmias. The mechanistic link between EBZ remodeling and increased susceptibility to arrhythmia remains incompletely understood, however. The present work yields several novel mechanistic insights into ionic mechanisms of arrhythmia after infarction. 1) EBZ tissue exhibits abnormal APD restitution, with a region of increasing APD at short DI. At short DI slow recovery of I_{Na} severely weakens the AP upstroke, causing abnormally slow and delayed I_{CaL} activation and suppression of I_{Kr} activation, prolonging APD. 2) Prolonged refractoriness is the primary cause of the large VW in response to premature S2 stimuli. Abnormal EBZ restitution also promotes APD dispersion between NZ and EBZ at fast CL_{S1} and increases the VW in response to S2 stimuli. 3) Prolonged refractoriness in the EBZ also promotes a large VW during pacing at

sufficiently fast pacing rates (CL_{S1} < 300 ms). Abnormal APD restitution increases the width of the VW by promoting 4:3 EBZ conduction block. 4) Despite severely reduced I_{Na}, EBZ safety factor for conduction and conduction velocity are near normal, even in severely uncoupled tissue. The detrimental effect of reduced I_{Na} on conduction is partially offset by the reduction in EBZ I_{K1}, which facilitates conduction. 5) Although I_{CaL} and I_{to1} play a role in conduction in the NZ, remodeling of these currents does not significantly affect SF in the EBZ. Reduced EBZ I_{Na} decreases upstroke V_m during propagation, suppressing I_{CaL} and I_{to1} activation and precluding any role for these currents in conduction safety. 6) The anti-arrhythmic effects of SkM1-I_{Na} injection are likely attributable to a range of desirable actions including; a. Elimination of abnormal APD restitution. b. Shortening of EBZ ERP and c. increased safety factor for conduction in uncoupled tissue. Elimination of abnormal restitution and shortening of ERP in the EBZ by SkM1-I_{Na} addition eliminates the VW in heterogeneous strand simulations.

Previous computational studies have provided important insights into the ionic determinants of EBZ ERP and repolarization (Cabo and Boyden, 2003), the role of heterogeneous gap junction coupling in stabilizing reentrant circuits (Cabo and Boyden, 2006), and the role of elevated CaMKII in increased ERP and susceptibility to conduction block in the EBZ (Christensen et al., 2009; Hund et al., 2008a). The present work compliments these previously published studies in several ways. APD restitution is thought to be a critical determinant of reentry initiation and maintenance, but has not been explored in detail in previous EBZ modeling studies. Slow conduction and localized gap junction uncoupling are thought to be important in arrhythmogenesis post-infarction, but the contribution of the range of EBZ remodeling processes to conduction in this setting has not been explored. Previous simulations studies have emphasized the importance of I_{Na} remodeling in ERP prolongation (Cabo and

Boyden, 2003; Christensen et al., 2009), slowed conduction (Cabo and Boyden 2003; Christensen, Dun et al. 2009) and formation of the VW (Christensen, Dun et al. 2009). The present study demonstrates that remodeling of I_{Na} has several additional important consequences, including reduction in SF, alteration of the role of I_{to1} and I_{CaL} in conduction and alteration of restitution kinetics.

The present study demonstrates that abnormal EBZ restitution promotes dispersion of refractoriness and increases the VW. The period of increasing APD at short DI in the EBZ is caused by slow I_{Na} recovery (due to I_{Na} remodeling and elevated V_{rest}) and decreased I_{CaL} density. EBZ APs where a weak upstroke (V_m ~ -15 mV) results in slow and delayed I_{CaL} activation and AP prolongation are analogous to those observed in epicardium in response to I_{Na} block (Krishnan and Antzelevitch, 1991) or increased I_{to1} (Calloe et al., 2010). The present study suggests that a sufficiently negative peak AP upstroke can lead to delayed I_{CaL} activation and AP prolongation, even in the absence of large I_{to1}.

The ionic mechanisms of APD restitution and the response to rapid pacing have not been studied in detail in previous EBZ experimental and modeling studies. Heterogeneity in the response of NZ and EBZ tissue at fast CL_{S1} and short DI is no doubt critical to the initiation and maintenance of reentry, and is an important area of further experimental and modeling studies. Resting membrane potential (Ursell et al., 1985), I_{Na} remodeling (Baba et al., 2005) and I_{CaL} remodeling (Baba et al., 2005) vary regionally, and this spatial variation may be an additional determinant of APD dispersion and arrhythmogenesis through effects on EBZ APD and ERP at fast CL_{S1}.

The healing infarct is characterized by compromised I_{Na} (Pu and Boyden, 1997), localized gap junction uncoupling (Cabo et al., 2006; Yao et al., 2003) and depolarized resting

membrane potential (Ursell et al., 1985). The inducibility of sustained reentry will depend on the safety and velocity of conduction in the context of this remodeling. It is well established that reduced I_{Na} slows conduction and decreases conduction safety. I_{to1} (Huelsing et al., 2001) and I_{CaL} (Joyner et al., 1996; Rohr and Kucera, 1997; Shaw and Rudy, 1997) have also been accorded a role in conduction safety in uncoupled tissue. The present study demonstrates that I_{CaL} facilitates and I_{to1} inhibits conduction in poorly coupled NZ strands, but remodeling of these currents has no effect on conduction in the EBZ. Participation of I_{CaL} and I_{to1} in conduction requires; 1) prominent I_{Na}, so that a robust AP upstroke strongly activates I_{CaL} and I_{to1} and 2) highly uncoupled gap junctions, so that long intercellular delays allow time for I_{CaL} and I_{to1} to make large charge contributions during propagation. The model suggests that conduction in pathophysiological conditions in which I_{Na} is compromised, such as the healing infarct, will not be directly affected by I_{CaL} and I_{to1} expression. This result also suggests that cell pair experiments (Huelsing et al., 2001; Joyner et al., 1996), in which direct stimulation leads to a more robust AP upstroke than that observed during multi-cellular propagation, are likely to overestimate the role of these currents in propagation. In addition, the anti-arrhythmic effects of enhanced I_{CaL} on the healing infarct (Pu et al., 1999) are likely attributable to effects other than direct facilitation of conduction by I_{CaL}. Our simulation results do, however, find that I_{K1} reduction in the EBZ increases conduction safety and allows conduction at more severe degrees of gap junction uncoupling than would otherwise be possible.

The reduction in inducibility of tachycardia and fibrillation by SkM1-I_{Na} injection post-infarction reported experimentally (Lau et al., 2009) suggests an exciting new anti-arrhythmic approach. The authors attribute this anti-arrhythmic effect of SkM1-I_{Na} to promotion of propagation at normal conduction velocity in depolarized tissue. Our simulations suggest several

desirable effects of SkM1-I_{Na} in the EBZ. In regions of normal gap junction coupling, EBZ conduction safety and velocity are near normal, despite reduced I_{Na} and increased V_{rest}. SkM1-I_{Na} is likely to play its most important role in regions of uncoupled tissue, where its effects on conduction safety and velocity are most pronounced. In addition, the simulations suggest that SkM1-I_{Na} normalizes EBZ APD restitution and refractoriness and eliminates the VW. Potentially undesirable side effects, such as $[Na^+]_i$ overload, were not observed. Taken together, these results suggest that SkM1-I_{Na} treatment of EBZ tissue is a promising anti-arrhythmic approach.

Chapter 4. Conclusions, Limitations and Future Directions

APD restitution, accommodation and adaptation have been observed in a range of species and cell types, and are thought to play an important role in arrhythmogenesis. The control epicardial myocyte presented in Chapter 2 accurately reproduces a wider range of these rate dependent phenomena then previously published models, and the accompanying simulations provide important insight into their underlying ionic mechanisms. This model is a valuable control model for the study of the effects of the ion channel remodeling that occurs in a wide range of disease states, as demonstrated in Chapter 3. Future studies could study the effects of alterations in ion channels shown to play an important role in restitution, accommodation and adaptation including I_{CaL}, I_{Ks} and I_{to1} on the stability of reentry, and compare these results against the predictions made in multi-dimensional simulations using simplified ionic models.

Additional simulations and refinements to the model should focus on increasing the physiological accuracy of the model response to block of the major ionic currents. Additional work in collaboration with Jordi Heijman has shown that the availability of ICaL at negative voltages is an important determinant of the response of the model to ion channel block, and these results should be incorporated into future studies using the model. Cell signaling pathways, especially the adrenergic and CaMKII pathways, are important determinants of cardiac cell electrophysiology and it is important that they be incorporated into future studies using the model. Future work by Jordi Heijman, building on the work of Hund and coworkers, is likely to provide important insight into the role of these signaling pathways in cardiac electrophysiology. APD alternans due to intracellular Ca2+ dynamics are also important determinants of cardiac electrophysiology and health and disease, and should be further studied in the model. Dr. Leonid

Livshitz has provided an important contribution to the ionic mechanisms of Ca2+ dependent alternans in a previous version of the Hund-Rudy canine model.

Although the present work provides several novel mechanistic insights into ionic mechanisms of remodeling and arrhythmogenesis post-infarction, the EBZ is a complex substrate where many additional factors may promote initiation and maintenance of arrhythmia. Our study examines vulnerability to and underlying mechanisms of formation of the initial line of block, a necessary prerequisite for initiation of reentry. Studies of reentry dynamics will require simulations in two or three-dimensional models of the EBZ. Tissue anisotropy may contribute to the formation of lines of block and lines of apparent block during reentry (Dillon et al., 1988) in the EBZ and requires a detailed description of cell orientation (Spach et al., 2000) and gap junction distribution (Peters et al., 1997; Yao et al., 2003) for accurate modeling. The variable thickness of the EBZ (Peters et al., 1997) may also contribute to the formation of stable reentrant circuits, a phenomenon best studied in three-dimensional models of the EBZ. Arrhythmogenesis in the EBZ may also depend on spatial heterogeneity of remodeling (Baba et al., 2005; Cabo and Boyden, 2006; Cabo et al., 2006). A recent modeling study has shown that increased levels of oxidized CaMKII (Christensen et al., 2009) may contribute to slowed conduction and prolonged ERP in the EBZ through effects of CaMKII on the steady state availability of I_{Na} (Wagner et al., 2006). The arrhythmogenic effects of I_{Na} remodeling characterized here may depend on CaMKII hyperactivity and oxidation state, although this dependence is not explicitly included in the present model. The role of CaMKII in the EBZ is an important subject for future experimental and modeling studies and will depend on regulation of CaMKII activation by intracellular Ca^{2+} and oxidation state, and the effect of CaMKII activation level on Ca^{2+} handling proteins (Maier, 2009), Na^{+} (Wagner et al., 2006), Ca^{2+} and K^{+} currents (Wagner et al., 2009).

Appendix A. Control Epicardial Cell Formulation

The equations below are for the original control model (Decker et al., 2009). Note that I_{Na} and I_{CaL} formulations were modified and a new model of I_{NaL} was used to construct the NZ and BZ models (See Appendix B).

Propagation in a Strand

A detailed description of computational methods for strand simulations is included in previous work from our laboratory (23). Briefly, propagation in a strand of serially connected HRd model cells was simulated via a finite difference approximation of the cable equation.

$$\frac{1}{C_M}\left(\frac{(V_{t-1}^t - V_i^t) - (V_i^t - V_{t+1}^t)}{\Delta x^2}\right)\frac{a}{2R_i} = R_{CG}\left(\left(\frac{V_i^{t+1} - V_i^t}{\Delta t}\right) + \frac{\bar{I}_{ion}}{C_M}\right)$$

V_i^t	membrane potential in cell i at time t
R_{CG}	ratio between capacitative and geometric areas, 2
a	fiber radius, 11 μM
C_m	specific membrance capacitance, 1 $\mu F / cm^2$
$\bar{I}_{ion}$	specific ionic current, $\mu A / cm^2$
I_{ion}	ionic current, $\mu A / \mu F \left(\frac{\bar{I}_{ion}}{C_M}\right)$
Δx	cell length, 100 μM
R_{myo}	myoplasmic resistance, 150 Ωcm
R_g	gap junction conductance, 1.5 Ωcm^2
$R_i = R_{myo} + R_g / \Delta x$	axial resistance per unit length
Δt	time step, 0.005 ms

No flux boundary conditions ($\delta V/\delta x = 0$) were set at the beginning and end of the strand. A 1 ms stimulus (-200 μA/μF) was applied to cell 1 and cell behavior was examined in a central cell (cell 48) where end effects were negligible.

General Parameters

V_m	membrane voltage
E_x	Reversal potential of current x, mV
$\bar{I}_x$	Maximum current carried through channel x, μA/μF
$\bar{G}_x$	Maximum conductance of channel x, ms/μF
X_∞	Steady state value of variable X
X_τ	Time constant of variable
α_y, β_y	Opening and closing rate constants of gate y, respectively
P_S	Membrane permeability to ion S, cm/s
$P_{S,A}$	Permeability ratio of ion S to ion A
γ_S	Activity coefficient of ion S
z_s	Valence of ion S
V_X	Volume of Compartment X
R	Gas constant, 8314 J/kmol/K
T	Temperature, 310^oK
F	Faraday constant, 96,487 C/mol
A_{Cap}	Capacitative membrane area, cm^2
A_{Geo}	Geometric membrane area, cm^2

Currents, Pumps and Exchangers

I_{Na}	Fast Na^+ current, μA/μF

$I_{Na,L}$	Slowly inactivating late Na^+ current, μA/μF
$I_{Na,b}$	Background Na^+ current, μA/μF
I_{CaL}	Ca^{2+} current through the L-type Ca^{2+} channel, μA/μF
$I_{Ca,b}$	Background Ca^{2+} current, μA/μF
$I_{p,Ca}$	Sarcolemmal Ca^{2+} pump, μA/μF
I_{Kr}	Rapid delayed rectifier K^+ current, μA/μF
I_{Ks}	Slow delayed rectifier K^+ current, μA/μF
I_{K1}	Time-independent K^+ current, μA/μF
I_{Kp}	Plateau K^+ current, μA/μF
I_{to1}	4AP-sensitive transient outward K^+ current, μA/μF
I_{to2}	Ca^{2+} dependent transient outward Cl^- current, μA/μF
$I_{Cl,b}$	Background Cl^- current, μA/μF
I_{NaK}	Na^+-K^+ pump, μA/μF
I_{NaCa}	Na^+-Ca^{2+} exchanger, μA/μF
CT_{NaCl}	Na^+-Cl- cotransporter, mmol/L per ms
CT_{KCl}	K^+-Cl- cotransporter, mmol/L per ms
$I_{Ca,t}$	Total transmembrane Ca^{2+} current
	$I_{Ca,t} = I_{Ca,L} + I_{Ca,b} + I_{p,Ca} - 2I_{Na,Ca}$
$I_{Na,t}$	Total transmembrane Na^+ current
	$I_{Na,t} = I_{Na} + 3I_{NaK} + 3I_{NaCa} + I_{NaL} + I_{Nab}$
$I_{K,t}$	Total transmembrane K^+ current
	$I_{K,t} = I_{Ks} + I_{Kr} + I_{K1} + I_{to1} + I_{Kp} - 2I_{NaK}$
$I_{Cl,t}$	Total transmembrane Cl^- current
	$I_{Cl,t} = I_{to2} + I_{Clb}$
I_{tot}	Total transmembrane current
	$I_{tot} = I_{Ca,t} + I_{Na,t} + I_{K,t} + I_{Cl,t}$
I_{stim}	Stimulus current, μA/μF

ACT	I_{CaL} activation parameter
α	I_{CaL} Rate Constant, activation
β	I_{CaL} Rate Constant, deactivation
C	I_{CaL} State, closed (Ca^{2+} free)
O	I_{CaL} State, open (Ca^{2+} free)
I_V	I_{CaL} inactivation parameter (Ca^{2+} free)
x	I_{CaL} Rate Constant, recovery from inactivation (Ca^{2+} free)
y	I_{CaL} Rate Constant, inactivation (Ca^{2+} free)
CI	I_{CaL} State, closed state inactivation (Ca^{2+} free)
OI	I_{CaL} State, open state inactivation (Ca^{2+} free)
I^*_{Ca}	I_{CaL} inactivation parameter, (Ca^{2+} present)
I^*_v	I_{CaL} inactivation parameter, (Ca^{2+} present)
x^*	I_{CaL} Rate Constant, recovery from inactivation (Ca^{2+} free)
y^*	I_{CaL} Rate Constant, inactivation (Ca^{2+} free)
C^*	I_{CaL} State, closed (Ca^{2+} present)
O^*	I_{CaL} State, open (Ca^{2+} present)
δ	I_{CaL} Rate Constant, transition to Ca^{2+} gating tier
θ	I_{CaL} Rate Constant, transition from Ca^{2+} gating tier
δ_I	I_{CaL} Rate Constant, from inactivated state to Ca^{2+} gating tier
θ_I	I_{CaL} Rate Constant, to inactivated state from Ca^{2+} gating tier
CI^*	I_{CaL} State, closed state inactivation (Ca^{2+} present)
OI^*	I_{CaL} State, open state inactivation Ca^{2+} present)
$V_{1/2}$	I_{NaK}, half maximal voltage dependent activation, mV
σ	I_{NaK}, slope factor for voltage dependence at $V_{1/2}$

P_{Na}	I_{NaK}, $[Na^+]_i$ dependent activation parameter
P_K	I_{NaK}, $[K^+]_o$ dependent activation parameter
K_{Nai}	I_{NaK}, $[Na^+]_i$ dependent activation parameter
K_{Ko}	I_{NaK}, $[K^+]_o$ dependent activation parameter
f_V	I_{NaK}, V_m dependent activation parameter
$\overline{G}_{NaK}$	I_{NaK}, maximally activated pump density, μA/μF
a, i_{1f}, i_{1s}	I_{to1}, Activation gate, fast inactivation gate, and slow inactivation gate, respectively
R_{to1}	I_{to1}, Time-independent rectification gate
$P_{Na/K}$	I_{Ks}, Na^+/K^+ permeability ratio**,** 0.01833
$\alpha, \beta, \gamma, \delta, \eta, \theta, \omega, \psi$	I_{Ks}, rate constants
$C_1 - C_{15}$	I_{Ks}, closed states
O_1, O_2	I_{Ks}, open states
O_{Ks}	I_{Ks}, open probability
$\overline{G}_{Ks}$	I_{Ks}, Ca^{2+} dependent maximum conductance
i_2	I_{to2}, Inactivation gate for I_{to2}
$k_{Ca,ito2}$	I_{to2}, half-maximal Ca^{2+} release activation constant
$K_{Ca,ito2}$	I_{to2}, Ca^{2+} dependent activation parameter
v_{max}	I_{NaCa}, Maximal flux, 4.5 μA/μF
k_{sat}	I_{NaCa}, saturation factor at negative potentials, 0.32
η	I_{NaCa}, Position of energy barrier 0.27

$K_{m,Nai}$	I_{NaCa}, $[Na^+]_i$ dissociation constant, 12.3 mmol/L
$K_{m,Nao}$	I_{NaCa}, $[Na^+]_o$ dissociation constant, 87.5 mmol/L
$K_{m,Cai}$	I_{NaCa}, $[Ca^{2+}]_i$ dissociation constant, 0.0036 mmol/L
$K_{m,Cao}$	I_{NaCa}, $[Ca^{2+}]_o$ dissociation constant, 1.3 mmol/L
$K_{mCa,act}$	I_{NaCa}, 1.25e-4 mmol/L
m, h, j	I_{Na}, Activation gate, fast inactivation gate, and slow inactivation gate, respectively
m_L, h_L	$I_{Na,L}$, Activation gate and inactivation gate, respectively
X_r	I_{Kr}, activation gate
R_{Kr}	I_{Kr}, time independent rectification gate
K_1	I_{K1}, inactivation gate of I_{K1}

Ionic fluxes and Diffusion

I_{rel}	Ca^{2+} release from JSR to myoplasm, mmol/L per ms
I_{up}	Ca^{2+} uptake from myoplasm to NSR, mmol/L per ms
I_{leak}	Ca^{2+} leak from JSR to myoplasm, mmol/L per ms
I_{tr}	Ca^{2+} transfer from NSR to JSR, mmol/L per ms
$I_{diff,x}$	Ionic diffusion of Ca^{2+}, Cl^- or Na^+ from SR subspace to myoplasm
$I_{diff,SS}$	Ca^{2+} diffusion from L-type subspace to SR subspace
$CaMK_{bound}$	Fraction of CaMKII binding sites bound to Ca^{2+}/calmodulin
$CaMK_{active}$	Fraction of active CaMKII binding sites
$CaMK_{trap}$	Fraction of autonomous CaMKII binding sites with trapped calmodulin
$CaMK_o$	Equilibrium fraction of active CaMKII binding sites, 0.05

α_{CaMK}, β_{CaMK}	Phosphorylation and dephosphorylation rates of CaMKII, respectively, $\alpha_{CaMK} = 0.05$ ms^{-1} $\beta_{CaMK} = 0.00068$ ms^{-1}
ΔP_{CaMK}	CaMKII-dependent factor of substrate parameter P
$\bar{\Delta}P$	Maximal CaMKII-dependent change in parameter P
$K_{m,CaM}$	CaMK half-saturation coefficient, 0.0015 mmol/L
$K_{m,CaMK}$	Half-saturation coefficient of substrate parameter, 0.15
β_0	I_{rel}, minimal value of β_τ, 4.75 ms
K_β	I_{rel}, half saturation coefficient for $\Delta\beta_{\tau,CaMK}$ 0.28 mmol/L
$\Delta\beta_0$	I_{rel}, Maximal CaMK dependent change for β_τ, 1 mmol/L
$K_{Rel,\infty}$	I_{rel}, half saturation coefficient for $I_{rel,\infty}$, 1 mmol/L
h_{Rel}	I_{rel}, Hill coefficient for $I_{rel,\infty}$, 8
h_β	I_{rel}, Hill coefficient for $\Delta\beta_{\tau,CaMK}$, 10
κ	I_{rel}, Amplitude coefficient for α_{Rel}, 0.1125 μA/μF
$K_{Rel,\tau}$	I_{rel}, Half saturation coefficient for $I_{Rel,\tau}$ 0.0123 mmol/L
$\bar{\Delta}K_{m,PLB}$	I_{up}, Phospholamban Half-saturation factor, 1.7e-4 mmol/L
$\bar{\Delta}I_{up,CaMK}$	I_{up}, Maximal CaMK dependent change in I_{up}, 0.75
$\bar{I}_{up}$	I_{up}, Maximal value of I_{up}, 0.004375 mmol/L per ms
$K_{m,up}$	I_{up}, Half saturation of I_{up}, 0.00092 mmol/L
τ_{tr}	I_{tr}, Time constant for NSR/JSR Ca^{2+} transfer, 25 ms

Compartments

i	intracellular space
o	extracellular space
SR	sarcoplasmic reticulum

JSR	junctional sarcoplasmic reticulum
NSR	network sarcoplasmic reticulum
SS,SR	SR Ca^{2+} release subspace
SS,CaL	L-type Ca^{2+} entry subspace

Concentrations and Buffering

$[Ca^{2+}]_x$	Calcium concentration in compartment X, mmol/L
$[Na^{+}]_x$	Sodium concentration in compartment X, mmol/L
$[K^{+}]_x$	Potassium concentration in compartment X, mmol/L
$[Cl^{-}]_x$	Chloride concentration in compartment X, mmol/L
csqn	Calsequestrin, Ca^{2+} buffer in JSR
trpn	Troponin, Ca^{2+} buffer in JSR
BSR_X	Anionic SR binding sites for Ca^{2+} (SS or SS,CaL)
BSL_X	Anionic sarcolemmal binding sites for Ca^{2+} (SS or SS,CaL)
$[\overline{trpn}]$	Maximum troponin concentration, 0.07 mmol/L
$[\overline{cmdn}]$	Maximum calmodulin concentration, 0.05 mmol/L
$K_{m,cmdn}$	Calmodulin half saturation, 0.00238 mmol/L
$K_{m,trpn}$	Troponin half saturation, 0.0005 mmol/L
$[\overline{csqn}]$	Calsequestrin concentration, 10.0 mmol/L
$K_{m,csqn}$	Troponin half saturation, 0.8 mmol/L

Cell geometry

Length (L) = 0.01 cm; radius (r) = 0.0011 cm

Cell volume: $V_{cell} = \pi \cdot r^2 \cdot L = 38e-6\ \mu L$

Geometric membrane area: $A_{geo} = 2\pi \cdot r^2 + 2\pi \cdot r \cdot L = 0.767e-4\ cm^2$

Capacitative membrane area: $A_{cap} = R_{CG} \cdot A_{geo} = 1.534e-4\ \text{cm}^2$

Myoplasmic volume: $V_{myo} = V_{cell} \cdot 68\% = 25.84e-6\ \mu\text{L}$

Mitochondrial volume: $V_{mito} = V_{cell} \cdot 26\% = 9.88e-6\ \mu\text{L}$

SR volume: $V_{SR} = V_{cell} \cdot 6\% = 2.28e-6\ \mu\text{L}$

NSR volume: $V_{NSR} = V_{cell} \cdot 5.52\% = 2.098e-6\ \mu\text{L}$

JSR volume: $V_{JSR} = V_{cell} \cdot 0.48\% = 0.182e-6\ \mu\text{L}$

SS,SR volume: $V_{SS,SR} = V_{cell} \cdot 2.0\% = 0.76e-6\ \mu\text{L}$

SS,CaL volume: $V_{SS,CaL} = V_{cell} \cdot 0.2\% = 0.076e-6\ \mu\text{L}$

External Concentrations

$[Ca^{2+}]_o$	1.8 mmol/L
$[Cl^-]_o$	100 mmol/L
$[K^+]_o$	5.4 mmol/L
$[Na^+]_o$	140 mmol/L

Resting voltage and concentrations (Single cell, unpaced for 5400 seconds)

V_m	-87.472528 mV
$[Ca^{2+}]_i$	0.000096833 mmol/L
$[Ca^{2+}]_{SS,SR}$	0.000138151 mmol/L
$[Ca^{2+}]_{SS,CaL}$	0.000143898 mmol/L
$[Ca^{2+}]_{JSR}$	1.133109 mmol/L
$[Ca^{2+}]_{NSR}$	1.159942 mmol/L

$[Cl^-]_i$	20.26905mmol/L
$[K^+]_i$	145.5689 mmol/L
$[Na^+]_i$	6.935575 mmol/L
$[Na^+]_{SS}$	6.935607 mmol/L
$[Cl^-]_{SS}$	20.26905 mmol/L

Model Equations

1. I_{CaL}

See Chapter 2 for description of model and experimental fits. Note that this formulation was modified in the NZ model (see Appendix B).

$$ACT_\tau = 0.59+0.8\cdot\frac{\exp(0.052\cdot(V_m+13))}{1+\exp(0.132\cdot(V_m+13))}$$

$$ACT_\infty = \frac{1}{1.0+\exp(-(V_m-13.56)/9.45)}$$

$$\alpha = \frac{ACT_\infty}{ACT_\tau}$$

$$\beta = \frac{1-ACT_\infty}{ACT_\tau}$$

$$I_{V,\infty} = \frac{1/(1+\exp((V_m+17.5)/3))+0.25}{1.25}$$

$$I_{V,\tau} = \frac{1}{\frac{1}{24.828\cdot(1+\exp(((V_m+49.10)/10.349)))}+\frac{1}{30.553\cdot(1+\exp((-(V_m+0.213)/10.807)))}}$$

$$x = \frac{I_{V,\infty}}{I_{V,\tau}}$$

$$y = \frac{1-I_{V,\infty}}{I_{V,\tau}}$$

$$I_{Ca}^{*} = 25 - \frac{17.5}{1+\left(\frac{0.003}{[Ca^{2+}]_{SS,CaL}}\right)^4}$$

$$I^{*}_{V,\tau} = \frac{1}{\frac{1}{24.828\cdot(1+\exp(((V_m+49.10)/10.349)))} + \frac{1}{I^{*}_{Ca}\cdot(1+\exp((-(V_m+0.213)/10.807)))}}$$

$$I^{*}_{V,\infty} = \frac{1/(1+\exp(-(V_m+17.5)/3))+0.0001}{1.0001}$$

$$x^{*} = \frac{I^{*}_{V,\infty}}{I^{*}_{V,\tau}}$$

$$y^{*} = \frac{1-I^{*}_{V,\infty}}{I^{*}_{V,\tau}}$$

$$\delta = \frac{3}{1+\left(\frac{0.003}{[Ca^{2+}]_{SS,CaL}}\right)^4}$$

$$\theta = 1$$

$$\theta_I = 0.000001$$

$$\delta_I = \theta_I \cdot \left(\frac{x\cdot y^{*}\cdot\delta}{y\cdot x^{*}\cdot\theta}\right)$$

State transitions:

$$\frac{dC}{dt} = -(\alpha+\delta+y)\cdot C + \beta\cdot O + \theta\cdot C^{*} + x\cdot CI$$

$$\frac{dO}{dt} = -(\beta+\delta+y)\cdot O + \alpha\cdot C + \theta\cdot O^{*} + x\cdot OI$$

$$\frac{dC^{*}}{dt} = -(\alpha+\theta+y^{*})\cdot C^{*} + \delta\cdot C + \beta\cdot O^{*} + x^{*}\cdot CI^{*}$$

$$\frac{dO^{*}}{dt} = -(\beta+\theta+y^{*})\cdot O^{*} + \delta\cdot O + \alpha\cdot C^{*} + x^{*}\cdot OI^{*}$$

$$\frac{dCI}{dt} = -(\alpha + \delta_I + x)\cdot CI + y\cdot C + \theta_I \cdot CI^* + \beta \cdot OI$$

$$\frac{dOI}{dt} = -(\beta + \delta_I + x)\cdot OI + y\cdot O + \theta_I \cdot OI^* + \alpha \cdot CI$$

$$\frac{dCI^*}{dt} = -(\alpha + \theta_I + x^*)\cdot CI^* + \delta_I \cdot CI + y^* \cdot C^* + \beta \cdot OI^*$$

$$\frac{dOI^*}{dt} = -(\beta + \theta_I + x^*)\cdot OI^* + \delta_I \cdot OI + y^* \cdot O^* + \alpha \cdot CI^*$$

Current:

$$P_{Ca} = 1.5552\times10^{-4} \text{ cm/s}; \gamma_{Cai} = 1; \gamma_{Cao} = 0.341$$

$$\bar{I}_{CaL} = P_{Ca}\cdot z_{Ca}^2 \cdot \frac{V\cdot F^2}{RT}\cdot \frac{\gamma_{Cai}\cdot[Ca^{2+}]_{SS,CaL}\cdot\exp(z_{Ca}\cdot V_m \cdot F/(RT)) - \gamma_{Cao}\cdot[Ca^{2+}]_0}{\exp(z_{Ca}\cdot V_m\cdot F/(RT)) - 1}$$

$$I_{CaL} = \bar{I}_{CaL}\cdot(O + O^*)$$

2. Slow component of the delayed rectifier potassium channel (I_{Ks})

See Chapter 2 for description of model and experimental fits.

Kinetic parameters:

$$\alpha = 1.4864\cdot10^{-2}\cdot\exp\left(2.9877\cdot10^{-2}\cdot V_m\cdot(F/(R\cdot T))\right)$$

$$\beta = 8.3986\cdot10^{-2}\cdot\exp\left(-5.5461\cdot10^{-2}\cdot V_m\cdot(F/(R\cdot T))\right)$$

$$\gamma = 1.4601\cdot10^{-2}\cdot\exp\left(2.4465\cdot10^{-1}\cdot V_m\cdot(F/(R\cdot T))\right)$$

$$\delta = 3.1173\cdot10^{-3}\cdot\exp\left(-4.2625\cdot10^{-1}\cdot V_m\cdot(F/(R\cdot T))\right)$$

$$\eta = 7.7320\cdot10^{-2}\cdot\exp\left(-6.4726\cdot10^{-2}\cdot V_m\cdot(F/(R\cdot T))\right)$$

$$\theta = 8.9538\cdot10^{-2}$$

$$\omega = 7.9405\cdot10^{-1}\cdot\exp\left(-8.0174\cdot10^{-2}\cdot V_m\cdot(F/(R\cdot T))\right)$$

$$\psi = 5.8638\cdot10^{-1}\cdot\exp\left(2.8206\cdot10^{-1}\cdot V_m\cdot(F/(R\cdot T))\right)$$

State transitions:

$$\frac{dC_1}{dt} = -(4\alpha)\cdot C_1 + \beta \cdot C_2$$

$$\frac{dC_2}{dt} = -(3\alpha + \beta + \gamma)\cdot C_2 + 4\alpha \cdot C_1 + 2\beta \cdot C_3 + \delta \cdot C_6$$

$$\frac{dC_3}{dt} = -(2\alpha + 2\beta + 2\gamma)\cdot C_3 + 3\alpha \cdot C_2 + 3\beta \cdot C_4 + \delta \cdot C_7$$

$$\frac{dC_4}{dt} = -(\alpha + 3\beta + 3\gamma)\cdot C_4 + 2\alpha \cdot C_3 + 4\beta \cdot C_5 + \delta \cdot C_8$$

$$\frac{dC_5}{dt} = -(4\beta + 4\gamma)\cdot C_5 + \alpha \cdot C_4 + \delta \cdot C_9$$

$$\frac{dC_6}{dt} = -(3\alpha + \delta)\cdot C_6 + \beta \cdot C_7 + \gamma \cdot C_2$$

$$\frac{dC_7}{dt} = -(2\alpha + \beta + \gamma + \delta)\cdot C_7 + 3\alpha \cdot C_6 + 2\beta \cdot C_8 + 2\gamma \cdot C_3 + 2\delta \cdot C_{10}$$

$$\frac{dC_8}{dt} = -(\alpha + 2\beta + 2\gamma + \delta)\cdot C_8 + 2\alpha \cdot C_7 + 3\beta \cdot C_9 + 3\gamma \cdot C_4 + 2\delta \cdot C_{11}$$

$$\frac{dC_9}{dt} = -(3\beta + 3\gamma + \delta)\cdot C_9 + \alpha \cdot C_8 + 4\gamma \cdot C_5 + 2\delta \cdot C_{12}$$

$$\frac{dC_{10}}{dt} = -(2\alpha + 2\delta)\cdot C_{10} + \beta \cdot C_{11} + \gamma \cdot C_7$$

$$\frac{dC_{11}}{dt} = -(\alpha + \beta + \gamma + 2\delta)\cdot C_{11} + 2\alpha \cdot C_{10} + 2\beta \cdot C_{12} + 2\gamma \cdot C_8 + 3\delta \cdot C_{13}$$

$$\frac{dC_{12}}{dt} = -(2\beta + 2\gamma + 2\delta)\cdot C_{12} + \alpha \cdot C_{11} + 3\gamma \cdot C_9 + 3\delta \cdot C_{14}$$

$$\frac{dC_{13}}{dt} = -(\alpha + 3\delta)\cdot C_{13} + \beta \cdot C_{14} + \gamma \cdot C_{11}$$

$$\frac{dC_{14}}{dt} = -(\beta + \gamma + 3\delta)\cdot C_{14} + \alpha \cdot C_{13} + 2\gamma \cdot C_{12} + 4\delta \cdot C_{15}$$

$$\frac{dC_{15}}{dt} = -(4\delta + \theta)\cdot C_{15} + \gamma \cdot C_{14} + \eta \cdot O_1$$

$$\frac{dO_1}{dt} = -(\eta + \psi)\cdot O_1 + \theta \cdot C_{15} + \omega \cdot O_2$$

$$\frac{dO_2}{dt} = -(\omega)\cdot O_2 + \psi \cdot O_1$$

Current:

$$\overline{G}_{Ks} = 0.0826 \cdot \left(1 + \frac{0.6}{1 + \left(\frac{3.8 \cdot 10^{-5}}{[Ca^{2+}]_i} \right)^{1.4}} \right)$$

$$O_{Ks} = O_1 + O_2$$

$$E_{Ks} = \frac{R \cdot T}{F} \cdot \log \frac{[K^+]_o + P_{Na/K} \cdot [Na^+]_o}{[K^+]_i + P_{Na/K} \cdot [Na^+]_i}$$

$$I_{Ks} = \overline{G_{Ks}} \cdot O_{Ks} \cdot (V_m - E_{Ks})$$

4. I_{NaK}

See Chapter 2 for description of model and experimental fits.

$V_{1/2} = -92$ mV

$\sigma = 1$

$$\phi = \sigma \cdot (V_m - V_{1/2}) \cdot \frac{F}{RT}$$

$$f_v = \frac{1}{1 + \exp(-\phi)}$$

$K_{Ko} = 1.5$ mM

$$P_K = \frac{[K^+]_o}{[K^+]_o + K_{Ko}}$$

$K_{Nai} = 2.6$ mM

$$P_{Na} = \left(\frac{[Na^+]_i}{[Na^+]_i + K_{Nai}} \right)^3$$

$\overline{I}_{NaK} = 1.4$ mS/μF

$$I_{NaK} = \bar{I}_{NaK} \cdot f_v \cdot P_{Na} \cdot P_K$$

5. I_{to1}

See Chapter 2 for description of model and experimental fits.

$$E_{to1} = \frac{RT}{F} \cdot \ln\left(\frac{[K^+]_o}{[K^+]_i}\right)$$

$$R_{to1} = \exp(\frac{V_m}{550})$$

$$\beta_a = \frac{3.5}{\left(1+\exp\left(\frac{(V_m+100)}{29.3814}\right)\right)}$$

$$\alpha_a = \frac{1}{1.2089 \cdot \left(1+\exp\left(\frac{(V_m-18.4099)}{-29.3814}\right)\right)}$$

$$\tau_a = \frac{1}{\alpha_a + \beta_a}$$

$$a_\infty = \frac{1}{\left(1+\exp\left(\frac{(V_m+9.437)}{-7.133}\right)\right)}$$

$$\alpha_{i1f} = \frac{0.025}{\left(1+\exp\left(\frac{(V_m+58)}{5}\right)\right)}$$

$$\beta_{i1f} = \frac{1}{9.7953 \cdot \left(1+\exp\left(\frac{(V_m+19)}{-9}\right)\right)}$$

$$\alpha_{i1s} = \frac{1}{250 \cdot \left(1+\exp\left(\frac{(V_m+60)}{5}\right)\right)}$$

$$\beta_{i1s} = \beta_{i1f}$$

$\overline{G}_{to1} = 0.4975 \text{ mS}/\mu\text{F}$

$$I_{to1} = \overline{G}_{to1} \cdot a^3 \cdot i_{1f} \cdot i_{1s} \cdot R_{to1} \cdot (V_m - E_{to1})$$

6. $\mathbf{I_{to2}}$

See Chapter 2 for description of model and experimental fits.

$k_{Ca,ito2} = 0.4$

$$K_{Ca,ito2} = 1 - \frac{1}{1 + \left(\frac{I_{rel}}{k_{Ca,ito2}} \right)^2}$$

$\tau_{i2} = 8$

$$\alpha_{i2} = \frac{0.025}{\left(1 + \exp\left(\frac{(V_m + 58)}{5} \right) \right)}$$

$$\beta_{i2} = \frac{1}{5 \cdot \left(1 + \exp\left(\frac{(V_m + 19)}{-9} \right) \right)}$$

$$i_{2,\infty} = \frac{\alpha_{i2}}{\alpha_{i2} + \beta_{i2}}$$

$P_{Cl} = 9\text{e-}7 \text{ cm/s}$

$$\bar{I}_{to2} = P_{Cl} \cdot z_{Cl}^2 \cdot \frac{V_m F^2}{RT} \cdot \frac{[Cl]_i - [Cl]_o \cdot \exp(-z_{Cl} \cdot V_m \cdot F/(RT))}{1 - \exp(-z_{Cl} \cdot V_m \cdot F/(RT))}$$

$$I_{to2} = \bar{I}_{to2} \cdot i_{2f} \cdot K_{Ca,ito2}$$

7. $\mathbf{I_{NaCa}}$

The Na^+-Ca^{2+} exchanger formulation was adopted from Weber and Bers. 20% of exchangers were located in the restricted space, consistent with experimental results and previous work from our lab (Faber et al., 2007).

$$I_{NaCa.x} = \frac{f_x \cdot v_{\max} \cdot \left([Na^+]_x^3 \cdot [Ca^{2+}]_o \cdot \exp\left(\frac{\eta \cdot VF}{RT} \right) - [Na^+]_o^3 \cdot [Ca^{2+}]_x \cdot \exp\left(\frac{(\eta - 1) \cdot VF}{RT} \right) \right)}{\left(1 + \left(\frac{K_{mCa,act}}{[Ca^{2+}]_x} \right)^2 \right) \cdot \left(1 + k_{sat} \exp\left(\frac{(\eta - 1) \cdot VF}{RT} \right) \right) \cdot \left(\begin{array}{l} K_{m,Cao}[Na^+]_x^3 + K_{m,Nao}^3[Ca^{2+}]_x + \\ K_{m,Nai}^3[Ca^{2+}]_o \cdot \left(1 + \frac{[Ca^{2+}]_x}{K_{m,Cai}} \right) + \\ K_{m,Cai}[Na^+]_o^3 \cdot \left(1 + \frac{[Na^+]_x^3}{K_{m,Nai}^3} \right) + \\ [Na^+]_x^3 \cdot [Ca^{2+}]_o + [Na^+]_o^3 \cdot [Ca^{2+}]_x \end{array} \right)}$$

where

$I_{NaCa} = I_{NaCa,SS,SR} + I_{NaCa,i}$

and if

$x = SS, SR$ then $f_X = f_{SS,SR} = 0.2,\ [Na^+]_x = [Na^+]_{SS,SR}$ and $[Ca^{2+}]_x = [Ca^{2+}]_{SS,SR}$

$x = i$ then $f_X = f_i = 0.8,\ [Na^+]_x = [Na^+]_i$ and $[Ca^{2+}]_x = [Ca^{2+}]_i$

8. I_{Na}

Fast Na^+ current density (I_{Na}) was adjusted to achieve conduction velocity (Spach et al., 2000), maximum upstroke velocity (Di Diego et al., 1996) and maximum upstroke voltage (Di Diego et al., 1996) consistent with data in canine epicardial tissue. Na^+ current recovery from inactivation was adjusted to fit data on recovery of upstroke velocity in canine epicardial myocytes (Lue and Boyden, 1992). Note that this formulation was modified in the NZ model (see Appendix B).

$\bar{G}_{Na} = 9.075$ mS/μF

$$E_{Na} = \frac{RT}{F} \cdot \ln\left(\frac{[Na^+]_o}{[Na^+]_i}\right)$$

$$\alpha_m = \frac{0.32 \cdot (V_m + 47.13)}{1 - \exp(-0.1 \cdot (V_m + 47.13))}$$

$$\beta_m = 0.08 \cdot \exp\left(\frac{-V_m}{11}\right)$$

If $V_m \geq -40.0$ mV

$$\alpha_h = 0.0$$

$$\beta_h = \frac{1}{0.13 \cdot \left(1 + \exp\left(\frac{V_m + 10.66}{-11.1}\right)\right)}$$

$$\alpha_j = 0.0$$

$$\beta_j = \frac{0.3 \cdot (-2.535 \times 10^{-7}) \cdot V_m}{\exp(-0.1 \cdot (V_m + 32)) + 1}$$

else

$$\alpha_h = 0.135 \cdot \exp\left(\frac{(80.0 + V_m)}{-6.8}\right)$$

$$\beta_h = 3.56 \cdot \exp(0.079 \cdot V_m) + 3.1 \times 10^5 \cdot \exp(0.35 \cdot V_m)$$

$$\alpha_j = \frac{(-1.2714 \times 10^5 \cdot \exp(0.2444 \cdot V_m) - 6.948 \times 10^{-5} \cdot \exp(-0.04391 \cdot V_m)) \cdot (V_m + 37.78)}{1 + \exp(0.311 \cdot (V_m + 79.23))}$$

$$\beta_j = \frac{0.1212 \cdot \exp(-0.01052 \cdot V_m)}{1 + \exp(-0.1378 \cdot (V_m + 40.14))}$$

$$I_{Na} = \bar{G}_{Na} \cdot m^3 \cdot h \cdot j \cdot (V_m - E_{Na})$$

9. I_{Nab}, CT_{NaCl}, and CT_{KCl}

Background Na^+ current (I_{Nab}) and co-transporter fluxes were required to maintain a resting $[Na^+]_i$ concentration consistent with measurements in canine epicardial myocytes (Gao et

al., 2005). Na^+ permeability for the background Na^+ current was given by the constant field equation, following the formulation used by Gao et al. (Gao et al., 2005):

$$\phi = \frac{F \cdot V_m}{R \cdot T}$$

$$P_{Nab} = 0.32 \times 10^{-8} \text{ cm/s}$$

$$I_{Nab} = F \cdot P_{nab} \cdot \phi \cdot \frac{([Na^+]_i \cdot \exp(\phi) - [Na^+]_o)}{\exp(\phi) - 1}$$

K^+-Cl^- (CT_{KCl}) and Na^+-Cl^- (CT_{NaCl}) cotransporter formulations were based on those in the original HRd model, with modified density.

$$E_{Na} = \frac{RT}{F} \cdot \ln\left(\frac{[Na^+]_o}{[Na^+]_i}\right)$$

$$E_K = \frac{RT}{F} \cdot \ln\left(\frac{[K^+]_o}{[K^+]_i}\right)$$

$$E_{Cl} = -\frac{RT}{F} \cdot \ln\left(\frac{[Cl^-]_o}{[Cl^-]_i}\right)$$

$$\overline{CT}_{NaCl} = 2.46108\text{e-}05 \text{ mmol/L per ms}$$

$$CT_{NaCl} = \overline{CT}_{NaCl} \cdot \frac{(E_{Na} - E_{Cl})^4}{(E_{Na} - E_{Cl})^4 + 87.8251^4}$$

$$\overline{CT}_{KCl} = 1.77\text{e-}05 \text{ mmol/L per ms}$$

$$CT_{KCl} = \overline{CT}_{KCl} \cdot \frac{(E_K - E_{Cl})}{(E_K - E_{Cl}) + 87.8251}$$

10. I_{Kr}

The formulation for the rapid component of the delayed rectifier potassium current is equivalent to that in the original HRd model.

$$\overline{G}_{Kr} = 0.0138542 \cdot \sqrt{\frac{[K^+]_o}{5.4}}$$

$$E_{Kr} = \frac{RT}{F} \cdot \ln\left(\frac{[K^+]_o}{[K^+]_i}\right)$$

$$\tau_{Xr} = \frac{1}{\frac{0.6\times10^{-3}\cdot(V_m - 1.7384)}{1-\exp(-0.136\cdot(V_m - 1.7384))} + \frac{3\times10^{-4}\cdot(V_m + 38.3608)}{\exp(0.1522\cdot(V_m + 38.3608))-1}}$$

$$X_{r\infty} = \frac{1}{1+\exp(-(V_m + 10.0805)/4.25)}$$

$$R_{Kr} = \frac{1}{1+\exp((V_m + 10)/15.4)}$$

$$I_{Kr} = \overline{G}_{Kr} \cdot X_r \cdot R_{Kr} \cdot (V_m - E_{Kr})$$

11. I_{K1}

The formulation for the inward rectifier potassium current is equivalent to that in the original HRd model.

$$E_{K1} = \frac{RT}{F} \cdot \ln\left(\frac{[K^+]_o}{[K^+]_i}\right)$$

$$\alpha_{K1} = \frac{1.02}{1+\exp(0.2385\cdot(V_m - E_{K1} - 59.215))}$$

$$\beta_{K1} = \frac{0.49124\cdot\exp(0.08032\cdot(V_m - E_{K1} + 5.476)) + \exp(0.06175\cdot(V_m - E_{K1} - 594.31))}{1+\exp(-0.5143\cdot(V_m - E_{K1} + 4.753))}$$

$$K_1 = \frac{\alpha_{K1}}{\alpha_{K1} + \beta_{K1}}$$

$$\overline{G}_{K1} = 0.5 \cdot \sqrt{\frac{[K^+]_o}{5.4}}$$

$$I_{K1} = \overline{G}_{K1} \cdot K_1 \cdot (V_m - E_{K1})$$

12. I_{Kp}

The formulation for the plateau potassium current is equivalent to that in the original HRd model.

$$E_{Kp} = \frac{RT}{F} \cdot \ln\left(\frac{[K^+]_o}{[K^+]_i}\right)$$

$$K_p = \frac{1}{1+\exp\left(\frac{7.488 - V_m}{5.98}\right)}$$

$$\overline{G}_{Kp} = 2.76 \times 10^{-3} \text{ mS}/\mu\text{F}$$

$$I_{Kp} = \overline{G}_{Kp} \cdot K_p \cdot (V_m - E_{Kp})$$

13. I_{pca}

The formulation for the sarcolemmal calcium pump is equivalent to that in the original HRd model.

$$\overline{G}_{p,Ca} = 0.0575 \text{ mS}/\mu\text{F}; K_{m,pCa} = 0.0005\text{mM}$$

$$I_{p,Ca} = \overline{G}_{p,Ca} \cdot \frac{[Ca^{2+}]_i}{K_{m,pCa} + [Ca^{2+}]_i}$$

14. $I_{ca,b}$

The formulation for the background calcium current is equivalent to that in the original HRd model.

$$P_{Ca,b} = 1.995\text{e-}07\text{cm/s}; \gamma_{Cai} = 1; \gamma_{Cai} = 0.341$$

$$I_{Ca,b} = P_{Ca,b} \cdot z_{Ca}^2 \cdot \frac{V_m \cdot F^2}{RT} \cdot \frac{\gamma_{Cai} \cdot [Ca^{2+}]_i \cdot \exp(z_{Ca} \cdot V_m \cdot F/(RT)) - \gamma_{Cao} \cdot [Ca^{2+}]_o}{\exp(z_{Ca} \cdot V_m \cdot F/(RT)) - 1}$$

15. $I_{Cl,b}$

The formulation for the background chloride current is equivalent to that in the original HRd model.

$$\overline{G}_{Cl,b} = 2.25\times10^{-4}\ \mu\text{A}/\mu\text{F}$$

$$E_{Cl} = -\left(\frac{RT}{F}\right)\cdot\ln\left(\frac{[Cl^-]_o}{[Cl^-]_i}\right)$$

$$I_{Cl,b} = \overline{G}_{Cl,b}\cdot(V_m - E_{Cl})$$

16. $I_{Na,L}$

The formulation for the late Na^+ current is equivalent to that in the original HRd model. Note that a new INa,L formulation was developed for the NZ model (see Appendix B).

$$E_{Na,L} = \frac{RT}{F}\cdot\ln\left(\frac{[Na^+]_o}{[Na^+]_i}\right)$$

$$\alpha_{m,L} = \frac{0.32\cdot(V_m + 47.13)}{1-\exp(-0.1\cdot(V_m + 47.13))}$$

$$\beta_{m,L} = 0.08\cdot\exp\left(\frac{-V_m}{11.0}\right)$$

$$h_{L,\infty} = \frac{1}{1+\exp((V_m + 91)/6.1)}$$

$$\tau_{hL} = 600\ \text{ms}$$

$$\overline{G}_{Na,L} = 0.0065\ \text{ms}/\mu\text{F}$$

$$I_{Na,L} = \overline{G}_{Na,L}\cdot m_L^3\cdot h_L\cdot(V_m - E_{Na,L})$$

17. SR Ca^{2+} fluxes

Formulations for SR Ca^{2+} fluxes were adopted from Hund et al. (Hund and Rudy, 2004) and Livshitz et al.(Livshitz and Rudy, 2007)

SR Release

Model SR release formulation is equivalent to that in Livshitz et al. (Livshitz and Rudy, 2007).

$$\Delta\beta_{\tau,CaMK} = \Delta\beta_0 / [1 + (K_\beta / CaMK_{active})^{h_\beta}]$$

$$\alpha_{Rel} = \kappa\beta_\tau mmol \cdot L^{-1} \cdot ms^{-1}$$ Type equation here.

$$\beta_\tau = \beta_0 (1 + \Delta\beta_{\tau,CaMK})$$

$$I_{rel,\tau} = \frac{\beta_\tau}{1 + \left(K_{Rel,\tau} / [Ca^{2+}]_{JSR} \right)}$$

$$I_{rel,\infty} = \frac{\alpha_{Rel} I_{Ca,L}}{1 + \left(K_{Rel,\infty} / [Ca^{2+}]_{JSR} \right)^{h_{Rel}}}$$

$$\frac{dI_{rel}}{dt} = -\frac{I_{rel,\infty} + I_{rel}}{I_{rel,\tau}}$$

SR Uptake

Model SR release formulation is equivalent to that in Livshitz et al. (Livshitz and Rudy, 2007).

$$\Delta K_{m,PLB} = \bar{\Delta} K_{m,PLB} \cdot \frac{CaMK_{active}}{K_{m,CaMK} + CaMK_{active}}$$

$$\Delta I_{up,CaMK} = \bar{\Delta} I_{up,CaMK} \cdot \frac{CaMK_{active}}{K_{m,CaMK} + CaMK_{active}}$$

$$I_{up} = \left(\Delta I_{up,CaMK} + 1 \right) \cdot \bar{I}_{up} \cdot \frac{[Ca^{2+}]_i}{[Ca^{2+}]_i + K_{m,up} - \Delta K_{m,PLB}}$$

SR Leak

Model SR leak is equivalent to that in Livshitz et al. (Livshitz and Rudy, 2007).

$$I_{leak} = \frac{0.004375}{\overline{NSR}} \cdot [Ca^{2+}]_{NSR}; \overline{NSR} = 15$$

JSR/NSR transfer

Time constant of NSR/JSR Ca2+ transfer was adjusted to 25 ms.

$$I_{tr} = \frac{\left([Ca^{2+}]_{NSR} - [Ca^{2+}]_{JSR}\right)}{\tau_{tr}}$$

18. Intracellular subspaces and myoplasmic concentrations

L-type Ca^{2+} channels are located in a local subspace (SS,CaL). Ryanodine receptors, I_{to2} channels and 20% of Na^{+}-Ca^{2+} exchangers are located in a Ca^{2+} release subspace (SS,SR). Ca^{2+} diffusion occurs between SS,CaL and SS,SR ($I_{diff,SS}$) and diffusion of Ca^{2+}, Na^{+} and Cl^{-} occur between the SS,SR and the bulk myoplasm ($I_{diff,Ca}$, $I_{diff,Na}$ and $I_{diff,Cl}$).

Calcium

$$\tau_{Diff} = 0.2 \text{ ms}$$

$$\tau_{Diff,SS} = 2 \text{ ms}$$

$$I_{Diff,SS} = \frac{[Ca^{2+}]_{SS,SR} - [Ca^{2+}]_{SS,CaL}}{\tau_{Diff,SS}}$$

$$I_{Diff} = \frac{[Ca^{2+}]_{SS,SR} - [Ca^{2+}]_{i}}{\tau_{Diff}}$$

$$\frac{d[Ca^{2+}]_i}{dt} = -\left(\frac{(I_{cab} + I_{pca} - 2 \cdot I_{NaCa,i}) \cdot A_{cap} \cdot C_m}{z_{Ca} \cdot F \cdot V_{myo}} + (I_{up} - I_{leak}) \frac{V_{nsr}}{V_{myo}} - I_{Diff} \frac{V_{SS,SR}}{V_{myo}}\right)$$

$$[Ca^{2+}]_{i,t} = [trpn] + [cmdn] + [Ca^{2+}]_i + \Delta[Ca^{2+}]_i$$

$$b = [\overline{cmdn}] + [\overline{trpn}] - [Ca^{2+}]_{i,t} + K_{m,trpn} + K_{m,cmdn}$$

$$c = K_{m,cmdn} \cdot K_{m,trpn} - [Ca^{2+}]_{i,t} \cdot (K_{m,trpn} + K_{m,cmdn}) + [\overline{trpn}] \cdot K_{m,cmdn} + [\overline{cmdn}] \cdot K_{m,trpn}$$

$$d = -K_{m,trpn} \cdot K_{m,cmdn} \cdot [Ca^{2+}]_{i,t}$$

$$[Ca^{2+}]_i = \frac{2}{3}\sqrt{b^2 - 3c} \cdot \cos\left(\frac{1}{3} \cdot \cos^{-1}\left(\frac{9bc - 2b^3 - 27d}{2\left(b^2 - 3c\right)^{1.5}}\right)\right) - \frac{b}{3}$$

$$\beta_{SS} = \frac{1}{1 + \frac{\overline{BSR} \cdot K_{m,BSR}}{\left(K_{m,BSR} + [Ca^{2+}]_X\right)^2} + \frac{\overline{BSL} \cdot K_{m,BSL}}{\left(K_{m,BSL} + [Ca^{2+}]_X\right)^2}}$$

$$\overline{BSR} = 0.047\text{mM}; K_{m,BSR} = 0.00087\text{mM}$$

$$\overline{BSL} = 1.124\text{mM}; K_{m,BSL} = 0.0087\text{mM}$$

$$\frac{d[Ca^{2+}]_{SS}}{dt} = \beta_{SS}\left(\frac{2 \cdot I_{NaCa,ss} \cdot A_{cap} \cdot C_m}{z_{Ca} \cdot F \cdot V_{SS}} + I_{rel} \cdot \frac{V_{JSR}}{V_{SS}} - I_{Diff} - I_{Diff,SS}\right)$$

$$\frac{d[Ca^{2+}]_{SS(CaL)}}{dt} = \beta_{SS}\left(-\frac{I_{Ca(L)} \cdot A_{Cap} \cdot C_m}{z_{Ca} \cdot F \cdot V_{SS(CaL)}} + \frac{V_{SS}}{V_{SS(CaL)}} \cdot I_{Diff,SS}\right)$$

$$\frac{d[Ca^{2+}]_{JSR}}{dt} = I_{tr} - I_{rel}$$

$$b = [\overline{csqn}] - [csqn] - [Ca^{2+}]_{JSR} - \Delta[Ca^{2+}]_{JSR} + K_{m,csqn}$$

$$c = K_{m,csqn} \cdot \left([csqn] + [Ca^{2+}]_{JSR} + \Delta[Ca^{2+}]_{JSR}\right)$$

$$[Ca^{2+}]_{JSR} = \frac{\sqrt{b^2 + 4c} - b}{2}$$

$$\frac{d[Ca^{2+}]_{NSR}}{dt} = I_{up} - I_{leak} - I_{tr} \cdot \frac{V_{JSR}}{V_{NSR}}$$

Sodium

$$I_{Diff,Na} = \frac{[Na^+]_{SS} - [Na^+]_i}{\tau_{Diff,SS}}$$

$$\frac{d[Na^+]_i}{dt} = -\left(\frac{(3 \cdot I_{NaCa,i} + 3 \cdot I_{NaK} + I_{Na} + I_{NaL} + I_{Nab}) \cdot A_{Cap} \cdot C_m}{z_{Na} \cdot F \cdot V_{myo}} - CT_{NaCl} - I_{Diff,Na} \cdot \frac{V_{SS}}{V_{myo}} \right)$$

$$\frac{d[Na^+]_{SS}}{dt} = -\left(\frac{3 \cdot I_{NaCa,SS} \cdot A_{Cap} \cdot C_m}{z_{Na} \cdot F \cdot V_{ss}} + I_{Diff,Na} \right)$$

Chloride

$$I_{Diff,Cl} = \frac{[Cl^-]_{SS} - [Cl^-]_i}{\tau_{Diff,SS}}$$

$$\frac{d[Cl^-]_i}{dt} = -\left(\frac{I_{Clb} \cdot A_{Cap} \cdot C_m}{z_{Cl} \cdot F \cdot V_{myo}} - CT_{NaCl} - CT_{KCl} - I_{Diff,Cl} \cdot \frac{V_{SS}}{V_{myo}} \right)$$

$$\frac{d[Cl^-]_{SS}}{dt} = -\left(\frac{I_{to2} \cdot A_{Cap} \cdot C_m}{z_{Cl} \cdot F \cdot V_{ss}} + I_{Diff,Cl} \right)$$

Potassium

$$\frac{d[K^+]_i}{dt} = -\left(\frac{I_{K,tot} \cdot A_{Cap} \cdot C_m}{z_{Cl} \cdot F \cdot V_{myo}} - CT_{KCl} \right)$$

CamKII

Model CaMKII formulation is equivalent to that in the original HRd model.

$$\alpha_{CaMK} = 0.05 \text{ ms}^{-1}; \alpha_{CaMK} = 0.00068 \text{ ms}^{-1}$$

$$CaMK_0 = 0.05; K_{m,CaM} = 0.0015 \text{ mmol/L}; K_{m,CaMK} = 0.15$$

$$CaMK_{bound} = CaMK_o \cdot (1 - CaMK_{trap}) \cdot \frac{1}{1 + \frac{K_{m,CaM}}{[Ca^{2+}]_{SS}}}$$

$$\frac{dCaMK_{trap}}{dt} = \alpha_{CaMK} \cdot CaMK_{bound} \cdot \left(CaMK_{bound} + CaMK_{trap} \right) - \beta_{CaMK} \cdot CaMK_{trap}$$

$$CaMK_{active} = CaMK_{bound} + CaMK_{trap}$$

Appendix B. NZ and BZ Model formulations

Note on updates to the NZ model

The control normal zone (NZ) model is based on a previously published model (Decker et al., 2009) of the canine epicardial myocyte. The late Na^+ current (I_{NaL}) in the NZ model was reformulated to reflect more detailed characterization of channel kinetics in canine (Maltsev et al., 2008b) and human ventricular (Maltsev and Undrovinas, 2006) cardiomyocytes as described in Section S3. NZ I_{Na} steady state inactivation was shifted to better reproduce the time constant of recovery of $dVdt_{max}$ recorded in NZ cells (Lue and Boyden, 1992). The NZ I_{CaL} formulation was adjusted to reproduce the effects of CaMKII overexpression (Kohlhaas et al., 2006). All other NZ current formulations are equivalent to those in the previously published model (Decker et al., 2009). The EBZ model was derived from the NZ model by incorporating available remodeling data as described below.

1. I_{Na}

Fast Na^+ current formulation is equivalent to that in a previous canine epicardial cell model (Decker et al., 2009). An additional parameter ($V_{SSI,shift}$) was introduced to facilitate fits to the relative shift in voltage dependent inactivation observed in NZ (Lue and Boyden, 1992), EBZ (Lue and Boyden, 1992) and SkM1 I_{Na}. NZ $V_{SSI,shift}$ = 2 mV and EBZ $V_{SSI,shift}$ = - 7 mV resulted in a relative shift in steady state inactivation (9 mV) matching that observed experimentally (Lue and Boyden, 1992). This shift in steady state activation also resulted in a time constant of recovery of maximum upstroke velocity in NZ and EBZ cells that matched experiments (conditioning potential of -80 mV). In addition, $\bar{G}_{Na}$ in the EBZ was reduced in order to fit the decrease in peak upstroke velocity (conditioning potential of -110 mV) observed experimentally

(Lue and Boyden, 1992). $\bar{G}_{Na}$ of SkM1 in EBZ tissue was adjusted to reproduce the 80% increase in EBZ $dVdt_{max}$ observed experimentally (Lau et al., 2009).

$V_{SSI,shift}$ Shift in steady state I_{Na} steady state inactivation, (mV)

$\bar{G}_{Na}$ Maximal conductance of I_{Na}, ms/μF

	$\bar{G}_{Na}$	$V_{SSI,shift}$
NZ	9.075 mS/μF	2 mV
EBZ	7.71375 mS/μF	-7 mV
SkM1	1.65 mS/μF	9 mV

$$E_{Na} = \frac{RT}{F} \cdot \ln\left(\frac{[Na^+]_o}{[Na^+]_i}\right)$$

$$\alpha_m = \frac{0.32 \cdot (V_m + 47.13)}{1 - \exp(-0.1 \cdot (V_m + 47.13))}$$

$$\beta_m = 0.08 \cdot \exp\left(\frac{-V_m}{11}\right)$$

If $V_m \geq -40.0$ mV

$$\alpha_h = 0.0$$

$$\beta_h = \frac{1}{0.13 \cdot \left(1 + \exp\left(\frac{(V_m - V_{SSI,shift}) + 10.66}{-11.1}\right)\right)}$$

$$\alpha_j = 0.0$$

$$\beta_j = \frac{0.3 \cdot (-2.535 \times 10^{-7}) \cdot (V_m - V_{SSI,shift})}{\exp(-0.1 \cdot ((V_m - V_{SSI,shift}) + 32)) + 1}$$

else

$$\alpha_h = 0.135 \cdot \exp\left(\frac{\left(80.0 + (V_m - V_{SSI,shift})\right)}{-6.8}\right)$$

$$\beta_h = 3.56 \cdot \exp\left(0.079 \cdot (V_m - V_{SSI,shift})\right) + 3.1 \times 10^5 \cdot \exp(0.35 \cdot (V_m - V_{SSI,shift}))$$

$$\alpha_j = \frac{(-1.2714\times10^5\cdot\exp(0.2444\cdot(V_m - V_{SSI,shift}))}{1+\exp(0.311\cdot((V_m - V_{SSI,shift})+79.23))} -$$
$$\frac{6.948\times10^{-5}\cdot\exp(-0.04391\cdot(V_m - V_{SSI,shift})))\cdot((V_m - V_{SSI,shift})+37.78)}{1+\exp(0.311\cdot((V_m - V_{SSI,shift})+79.23))}$$
$$\beta_j = \frac{0.1212\cdot\exp(-0.01052\cdot(V_m - V_{SSI,shift}))}{1+\exp(-0.1378\cdot((V_m - V_{SSI,shift})+40.14))}$$
$$I_{Na} = \bar{G}_{Na}\cdot m^3\cdot h\cdot j\cdot(V_m - E_{Na})$$

2. I_{CaL}

NZ I_{CaL} current formulation is derived from that in a previous published canine epicardial cell model (Decker et al., 2009). The NZ model was updated so that maximal CaMKII activity increases peak I_{CaL} by 30% and slows Ca^{2+} dependent inactivation (Kohlhaas et al., 2006). EBZ current parameters were altered to reproduce a) decreased density (P_{Ca}), b) rightward shift in the I-V relationship ($ACT_{\infty,shift}$) and c) faster voltage dependent inactivation ($\tau_{VDI,SS}$) (Aggarwal and Boyden, 1995).

P_{Ca} Maximum Ca^{2+} permeability of $I_{CaL,}$ cm/s

$ACT_{\infty,shift}$ Shift in I_{CaL} activation parameter, mV

$\tau_{VDI,SS}$ Minimal I_{CaL} inactivation time constant parameter, ms

$\Delta\tau_{Ca}^{CaMK}$ Maximal change in I_{CaL} inactivation time constant due to CaMKII, ms

ΔP_{Ca}^{CaMK} Maximal change in I_{CaL} Ca2+ permeability due to CaMKII, cm/s

	P_{Ca}	$ACT_{\infty,shift}$	$\tau_{VDI,SS}$
NZ	1.5555x10-4 cm/s	13.56 mV	30.553 ms
EBZ	1.187x10-4 cm/s	17.5 mV	15.0 ms

$$ACT_\infty = \frac{1}{1.0+\exp(-(V_m - ACT_{\infty,shift})/9.45)}$$

$$I_{V,\tau} = \frac{1}{\frac{1}{24.828 \cdot (1+\exp(((V_m+49.10)/10.349)))} + \frac{1}{\tau_{VDI,SS} \cdot (1+\exp((-(V_m+0.213)/10.807)))}}$$

$$ACT_\tau = 0.59+0.8 \cdot \frac{\exp(0.052 \cdot (V_m+13))}{1+\exp(0.132 \cdot (V_m+13))}$$

$$\alpha = \frac{ACT_\infty}{ACT_\tau}$$

$$\beta = \frac{1-ACT_\infty}{ACT_\tau}$$

$$I_{V,\infty} = \frac{1/(1 + \exp((V_m+17.5)/3))+0.25}{1.25}$$

$$x = \frac{I_{V,\infty}}{I_{V,\tau}}$$

$$y = \frac{1-I_{V,\infty}}{I_{V,\tau}}$$

$$\Delta\tau_{Ca}^{CaMK} = \frac{7.5}{1+\left(\frac{0.7}{CaMK_{active}}\right)^4}$$

$$I_{Ca}^{*} = 25 - \frac{17.5 - \Delta\tau_{Ca}^{CaMK})}{1+\left(\frac{0.003}{[Ca^{2+}]_{SS,CaL}}\right)^4}$$

$$I^{*}_{V,\tau} = \frac{1}{\frac{1}{24.828 \cdot (1+\exp(((V_m+49.10)/10.349)))} + \frac{1}{I^{*}_{Ca} \cdot (1+\exp((-(V_m+0.213)/10.807)))}}$$

$$I^{*}_{V,\infty} = \frac{1/(1 + \exp((V_m+17.5)/3))+0.0001}{1.0001}$$

$$x^{*} = \frac{I^{*}_{V,\infty}}{I^{*}_{V,\tau}}$$

$$y^{*} = \frac{1-I^{*}_{V,\infty}}{I^{*}_{V,\tau}}$$

$$\delta = \frac{3}{1+\left(\frac{0.003}{[Ca^{2+}]_{SS,CaL}}\right)^4}$$

$$\theta = 1$$

$$\theta_I = 0.000001$$

$$\delta_I = \theta_I \cdot \left(\frac{x \cdot y^* \cdot \delta}{y \cdot x^* \cdot \theta}\right)$$

State transitions:

$$\frac{dC}{dt} = -(\alpha + \delta + y) \cdot C + \beta \cdot O + \theta \cdot C^* + x \cdot CI$$

$$\frac{dO}{dt} = -(\beta + \delta + y) \cdot O + \alpha \cdot C + \theta \cdot O^* + x \cdot OI$$

$$\frac{dC^*}{dt} = -(\alpha + \theta + y^*) \cdot C^* + \delta \cdot C + \beta \cdot O^* + x^* \cdot CI^*$$

$$\frac{dO^*}{dt} = -(\beta + \theta + y^*) \cdot O^* + \delta \cdot O + \alpha \cdot C^* + x^* \cdot OI^*$$

$$\frac{dCI}{dt} = -(\alpha + \delta_I + x) \cdot CI + y \cdot C + \theta_I \cdot CI^* + \beta \cdot OI$$

$$\frac{dOI}{dt} = -(\beta + \delta_I + x) \cdot OI + y \cdot O + \theta_I \cdot OI^* + \alpha \cdot CI$$

$$\frac{dCI^*}{dt} = -(\alpha + \theta_I + x^*) \cdot CI^* + \delta_I \cdot CI + y^* \cdot C^* + \beta \cdot OI^*$$

$$\frac{dOI^*}{dt} = -(\beta + \theta_I + x^*) \cdot OI^* + \delta_I \cdot OI + y^* \cdot O^* + \alpha \cdot CI^*$$

$$\Delta P_{Ca}^{CaMK} = \frac{0.4}{1 + \left(\frac{0.7}{CaMK_{active}}\right)^4}$$

$\gamma_{Cai} = 1; \gamma_{Cao} = 0.341$

$$\bar{I}_{CaL} = (1 + \Delta P_{Ca}^{CaMK}) \cdot P_{Ca} \cdot z_{Ca}^2 \cdot \frac{V_m \cdot F^2}{RT} \left(\frac{\gamma_{Cai} \cdot [Ca^{2+}]_{SS,CaL} \cdot \exp\left(z_{Ca} \cdot \frac{V_m \cdot F}{RT}\right) - \gamma_{Cao} \cdot [Ca^{2+}]_o}{\exp\left(z_{Ca} \cdot \frac{V_m \cdot F}{RT}\right) - 1} \right)$$

$$I_{CaL} = \bar{I}_{CaL} \cdot (O + O^*)$$

3. I_{K1}

The approximately 70% reduction in density of I_{K1} recorded in the EBZ during ramp (Pinto and Boyden, 1999) and clamp (Lue and Boyden, 1992) protocols was reproduced by reducing the parameter $\overline{G}_{K1,5.4}$

$\bar{G}_{K1,5.4}$ Maximal I_{K1} conductance at $[K^+]_o$ = 5.4 mM, ms/μF

	$\overline{G}_{K1,5.4}$
NZ	0.5 ms/μF
EBZ	0.15 ms/μF

$$E_{K1} = \frac{RT}{F} \cdot \ln\left(\frac{[K^+]_o}{[K^+]_i}\right)$$

$$\alpha_{K1} = \frac{1.02}{1 + \exp(0.2385 \cdot (V_m - E_{K1} - 59.215))}$$

$$\beta_{K1} = \frac{0.49124 \cdot \exp(0.08032 \cdot (V_m - E_{K1} + 5.476)) + \exp(0.06175 \cdot (V_m - E_{K1} - 594.31))}{1 + \exp(-0.5143 \cdot (V_m - E_{K1} + 4.753))}$$

$$K_1 = \frac{\alpha_{K1}}{\alpha_{K1} + \beta_{K1}}$$

$$\overline{G}_{K1} = \overline{G}_{K1,5.4} \cdot \sqrt{\frac{[K^+]_o}{5.4}}$$

$$I_{K1} = \overline{G}_{K1} \cdot K_1 \cdot (V_m - E_{K1})$$

4. I_{Kr}

I_{Kr} in the EBZ model was altered to fit experimentally observed reduction in density and more rapid activation (Jiang et al., 2000).

$\bar{G}_{Kr,5.4}$ Maximal I_{Kr} conductance at $[K^+]_o$ = 5.4 mM, ms/μF
$Xr_{\tau,MAG}$ I_{Kr} activation time constant parameter, $ms^{-1}mV^{-1}$

	$\overline{G}_{Kr,5.4}$	$Xr_{\tau,MAG}$
NZ	0.0138542 ms/μF	0.0006 $ms^{-1}mV^{-1}$
EBZ	0.009698 ms/μF	0.001 $ms^{-1}mV^{-1}$

$$\overline{G}_{Kr} = 0.0138542 \cdot \sqrt{\frac{[K^+]_o}{5.4}}$$

$$E_{Kr} = \frac{RT}{F} \cdot \ln\left(\frac{[K^+]_o}{[K^+]_i}\right)$$

$$\tau_{Xr} = \frac{1}{\frac{Xr_{\tau,MAG} \cdot (V_m - 1.7384)}{1 - \exp(-0.136 \cdot (V_m - 1.7384))} + \frac{3 \times 10^{-4} \cdot (V_m + 38.3608)}{\exp(0.1522 \cdot (V_m + 38.3608)) - 1}}$$

$$X_{r\infty} = \frac{1}{1 + \exp(-(V_m + 10.0805)/4.25)}$$

$$R_{Kr} = \frac{1}{1 + \exp((V_m + 10)/15.4)}$$

$$I_{Kr} = \overline{G}_{Kr} \cdot X_r \cdot R_{Kr} \cdot (V_m - E_{Kr})$$

5. I_{Ks}

I_{Ks} density in the EBZ was reduced to match experiments (Jiang et al., 2000).

$\bar{G}_{Ks,\infty}$ Minimum I_{Ks} conductance, ms/μF

	$\overline{G}_{Ks,\infty}$
NZ	0.0826 ms/μF
EBZ	0.01652 ms/μF

$$\alpha = 1.4864 \cdot 10^{-2} \cdot \exp\left(2.9877 \cdot 10^{-2} \cdot V_m \cdot (F/(R \cdot T))\right)$$
$$\beta = 8.3986 \cdot 10^{-2} \cdot \exp\left(-5.5461 \cdot 10^{-2} \cdot V_m \cdot (F/(R \cdot T))\right)$$
$$\gamma = 1.4601 \cdot 10^{-2} \cdot \exp\left(2.4465 \cdot 10^{-1} \cdot V_m \cdot (F/(R \cdot T))\right)$$
$$\delta = 3.1173 \cdot 10^{-3} \cdot \exp\left(-4.2625 \cdot 10^{-1} \cdot V_m \cdot (F/(R \cdot T))\right)$$
$$\eta = 7.7320 \cdot 10^{-2} \cdot \exp\left(-6.4726 \cdot 10^{-2} \cdot V_m \cdot (F/(R \cdot T))\right)$$
$$\theta = 8.9538 \cdot 10^{-2}$$
$$\omega = 7.9405 \cdot 10^{-1} \cdot \exp\left(-8.0174 \cdot 10^{-2} \cdot V_m \cdot (F/(R \cdot T))\right)$$
$$\psi = 5.8638 \cdot 10^{-1} \cdot \exp\left(2.8206 \cdot 10^{-1} \cdot V_m \cdot (F/(R \cdot T))\right)$$

State transitions:

$$\frac{dC_1}{dt} = -(4\alpha) \cdot C_1 + \beta \cdot C_2$$
$$\frac{dC_2}{dt} = -(3\alpha + \beta + \gamma) \cdot C_2 + 4\alpha \cdot C_1 + 2\beta \cdot C_3 + \delta \cdot C_6$$
$$\frac{dC_3}{dt} = -(2\alpha + 2\beta + 2\gamma) \cdot C_3 + 3\alpha \cdot C_2 + 3\beta \cdot C_4 + \delta \cdot C_7$$
$$\frac{dC_4}{dt} = -(\alpha + 3\beta + 3\gamma) \cdot C_4 + 2\alpha \cdot C_3 + 4\beta \cdot C_5 + \delta \cdot C_8$$
$$\frac{dC_5}{dt} = -(4\beta + 4\gamma) \cdot C_5 + \alpha \cdot C_4 + \delta \cdot C_9$$
$$\frac{dC_6}{dt} = -(3\alpha + \delta) \cdot C_6 + \beta \cdot C_7 + \gamma \cdot C_2$$
$$\frac{dC_7}{dt} = -(2\alpha + \beta + \gamma + \delta) \cdot C_7 + 3\alpha \cdot C_6 + 2\beta \cdot C_8 + 2\gamma \cdot C_3 + 2\delta \cdot C_{10}$$
$$\frac{dC_8}{dt} = -(\alpha + 2\beta + 2\gamma + \delta) \cdot C_8 + 2\alpha \cdot C_7 + 3\beta \cdot C_9 + 3\gamma \cdot C_4 + 2\delta \cdot C_{11}$$
$$\frac{dC_9}{dt} = -(3\beta + 3\gamma + \delta) \cdot C_9 + \alpha \cdot C_8 + 4\gamma \cdot C_5 + 2\delta \cdot C_{12}$$
$$\frac{dC_{10}}{dt} = -(2\alpha + 2\delta) \cdot C_{10} + \beta \cdot C_{11} + \gamma \cdot C_7$$
$$\frac{dC_{11}}{dt} = -(\alpha + \beta + \gamma + 2\delta) \cdot C_{11} + 2\alpha \cdot C_{10} + 2\beta \cdot C_{12} + 2\gamma \cdot C_8 + 3\delta \cdot C_{13}$$

$$\frac{dC_{12}}{dt} = -(2\beta + 2\gamma + 2\delta)\cdot C_{12} + \alpha \cdot C_{11} + 3\gamma \cdot C_9 + 3\delta \cdot C_{14}$$

$$\frac{dC_{13}}{dt} = -(\alpha + 3\delta)\cdot C_{13} + \beta \cdot C_{14} + \gamma \cdot C_{11}$$

$$\frac{dC_{14}}{dt} = -(\beta + \gamma + 3\delta)\cdot C_{14} + \alpha \cdot C_{13} + 2\gamma \cdot C_{12} + 4\delta \cdot C_{15}$$

$$\frac{dC_{15}}{dt} = -(4\delta + \theta)\cdot C_{15} + \gamma \cdot C_{14} + \eta \cdot O_1$$

$$\frac{dO_1}{dt} = -(\eta + \psi)\cdot O_1 + \theta \cdot C_{15} + \omega \cdot O_2$$

$$\frac{dO_2}{dt} = -(\omega)\cdot O_2 + \psi \cdot O_1$$

Current:

$$\overline{G}_{Ks} = \overline{G}_{Ks,\infty} \cdot \left(1 + \frac{0.6}{1 + \left(\frac{3.8 \cdot 10^{-5}}{[Ca^{2+}]_i} \right)^{1.4}} \right)$$

$$O_{Ks} = O_1 + O_2$$

$$E_{Ks} = \frac{R \cdot T}{F} \cdot \log \frac{[K^+]_o + P_{Na/K} \cdot [Na^+]_o}{[K^+]_i + P_{Na/K} \cdot [Na^+]_i}$$

$$I_{Ks} = \bar{G}_{Ks} \cdot O_{Ks} \cdot (V_m - E_{Ks})$$

6. I_{to1}

I_{to1} density in the EBZ was reduced by 90% (Lue and Boyden, 1992).

$\bar{G}_{to1}$ Maximal I_{to1} conductance, ms/μF

	$\overline{G}_{to1}$
NZ	0.4975 ms/μF
EBZ	0.04975 ms/μF

G. I_{to2}

I_{to2} density in the EBZ was reduced to match experiments (Aggarwal et al., 1997).

$P_{Cl}(I_{to2})$ Maximum Cl^- permeability of $I_{to2,}$ cm/s

	$P_{Cl}(I_{to2})$
NZ	9e-7 cm/s
EBZ	7.767e-7 cm/s

7. I_{NaL}

I_{NaL} in the NZ and EBZ models was reformulated to better fit recent data from human and canine ventricular myocytes and reflect present understanding of the current (Zaza et al., 2008). At 24°C, human (Maltsev and Undrovinas, 2006) and canine (Maltsev et al., 2008a) ventricular I_{NaL} inactivates with fast ($\tau \sim 50$ ms) and slow ($\tau \sim 500$ ms) time constants during a pulse to -30 mV. These fast and slow time constants are thought to represent burst and late activating modes of the cardiac Na^+ channel isoform ($Na_v1.5$), respectively. Total I_{NaL} in the model is calculated as the sum of channels in the late bursting (*LB*) and late scattered (*LS*) modes. Time and voltage dependent inactivation of the burst and late activating modes was implemented using Hodgin-Huxley type gates h_{LB} and h_{LS}. Considering the similarities in reported behavior in human (Maltsev and Undrovinas, 2006) and canine ventricle (Maltsev et al., 2008a), I_{NaL} onset of inactivation is based on characterization of the time course of inactivation in human ventricular myocytes (Maltsev and Undrovinas, 2006), as adjusted to 37°C based on Q10 data (Maltsev and Undrovinas, 2006). The relative contribution of the late scattered mode ($f_{LS} = 0.27$) and steady state voltage dependence of inactivation is based on canine ventricular myocyte data (Maltsev et al., 2008a). The time constant of recovery from inactivation was adapted from data in human ventricular myocytes (Maltsev et al., 1998), also adjusted to 37°C based on Q10 of 2.2 (Maltsev and Undrovinas, 2006). Current density was adjusted to reproduce the experimentally measured

APD prolongation of approximately 40 ms after application of low concentrations of TTX in canine epicardial myocytes (Zygmunt et al., 2001). No experimental data are available on I_{NaL} in the EBZ.

LS	Late scattered mode, I_{NaL}
LB	Late bursting mode, I_{NaL}
m_L	activation gate, I_{NaL}
h_{LB}	late bursting inactivation gate, I_{NaL}
h_{LS}	late scattered inactivation gate, I_{NaL}
$\alpha_{m,L}, \beta_{m,L}$	Opening and closing rate constants of I_{NaL} activation gate
$\tau_{h,LB}$	Time constant of late bursting I_{NaL} inactivation gate
$\tau_{h,LS}$	Time constant of late scattered I_{NaL} inactivation gate
$h_{LB,\infty}$	Steady state value of late bursting I_{NaL} inactivation gate
$h_{LS,\infty}$	Steady state value of late scattered I_{NaL} inactivation gate
h_{LB}	late bursting I_{NaL} inactivation gate
f_{LS}	Relative contribution of I_{NaL} late scattered mode

$$\alpha_{m,L} = \frac{0.32 \cdot (V_m + 47.13)}{1 - \exp(-0.1 \cdot (V_m + 47.13))}$$

$$\beta_{m,L} = 0.08 \cdot \exp\left(\frac{-V_m}{11.0}\right)$$

$$\tau_{h,LS} = \frac{1}{\frac{1}{215.4339 \cdot \left(1 + exp\left(\frac{V_m + 85.9963}{8.9337}\right)\right)} + \frac{1}{168.6230 \cdot \left(1 + exp\left(\frac{-(V_m + 83.1026)}{10.8195}\right)\right)}}$$

$$\tau_{h,LB} = \frac{1}{\frac{1}{215.4339 \cdot \left(1 + exp\left(\frac{V_m + 85.9963}{8.9337}\right)\right)} + \frac{1}{11.1135 \cdot \left(1 + exp\left(\frac{-(V_m + 33.3651)}{14.9459}\right)\right)}}$$

$$h_{LB,\infty} = h_{LS,\infty} = \frac{1}{1 + \exp((V_m + 91)/6.1)}$$

$$f_{LS} = 0.27$$

$$\overline{G}_{Na,L} = 0.0065 \text{ ms}/\mu\text{F}$$

$$E_{Na,L} = \frac{RT}{F} \cdot \ln\left(\frac{[Na^+]_o}{[Na^+]_i}\right)$$

$$I_{Na,L} = \bar{G}_{Na,L} \cdot m_L^3 \cdot \left(V_m - E_{Na,L}\right) \cdot ((1 - f_{LS}) \cdot h_{LB} + f_{LS} \cdot h_{LS})$$

References

Aggarwal, R., and Boyden, P.A. (1995). Diminished Ca2+ and Ba2+ currents in myocytes surviving in the epicardial border zone of the 5-day infarcted canine heart. Circ Res *77*, 1180-1191.

Aggarwal, R., Pu, J., and Boyden, P.A. (1997). Ca(2+)-dependent outward currents in myocytes from epicardial border zone of 5-day infarcted canine heart. Am J Physiol *273*, H1386-1394.

Baba, S., Dun, W., Cabo, C., and Boyden, P.A. (2005). Remodeling in cells from different regions of the reentrant circuit during ventricular tachycardia. Circulation *112*, 2386-2396.

Baher, A., Qu, Z., Hayatdavoudi, A., Lamp, S.T., Yang, M.J., Xie, F., Turner, S., Garfinkel, A., and Weiss, J.N. (2006). Short-term Cardiac Memory and Mother Rotor Fibrillation. Am J Physiol Heart Circ Physiol.

Baher, A., Qu, Z., Hayatdavoudi, A., Lamp, S.T., Yang, M.J., Xie, F., Turner, S., Garfinkel, A., and Weiss, J.N. (2007). Short-term cardiac memory and mother rotor fibrillation. Am J Physiol Heart Circ Physiol *292*, H180-189.

Beaumont, J., Davidenko, N., Davidenko, J.M., and Jalife, J. (1998). Spiral waves in two-dimensional models of ventricular muscle: formation of a stationary core. Biophys J *75*, 1-14.

Birinyi, P., Acsai, K., Banyasz, T., Toth, A., Horvath, B., Virag, L., Szentandrassy, N., Magyar, J., Varro, A., Fulop, F., *et al.* (2005). Effects of SEA0400 and KB-R7943 on Na+/Ca2+ exchange current and L-type Ca2+ current in canine ventricular cardiomyocytes. Naunyn Schmiedebergs Arch Pharmacol *372*, 63-70.

Boyett, M.R., and Jewell, B.R. (1978). A study of the factors responsible for rate-dependent shortening of the action potential in mammalian ventricular muscle. J Physiol *285*, 359-380.

Cabo, C., and Boyden, P.A. (2003). Electrical remodeling of the epicardial border zone in the canine infarcted heart: a computational analysis. Am J Physiol Heart Circ Physiol *284*, H372-384.

Cabo, C., and Boyden, P.A. (2006). Heterogeneous Gap Junction Remodeling Stabilizes Reentrant Circuits in the Epicardial Border Zone of the Healing Canine Infarct: A Computational Study. Am J Physiol Heart Circ Physiol.

Cabo, C., Pertsov, A.M., Baxter, W.T., Davidenko, J.M., Gray, R.A., and Jalife, J. (1994). Wave-front curvature as a cause of slow conduction and block in isolated cardiac muscle. Circ Res *75*, 1014-1028.

Cabo, C., Yao, J., Boyden, P.A., Chen, S., Hussain, W., Duffy, H.S., Ciaccio, E.J., Peters, N.S., and Wit, A.L. (2006). Heterogeneous gap junction remodeling in reentrant circuits in the epicardial border zone of the healing canine infarct. Cardiovasc Res.

Calloe, K., Soltysinska, E., Jespersen, T., Lundby, A., Antzelevitch, C., Olesen, S.P., and Cordeiro, J.M. (2010). Differential effects of the transient outward K(+) current activator NS5806 in the canine left ventricle. J Mol Cell Cardiol *48*, 191-200.

Cardinal, R., Vermeulen, M., Shenasa, M., Roberge, F., Page, P., Helie, F., and Savard, P. (1988). Anisotropic conduction and functional dissociation of ischemic tissue during reentrant ventricular tachycardia in canine myocardial infarction. Circulation *77*, 1162-1176.

Cherry, E.M., and Fenton, F.H. (2004). Suppression of alternans and conduction blocks despite steep APD restitution: electrotonic, memory, and conduction velocity restitution effects. Am J Physiol Heart Circ Physiol *286*, H2332-2341.

Cherry, E.M., and Fenton, F.H. (2006). A tale of two dogs: Analyzing two models of canine ventricular electrophysiology. Am J Physiol Heart Circ Physiol.

Cherry, E.M., and Fenton, F.H. (2007). A tale of two dogs: analyzing two models of canine ventricular electrophysiology. Am J Physiol Heart Circ Physiol *292*, H43-55.

Christensen, M.D., Dun, W., Boyden, P.A., Anderson, M.E., Mohler, P.J., and Hund, T.J. (2009). Oxidized calmodulin kinase II regulates conduction following myocardial infarction: a computational analysis. PLoS Comput Biol *5*, e1000583.

Ciaccio, E.J. (2000). Localization of the slow conduction zone during reentrant ventricular tachycardia. Circulation *102*, 464-469.

Ciaccio, E.J. (2001). Dynamic relationship of cycle length to reentrant circuit geometry and to the slow conduction zone during ventricular tachycardia. Circulation *103*, 1017-1024.

Ciaccio, E.J. (2002). Premature excitation and onset of reentrant ventricular tachycardia. Am J Physiol Heart Circ Physiol *283*, H1703-1712.

Ciaccio, E.J., Costeas, C., Coromilas, J., and Wit, A.L. (2001a). Static relationship of cycle length to reentrant circuit geometry. Circulation *104*, 1946-1951.

Ciaccio, E.J., Tosti, A.C., and Scheinman, M.M. (2001b). Relationship between sinus rhythm activation and the reentrant ventricular tachycardia isthmus. Circulation *104*, 613-619.

Cordeiro, J.M., Greene, L., Heilmann, C., Antzelevitch, D., and Antzelevitch, C. (2004). Transmural heterogeneity of calcium activity and mechanical function in the canine left ventricle. Am J Physiol Heart Circ Physiol *286*, H1471-1479.

Cordeiro, J.M., Marieb, M., Pfeiffer, R., Calloe, K., Burashnikov, E., and Antzelevitch, C. (2009). Accelerated inactivation of the L-type calcium current due to a mutation in CACNB2b underlies Brugada syndrome. J Mol Cell Cardiol *46*, 695-703.

Decker, K.F., Heijman, J., Silva, J.R., Hund, T.J., and Rudy, Y. (2009). Properties and ionic mechanisms of action potential adaptation, restitution, and accommodation in canine epicardium. Am J Physiol Heart Circ Physiol *296*, H1017-1026.

Despa, S., Islam, M.A., Pogwizd, S.M., and Bers, D.M. (2002). Intracellular [Na+] and Na+ pump rate in rat and rabbit ventricular myocytes. J Physiol *539*, 133-143.

Di Diego, J.M., Sun, Z.Q., and Antzelevitch, C. (1996). I(to) and action potential notch are smaller in left vs. right canine ventricular epicardium. Am J Physiol *271*, H548-561.

Dillon, S.M., Allessie, M.A., Ursell, P.C., and Wit, A.L. (1988). Influences of anisotropic tissue structure on reentrant circuits in the epicardial border zone of subacute canine infarcts. Circ Res *63*, 182-206.

Dong, M., Sun, X., Prinz, A.A., and Wang, H.S. (2006). Effect of simulated I(to) on guinea pig and canine ventricular action potential morphology. Am J Physiol Heart Circ Physiol *291*, H631-637.

Dumaine, R., Towbin, J.A., Brugada, P., Vatta, M., Nesterenko, D.V., Nesterenko, V.V., Brugada, J., Brugada, R., and Antzelevitch, C. (1999). Ionic mechanisms responsible for the electrocardiographic phenotype of the Brugada syndrome are temperature dependent. Circ Res *85*, 803-809.

Dun, W., Baba, S., Yagi, T., and Boyden, P.A. (2004). Dynamic remodeling of K+ and Ca2+ currents in cells that survived in the epicardial border zone of canine healed infarcted heart. Am J Physiol Heart Circ Physiol *287*, H1046-1054.

Dun, W., and Boyden, P.A. (2005). Diverse phenotypes of outward currents in cells that have survived in the 5-day-infarcted heart. Am J Physiol Heart Circ Physiol *289*, H667-673.

El-Sherif, N., Hope, R.R., Scherlag, B.J., and Lazzara, R. (1977a). Re-entrant ventricular arrhythmias in the late myocardial infarction period. 2. Patterns of initiation and termination of re-entry. Circulation *55*, 702-719.

El-Sherif, N., Lazzara, R., Hope, R.R., and Scherlag, B.J. (1977b). Re-entrant ventricular arrhythmias in the late myocardial infarction period. 3. Manifest and concealed extrasystolic grouping. Circulation *56*, 225-234.

El-Sherif, N., Scherlag, B.J., Lazzara, R., and Hope, R.R. (1977c). Re-entrant ventricular arrhythmias in the late myocardial infarction period. 1. Conduction characteristics in the infarction zone. Circulation *55*, 686-702.

El-Sherif, N., Smith, R.A., and Evans, K. (1981). Canine ventricular arrhythmias in the late myocardial infarction period. 8. Epicardial mapping of reentrant circuits. Circ Res *49*, 255-265.

Elzinga, G., Lab, M.J., Noble, M.I., Papadoyannis, D.E., Pidgeon, J., Seed, A., and Wohlfart, B. (1981). The action-potential duration and contractile response of the intact heart related to the preceding interval and the preceding beat in the dog and cat. J Physiol *314*, 481-500.

Faber, G.M., and Rudy, Y. (2000). Action potential and contractility changes in [Na(+)](i) overloaded cardiac myocytes: a simulation study. Biophys J *78*, 2392-2404.

Faber, G.M., Silva, J., Livshitz, L., and Rudy, Y. (2007). Kinetic properties of the cardiac L-type Ca2+ channel and its role in myocyte electrophysiology: a theoretical investigation. Biophys J *92*, 1522-1543.

Fast, V.G., and Kleber, A.G. (1995). Block of impulse propagation at an abrupt tissue expansion: evaluation of the critical strand diameter in 2- and 3-dimensional computer models. Cardiovasc Res *30*, 449-459.

Fast, V.G., and Kleber, A.G. (1997). Role of wavefront curvature in propagation of cardiac impulse. Cardiovasc Res *33*, 258-271.

Fenton, F.H., Cherry, E.M., Hastings, H.M., and Evans, S.J. (2002). Multiple mechanisms of spiral wave breakup in a model of cardiac electrical activity. Chaos *12*, 852-892.

Findlay, I. (2002a). Voltage- and cation-dependent inactivation of L-type Ca2+ channel currents in guinea-pig ventricular myocytes. J Physiol *541*, 731-740.

Findlay, I. (2002b). Voltage-dependent inactivation of L-type Ca2+ currents in guinea-pig ventricular myocytes. J Physiol *545*, 389-397.

Flaim, S.N., Giles, W.R., and McCulloch, A.D. (2006). Contributions of sustained INa and IKv43 to transmural heterogeneity of early repolarization and arrhythmogenesis in canine left ventricular myocytes. Am J Physiol Heart Circ Physiol *291*, H2617-2629.

Fox, J.J., McHarg, J.L., and Gilmour, R.F., Jr. (2002). Ionic mechanism of electrical alternans. Am J Physiol Heart Circ Physiol *282*, H516-530.

Franz, M.R., Swerdlow, C.D., Liem, L.B., and Schaefer, J. (1988). Cycle length dependence of human action potential duration in vivo. Effects of single extrastimuli, sudden sustained rate acceleration and deceleration, and different steady-state frequencies. J Clin Invest *82*, 972-979.

Gao, J., Mathias, R.T., Cohen, I.S., and Baldo, G.J. (1995). Two functionally different Na/K pumps in cardiac ventricular myocytes. J Gen Physiol *106*, 995-1030.

Gao, J., Wang, W., Cohen, I.S., and Mathias, R.T. (2005). Transmural gradients in Na/K pump activity and [Na+]I in canine ventricle. Biophys J *89*, 1700-1709.

Gough, W.B., Mehra, R., Restivo, M., Zeiler, R.H., and el-Sherif, N. (1985). Reentrant ventricular arrhythmias in the late myocardial infarction period in the dog. 13. Correlation of activation and refractory maps. Circ Res *57*, 432-442.

Greenstein, J.L., Wu, R., Po, S., Tomaselli, G.F., and Winslow, R.L. (2000). Role of the calcium-independent transient outward current I(to1) in shaping action potential morphology and duration. Circ Res *87*, 1026-1033.

Han, J., and Moe, G.K. (1969). Cumulative effects of cycle length on refractory periods of cardiac tissues. Am J Physiol *217*, 106-109.

Huelsing, D.J., Pollard, A.E., and Spitzer, K.W. (2001). Transient outward current modulates discontinuous conduction in rabbit ventricular cell pairs. Cardiovasc Res *49*, 779-789.

Hund, T.J., Decker, K.F., Kanter, E., Mohler, P.J., Boyden, P.A., Schuessler, R.B., Yamada, K.A., and Rudy, Y. (2008a). Role of activated CaMKII in abnormal calcium homeostasis and I(Na) remodeling after myocardial infarction: insights from mathematical modeling. J Mol Cell Cardiol *45*, 420-428.

Hund, T.J., Decker, K.F., Kanter, E., Mohler, P.J., Boyden, P.A., Schuessler, R.B., Yamada, K.A., and Rudy, Y. (2008b). Role of activated CaMKII in abnormal calcium homeostasis and I(Na) remodeling after myocardial infarction: Insights from mathematical modeling. J Mol Cell Cardiol.

Hund, T.J., Kucera, J.P., Otani, N.F., and Rudy, Y. (2001). Ionic charge conservation and long-term steady state in the Luo-Rudy dynamic cell model. Biophys J *81*, 3324-3331.

Hund, T.J., and Rudy, Y. (2000). Determinants of excitability in cardiac myocytes: mechanistic investigation of memory effect. Biophys J *79*, 3095-3104.

Hund, T.J., and Rudy, Y. (2004). Rate dependence and regulation of action potential and calcium transient in a canine cardiac ventricular cell model. Circulation *110*, 3168-3174.

Hund, T.J., and Rudy, Y. (2006). A role for calcium/calmodulin-dependent protein kinase II in cardiac disease and arrhythmia. Handb Exp Pharmacol, 201-220.

Janse, M.J., and Wit, A.L. (1989). Electrophysiological mechanisms of ventricular arrhythmias resulting from myocardial ischemia and infarction. Physiol Rev *69*, 1049-1169.

Jiang, M., Cabo, C., Yao, J., Boyden, P.A., and Tseng, G. (2000). Delayed rectifier K currents have reduced amplitudes and altered kinetics in myocytes from infarcted canine ventricle. Cardiovasc Res *48*, 34-43.

Joyner, R.W., Kumar, R., Wilders, R., Jongsma, H.J., Verheijck, E.E., Golod, D.A., Van Ginneken, A.C., Wagner, M.B., and Goolsby, W.N. (1996). Modulating L-type calcium current affects discontinuous cardiac action potential conduction. Biophys J *71*, 237-245.

Kaab, S., Nuss, H.B., Chiamvimonvat, N., O'Rourke, B., Pak, P.H., Kass, D.A., Marban, E., and Tomaselli, G.F. (1996). Ionic mechanism of action potential prolongation in ventricular myocytes from dogs with pacing-induced heart failure. Circ Res *78*, 262-273.

Kalb, S.S., Dobrovolny, H.M., Tolkacheva, E.G., Idriss, S.F., Krassowska, W., and Gauthier, D.J. (2004). The restitution portrait: a new method for investigating rate-dependent restitution. J Cardiovasc Electrophysiol *15*, 698-709.

Karma, A. (1994). Electrical alternans and spiral wave breakup in cardiac tissue. Chaos *4*, 461-472.

Kohlhaas, M., Zhang, T., Seidler, T., Zibrova, D., Dybkova, N., Steen, A., Wagner, S., Chen, L., Brown, J.H., Bers, D.M., *et al.* (2006). Increased sarcoplasmic reticulum calcium leak but unaltered contractility by acute CaMKII overexpression in isolated rabbit cardiac myocytes. Circ Res *98*, 235-244.

Krishnan, S.C., and Antzelevitch, C. (1991). Sodium channel block produces opposite electrophysiological effects in canine ventricular epicardium and endocardium. Circ Res *69*, 277-291.

Lau, D.H., Clausen, C., Sosunov, E.A., Shlapakova, I.N., Anyukhovsky, E.P., Danilo, P., Jr., Rosen, T.S., Kelly, C., Duffy, H.S., Szabolcs, M.J., *et al.* (2009). Epicardial border zone overexpression of skeletal muscle sodium channel SkM1 normalizes activation, preserves conduction, and suppresses ventricular arrhythmia: an in silico, in vivo, in vitro study. Circulation *119*, 19-27.

Licata, A., Aggarwal, R., Robinson, R.B., and Boyden, P. (1997). Frequency dependent effects on Cai transients and cell shortening in myocytes that survive in the infarcted heart. Cardiovasc Res *33*, 341-350.

Litovsky, S.H., and Antzelevitch, C. (1989). Rate dependence of action potential duration and refractoriness in canine ventricular endocardium differs from that of epicardium: role of the transient outward current. J Am Coll Cardiol *14*, 1053-1066.

Liu, D.W., and Antzelevitch, C. (1995). Characteristics of the delayed rectifier current (IKr and IKs) in canine ventricular epicardial, midmyocardial, and endocardial myocytes. A weaker IKs contributes to the longer action potential of the M cell. Circ Res *76*, 351-365.

Liu, D.W., Gintant, G.A., and Antzelevitch, C. (1993). Ionic bases for electrophysiological distinctions among epicardial, midmyocardial, and endocardial myocytes from the free wall of the canine left ventricle. Circ Res *72*, 671-687.

Livshitz, L.M., and Rudy, Y. (2007). Regulation of Ca2+ and electrical alternans in cardiac myocytes: role of CAMKII and repolarizing currents. Am J Physiol Heart Circ Physiol *292*, H2854-2866.

Lue, W.M., and Boyden, P.A. (1992). Abnormal electrical properties of myocytes from chronically infarcted canine heart. Alterations in Vmax and the transient outward current. Circulation *85*, 1175-1188.

Lux, R.L., and Ershler, P.R. (2003). Cycle length sequence dependent repolarization dynamics. J Electrocardiol *36 Suppl,* 205-208.

Magyar, J., Szentandrassy, N., Banyasz, T., Fulop, L., Varro, A., and Nanasi, P.P. (2002). Effects of thymol on calcium and potassium currents in canine and human ventricular cardiomyocytes. Br J Pharmacol *136*, 330-338.

Mahajan, A., Shiferaw, Y., Sato, D., Baher, A., Olcese, R., Xie, L.H., Yang, M.J., Chen, P.S., Restrepo, J.G., Karma, A., *et al.* (2008). A rabbit ventricular action potential model replicating cardiac dynamics at rapid heart rates. Biophys J *94*, 392-410.

Maier, L.S. (2009). Role of CaMKII for signaling and regulation in the heart. Front Biosci *14*, 486-496.

Maltsev, V.A., Kyle, J.W., Mishra, S., and Undrovinas, A. (2008a). Molecular identity of the late sodium current in adult dog cardiomyocytes identified by Nav1.5 antisense inhibition. Am J Physiol Heart Circ Physiol *295*, H667-676.

Maltsev, V.A., Reznikov, V., Undrovinas, N.A., Sabbah, H.N., and Undrovinas, A. (2008b). Modulation of late sodium current by Ca2+, calmodulin, and CaMKII in normal and failing dog cardiomyocytes: similarities and differences. Am J Physiol Heart Circ Physiol *294*, H1597-1608.

Maltsev, V.A., Sabbah, H.N., Higgins, R.S., Silverman, N., Lesch, M., and Undrovinas, A.I. (1998). Novel, ultraslow inactivating sodium current in human ventricular cardiomyocytes. Circulation *98*, 2545-2552.

Maltsev, V.A., and Undrovinas, A.I. (2006). A multi-modal composition of the late Na+ current in human ventricular cardiomyocytes. Cardiovasc Res *69*, 116-127.

Mehra, R., Zeiler, R.H., Gough, W.B., and El-Sherif, N. (1983). Reentrant ventricular arrhythmias in the late myocardial infarction period. 9. Electrophysiologic-anatomic correlation of reentrant circuits. Circulation *67*, 11-24.

Mironov, S., Jalife, J., and Tolkacheva, E.G. (2008). Role of Conduction Velocity Restitution and Short-Term Memory in the Development of Action Potential Duration Alternans in Isolated Rabbit Hearts. Circulation.

Oudit, G.Y., Kassiri, Z., Sah, R., Ramirez, R.J., Zobel, C., and Backx, P.H. (2001). The molecular physiology of the cardiac transient outward potassium current (I(to)) in normal and diseased myocardium. J Mol Cell Cardiol *33*, 851-872.

Patel, S.P., and Campbell, D.L. (2005). Transient outward potassium current, 'Ito', phenotypes in the mammalian left ventricle: underlying molecular, cellular and biophysical mechanisms. J Physiol *569*, 7-39.

Patel, S.P., Parai, R., and Campbell, D.L. (2004). Regulation of Kv4.3 voltage-dependent gating kinetics by KChIP2 isoforms. J Physiol *557*, 19-41.

Peters, N.S., Coromilas, J., Severs, N.J., and Wit, A.L. (1997). Disturbed connexin43 gap junction distribution correlates with the location of reentrant circuits in the epicardial border zone of healing canine infarcts that cause ventricular tachycardia. Circulation *95*, 988-996.

Pinto, J.M., and Boyden, P.A. (1999). Electrical remodeling in ischemia and infarction. Cardiovasc Res *42*, 284-297.

Pitt, G.S. (2007). Calmodulin and CaMKII as molecular switches for cardiac ion channels. Cardiovasc Res *73*, 641-647.

Pu, J., and Boyden, P.A. (1997). Alterations of Na+ currents in myocytes from epicardial border zone of the infarcted heart. A possible ionic mechanism for reduced excitability and postrepolarization refractoriness. Circ Res *81*, 110-119.

Pu, J., Robinson, R.B., and Boyden, P.A. (2000). Abnormalities in Ca(i)handling in myocytes that survive in the infarcted heart are not just due to alterations in repolarization. J Mol Cell Cardiol *32*, 1509-1523.

Pu, J., Ruffy, F., and Boyden, P.A. (1999). Effects of Bay Y5959 on Ca2+ currents and intracellular Ca2+ in cells that have survived in the epicardial border of the infarcted canine heart. J Cardiovasc Pharmacol *33*, 929-937.

Qu, Z. (2004). Dynamical effects of diffusive cell coupling on cardiac excitation and propagation: a simulation study. Am J Physiol Heart Circ Physiol *287*, H2803-2812.

Qu, Z., Weiss, J.N., and Garfinkel, A. (1999). Cardiac electrical restitution properties and stability of reentrant spiral waves: a simulation study. Am J Physiol *276*, H269-283.

Restivo, M., Gough, W.B., and el-Sherif, N. (1990). Ventricular arrhythmias in the subacute myocardial infarction period. High-resolution activation and refractory patterns of reentrant rhythms. Circ Res *66*, 1310-1327.

Rohr, S., and Kucera, J.P. (1997). Involvement of the calcium inward current in cardiac impulse propagation: induction of unidirectional conduction block by nifedipine and reversal by Bay K 8644. Biophys J *72*, 754-766.

Rubart, M., Lopshire, J.C., Fineberg, N.S., and Zipes, D.P. (2000). Changes in left ventricular repolarization and ion channel currents following a transient rate increase superimposed on bradycardia in anesthetized dogs. J Cardiovasc Electrophysiol *11*, 652-664.

Rudy, Y., and Silva, J.R. (2006). Computational biology in the study of cardiac ion channels and cell electrophysiology. Q Rev Biophys *39*, 57-116.

Sah, R., Ramirez, R.J., and Backx, P.H. (2002). Modulation of Ca(2+) release in cardiac myocytes by changes in repolarization rate: role of phase-1 action potential repolarization in excitation-contraction coupling. Circ Res *90*, 165-173.

Saitoh, H., Bailey, J.C., and Surawicz, B. (1988). Alternans of action potential duration after abrupt shortening of cycle length: differences between dog Purkinje and ventricular muscle fibers. Circ Res *62*, 1027-1040.

Sakai, R., Hagiwara, N., Matsuda, N., Kassanuki, H., and Hosoda, S. (1996). Sodium--potassium pump current in rabbit sino-atrial node cells. J Physiol *490 (Pt 1)*, 51-62.

Sato, D., Shiferaw, Y., Garfinkel, A., Weiss, J.N., Qu, Z., and Karma, A. (2006). Spatially discordant alternans in cardiac tissue: role of calcium cycling. Circ Res *99*, 520-527.

Shaw, R.M., and Rudy, Y. (1995). The vulnerable window for unidirectional block in cardiac tissue: characterization and dependence on membrane excitability and intercellular coupling. J Cardiovasc Electrophysiol *6*, 115-131.

Shaw, R.M., and Rudy, Y. (1997). Ionic mechanisms of propagation in cardiac tissue. Roles of the sodium and L-type calcium currents during reduced excitability and decreased gap junction coupling. Circ Res *81*, 727-741.

Shiferaw, Y., Sato, D., and Karma, A. (2005). Coupled dynamics of voltage and calcium in paced cardiac cells. Phys Rev E Stat Nonlin Soft Matter Phys *71*, 021903.

Shimizu, W., and Antzelevitch, C. (1998). Cellular basis for the ECG features of the LQT1 form of the long-QT syndrome: effects of beta-adrenergic agonists and antagonists and sodium

channel blockers on transmural dispersion of repolarization and torsade de pointes. Circulation *98*, 2314-2322.

Shivkumar, K., Deutsch, N.A., Lamp, S.T., Khuu, K., Goldhaber, J.I., and Weiss, J.N. (1997). Mechanism of hypoxic K loss in rabbit ventricle. J Clin Invest *100*, 1782-1788.

Sicouri, S., and Antzelevitch, C. (1991). A subpopulation of cells with unique electrophysiological properties in the deep subepicardium of the canine ventricle. The M cell. Circ Res *68*, 1729-1741.

Silva, J., and Rudy, Y. (2005). Subunit interaction determines IKs participation in cardiac repolarization and repolarization reserve. Circulation *112*, 1384-1391.

Sipido, K.R., Volders, P.G., de Groot, S.H., Verdonck, F., Van de Werf, F., Wellens, H.J., and Vos, M.A. (2000). Enhanced Ca(2+) release and Na/Ca exchange activity in hypertrophied canine ventricular myocytes: potential link between contractile adaptation and arrhythmogenesis. Circulation *102*, 2137-2144.

Spach, M.S., and Dolber, P.C. (1986). Relating extracellular potentials and their derivatives to anisotropic propagation at a microscopic level in human cardiac muscle. Evidence for electrical uncoupling of side-to-side fiber connections with increasing age. Circ Res *58*, 356-371.

Spach, M.S., Heidlage, J.F., Dolber, P.C., and Barr, R.C. (2000). Electrophysiological effects of remodeling cardiac gap junctions and cell size: experimental and model studies of normal cardiac growth. Circ Res *86*, 302-311.

Spach, M.S., Miller, W.T., 3rd, Dolber, P.C., Kootsey, J.M., Sommer, J.R., and Mosher, C.E., Jr. (1982). The functional role of structural complexities in the propagation of depolarization in the atrium of the dog. Cardiac conduction disturbances due to discontinuities of effective axial resistivity. Circ Res *50*, 175-191.

Spach, M.S., Miller, W.T., 3rd, Geselowitz, D.B., Barr, R.C., Kootsey, J.M., and Johnson, E.A. (1981). The discontinuous nature of propagation in normal canine cardiac muscle. Evidence for recurrent discontinuities of intracellular resistance that affect the membrane currents. Circ Res *48*, 39-54.

Splawski, I., Tristani-Firouzi, M., Lehmann, M.H., Sanguinetti, M.C., and Keating, M.T. (1997). Mutations in the hminK gene cause long QT syndrome and suppress IKs function. Nat Genet *17*, 338-340.

Stengl, M., Volders, P.G., Thomsen, M.B., Spatjens, R.L., Sipido, K.R., and Vos, M.A. (2003). Accumulation of slowly activating delayed rectifier potassium current (IKs) in canine ventricular myocytes. J Physiol *551*, 777-786.

Sun, H., Leblanc, N., and Nattel, S. (1997). Mechanisms of inactivation of L-type calcium channels in human atrial myocytes. Am J Physiol *272*, H1625-1635.

Sun, X., and Wang, H.S. (2005). Role of the transient outward current (Ito) in shaping canine ventricular action potential--a dynamic clamp study. J Physiol *564*, 411-419.

Szabo, G., Szentandrassy, N., Biro, T., Toth, B.I., Czifra, G., Magyar, J., Banyasz, T., Varro, A., Kovacs, L., and Nanasi, P.P. (2005). Asymmetrical distribution of ion channels in canine and human left-ventricular wall: epicardium versus midmyocardium. Pflugers Arch *450*, 307-316.

Toal, S.C., Farid, T.A., Selvaraj, R., Chauhan, V.S., Masse, S., Ivanov, J., Harris, L., Downar, E., Franz, M.R., and Nanthakumar, K. (2009). Short-term memory and restitution during ventricular fibrillation in human hearts: an in vivo study. Circ Arrhythm Electrophysiol *2*, 562-570.

Tolkacheva, E.G., Anumonwo, J.M., and Jalife, J. (2006). Action potential duration restitution portraits of mammalian ventricular myocytes: role of calcium current. Biophys J *91*, 2735-2745.

Tseng, G.N. (1988). Calcium current restitution in mammalian ventricular myocytes is modulated by intracellular calcium. Circ Res *63*, 468-482.

Tseng, G.N., and Hoffman, B.F. (1989). Two components of transient outward current in canine ventricular myocytes. Circ Res *64*, 633-647.

Ursell, P.C., Gardner, P.I., Albala, A., Fenoglio, J.J., Jr., and Wit, A.L. (1985). Structural and electrophysiological changes in the epicardial border zone of canine myocardial infarcts during infarct healing. Circ Res *56*, 436-451.

Varro, A., Lathrop, D.A., and Papp, J.G. (2001). Role of the delayed rectifier component I(Ks) in cardiac repolarization. J Cardiovasc Electrophysiol *12*, 1204-1206.

Volders, P.G., Stengl, M., van Opstal, J.M., Gerlach, U., Spatjens, R.L., Beekman, J.D., Sipido, K.R., and Vos, M.A. (2003). Probing the contribution of IKs to canine ventricular repolarization: key role for beta-adrenergic receptor stimulation. Circulation *107*, 2753-2760.

Wagner, S., Dybkova, N., Rasenack, E.C., Jacobshagen, C., Fabritz, L., Kirchhof, P., Maier, S.K., Zhang, T., Hasenfuss, G., Brown, J.H., *et al.* (2006). Ca2+/calmodulin-dependent protein kinase II regulates cardiac Na+ channels. J Clin Invest *116*, 3127-3138.

Wagner, S., Hacker, E., Grandi, E., Weber, S.L., Dybkova, N., Sossalla, S., Sowa, T., Fabritz, L., Kirchhof, P., Bers, D.M., *et al.* (2009). Ca/calmodulin kinase II differentially modulates potassium currents. Circ Arrhythm Electrophysiol *2*, 285-294.

Wang, Y.G., Wagner, M.B., Kumar, R., Goolsby, W.N., and Joyner, R.W. (2000). Fast pacing facilitates discontinuous action potential propagation between rabbit atrial cells. Am J Physiol Heart Circ Physiol *279*, H2095-2103.

Watanabe, M.A., and Koller, M.L. (2002). Mathematical analysis of dynamics of cardiac memory and accommodation: theory and experiment. Am J Physiol Heart Circ Physiol *282*, H1534-1547.

Williams, B.A., Dickenson, D.R., and Beatch, G.N. (1999). Kinetics of rate-dependent shortening of action potential duration in guinea-pig ventricle; effects of IK1 and IKr blockade. Br J Pharmacol *126*, 1426-1436.

Winslow, R.L., Rice, J., Jafri, S., Marban, E., and O'Rourke, B. (1999). Mechanisms of altered excitation-contraction coupling in canine tachycardia-induced heart failure, II: model studies. Circ Res *84*, 571-586.

Wit, A.L., and Janse, M.J. (1992). Experimental models of ventricular tachycardia and fibrillation caused by ischemia and infarction. Circulation *85*, I32-42.

Yao, J.A., Hussain, W., Patel, P., Peters, N.S., Boyden, P.A., and Wit, A.L. (2003). Remodeling of gap junctional channel function in epicardial border zone of healing canine infarcts. Circ Res *92*, 437-443.

Yu, H., McKinnon, D., Dixon, J.E., Gao, J., Wymore, R., Cohen, I.S., Danilo, P., Jr., Shvilkin, A., Anyukhovsky, E.P., Sosunov, E.A., *et al.* (1999). Transient outward current, Ito1, is altered in cardiac memory. Circulation *99*, 1898-1905.

Zaza, A., Belardinelli, L., and Shryock, J.C. (2008). Pathophysiology and pharmacology of the cardiac "late sodium current.". Pharmacol Ther *119*, 326-339.

Zygmunt, A.C. (1994). Intracellular calcium activates a chloride current in canine ventricular myocytes. Am J Physiol *267*, H1984-1995.

Zygmunt, A.C., Eddlestone, G.T., Thomas, G.P., Nesterenko, V.V., and Antzelevitch, C. (2001). Larger late sodium conductance in M cells contributes to electrical heterogeneity in canine ventricle. Am J Physiol Heart Circ Physiol *281*, H689-697.

Zygmunt, A.C., Goodrow, R.J., and Antzelevitch, C. (2000). I(NaCa) contributes to electrical heterogeneity within the canine ventricle. Am J Physiol Heart Circ Physiol *278*, H1671-1678.